UNIVERSITY OF OTTAWA

Field Installation of a Fully Instrumented Prototype Solar Concentrator System: Thermal and Photovoltaic Analysis

Thesis submitted to the Faculty of Graduate and Postdoctoral Studies in partial fulfillment of the requirement for a Master's of Applied Science in Electrical and Computer Engineering.

September 2013

School of Electrical Engineering and Computer Science

University of Ottawa

Nothing exists except atoms and empty space; everything else is just opinion.

Democritus

ABSTRACT

Concentrator photovoltaics (CPV) is one of the most promising renewable technologies owing to its high efficiency, scalability, low operating expense, and small environmental impact. However, there is much research and advancements to be made before CPV is established as a cost competitive energy technology. To this end, Morgan Solar has developed the *Sun Simba*, an innovative light weight and low cost CPV module. Under the "Advancing Photonics for Economical Concentration Systems" (APECS) project, outdoor CPV test and measurement systems were designed and constructed at the University of Ottawa and at Little Rock, CA. The performance and reliability of development stage *Sun Simba* modules installed at the University of Ottawa is assessed. The Little Rock test system was constructed for purposes of future comparison and assessment. To properly assess the performance, instrumentation and data acquisition systems to measure meterological parameters and the associated electrical performance are described and the long-term performance of *Sun Simba* modules installed at the University of Ottawa is summarized.

A finite element model of a cell-on-carrier assembly was constructed to explore the parameter space of the carrier and suggest improvements in carrier design. The effect of carrier geometry, material choices, and convective boundary conditions and their influence on the cell efficiency is determined. The modelling results connected to the measured data is used to estimate the heat sinking capability of the second generation *Sun Simba* modules.

STATEMENT OF ORIGINALITY

Except where noted, the results presented in this thesis were obtained by the author during the period of his MA.Sc. research under the supervision of Dr. Henry Schriemer and Dr. Karin Hinzer. They are to the best of his knowledge original.

ACKNOWLEDGMENTS

I owe a large debt of gratitude to all of those who have provided the support and knowledge over the years to make this thesis possible. Though their names are not on this work, their contributions to this thesis were of no small part.

I have been amazingly fortunate to have supervisors with the patience, understanding, and willingness to give their students the freedom to explore that served as the basis of one the most rewarding and enriching experiences in my life. I have grown immensely as both a person and a researcher under their guidance. Specifically, I am deeply grateful to my supervisor, Dr. Henry Schriemer, for the thorough reading of this work and the detailed comments that lead to its completion. The countless hours and endurance that it took to provide such insightful feedback is greatly appreciated. I am also deeply grateful to my co-supervisor, Dr. Karin Hinzer, for the questions and constructive criticisms given over the years that taught me to refine my arguments and grow as a researcher. Her positive attitude and joyful spirit was uplifting and a constant source of inspiration. I can only hope to one day become as great a supervisor as Henry and Karin were to me.

I am extremely grateful to Dr. Joan Haysom for her unyielding support and guidance over the tenure of this work. There was never an issue or question I could bring to her that she couldn't address. Her passion, industriousness, and pro-activeness were engaging qualities I quickly came to admire and one day hope to replicate.

I am thankful to Matt Wilkins for always being there to address my technical questions and being an endless source of knowledge.

Jafaru Mohammed brought a skillset well outside of my abilities that significantly improved the data storage systems and the efficiency of data analysis. Completing this work would have been much more challenging without his assistance and ongoing support. I am greatly indebted.

Most importantly, this work would not have been possible without the love and support of my parents. The thank you I wish to write might eclipse this thesis, but since this is not practical in this instance, something much shorter will have to do. Thank you Mom and Dad for the financial and emotional support you have so freely provided over the years. You were always a source of strength and drove to push me through the toughest of times to get this work completed. Without you, I would be nothing, and because of your support, I feel I have everything. Thank you.

Finally, I am grateful to all those involved on the APECS project, including Morgan Solar Inc. This project has helped me to grow and learn on many different levels and provided an experience I will cherish forever.

TABLE OF CONTENTS

LIST OF FIGURES

1. Introduction

Energy plays an integral role in modern civilization as it centrally impacts social welfare by enabling economic development. In large measure the distribution and availability of energy correlates with a society's standard of living. However, most of the energy is sourced from non-renewable fossil fuels such as coal or oil. The overall energy production of fossil fuels is approaching its peak under present economic recovery scenarios. The expected decline of oil production by 2020 may create an energy gap that other fossil fuels cannot fill [1], absent significant economic or technological changes in their production. The extraction and exploitation of such fossil fuels negatively impacts biosystem and ecosystem health through pollution and habitat disruption, and may have deleterious impact on global climate patterns. These impacts will likely be exacerbated by increasing world populations, in particular through the enhancement of living standards in poorer regions [2], and the ever higher energy demands needed to satisfy human desires. A significant paradigm shift in energy use and development appears to be necessary to responsibly address long term energy requirements in a more sustainable fashion. Absent a source of "endless free energy" (such as the ever touted, but never realized, nuclear fusion), renewable energy sources may be able to achieve the goal of more equitable energy production with smaller environmental impacts than is allowed by the present hydrocarbon approach. Integrating a mix of different renewable energy sources into the electrical grid in incremental fashion can allow the transition to a new energy future to be accomplished while safely meeting current energy demands. Of all renewables, such as wind, biomass, and photovoltaics (PV), PV is one of the most attractive options to pursue due to its scalability, portability, very low operating expense and small environmental impact.

At the heart of a PV energy system is the photovoltaic cell, which converts photons into harvestable electrical energy through the photoelectric effect. The current cell technologies that exist are summarized in Figure 1-1. Of these, crystalline silicon PV systems currently have more than 85% of the market share with thin film technologies (such as CdTe and amorphous silicon) most of the remainder [3,4]. However, there are other PV technologies that possess superior efficiencies with the potential to change the market once they reach maturity. One of the technologies that may be poised to do so is concentrated photovoltaics (CPV). CPV systems concentrate sunlight onto a small area of expensive but high efficiency III-V multijunction PV cells. These high performance PV cells are nearly twice as efficient as crystalline silicon solar cells [5,8] as multiple junctions absorb a different portion of the incident solar spectrum. This enables higher overall absorption and ultimately higher efficiency. Further increasing the efficiency of the CPV cells is the fact that PV cell efficiency is increased at high concentrations of light. However, CPV systems must track the sun since they must make use of concentrating optical systems – they can only use direct normal incident (DNI) light. This makes capital expenditures much higher than for fixed flat panel systems, and also increases operational expenses. Despite this, CPV remains a promising technology since total system efficiencies are now about 8% higher than that of crystalline silicon PV technology [5-7]. Since the efficiencies

of the latter have approached fundamental limits, while those of CPV are nowhere near theirs, the potential advantages and performance gains of CPV cannot be ignored. CPV thus needs its levelized cost of energy production reduced to attract potential investors. This can best be done by improving system reliability, improving system efficiency, and leveraging the economies of scale that develop as CPV matures.

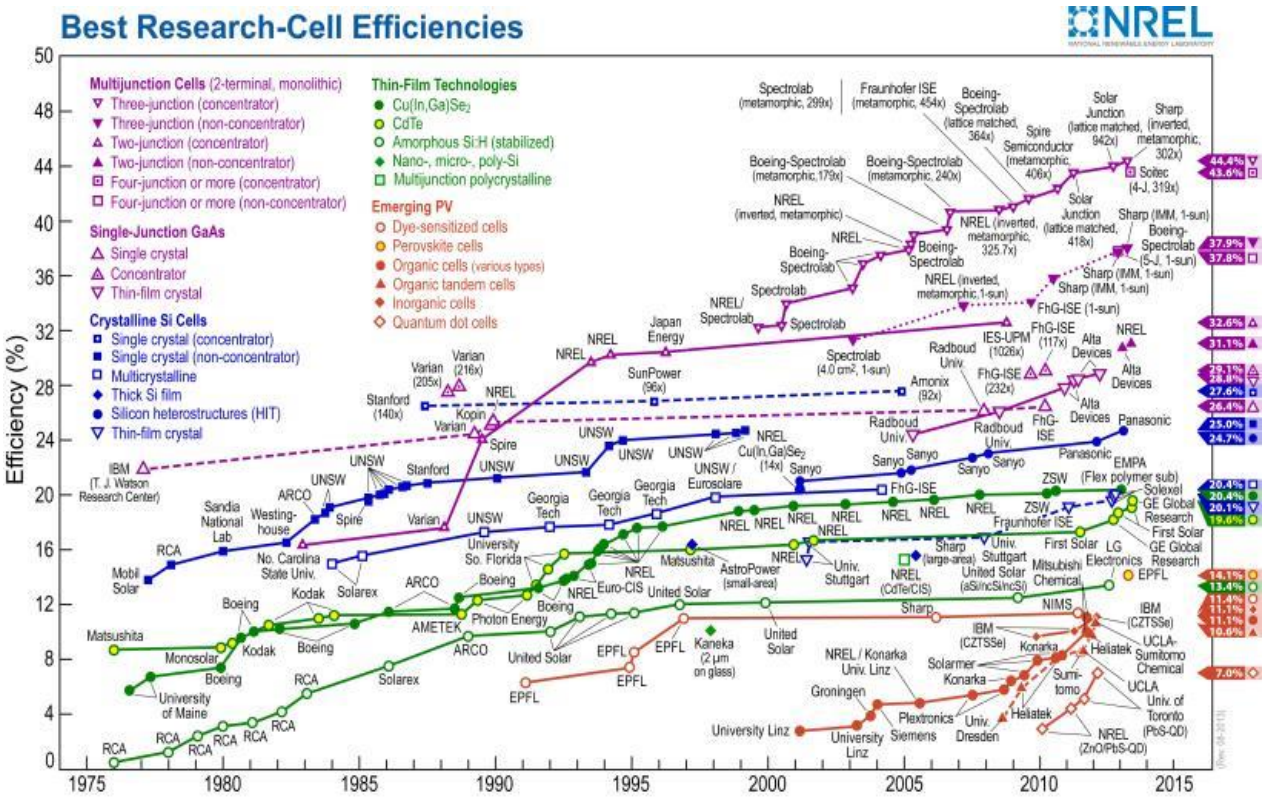

Figure 1-1: Best research cell efficiencies of different PV technologies. Multijunction cell's used in CPV systems nearly twice as efficient as crystalline Si cells. Chart produced by NREL [8].

A test site with significant cold weather extremes and strong variation in low DNI light is one of two critical locations to validate CPV technology, the other being one with significant warm weather extremes and little variation in high DNI light. This thesis describes the realization of two such test sites, one in Ottawa, ON, and one in Little Rock, CA, respectively. Due to time constraints, the focus is primarily on the former, since it acted as the prototype installation and development site for the latter. The performance analyses needed to identify system inefficiencies and areas for improvement are largely based on early generations of the novel CPV light guiding technology developed by Morgan Solar Inc. (MSI), a partner in the "Advancing Photonics for Economical Concentration Systems" (APECS) project, of which this research is a part.

To reduce CPV system costs, MSI, a Toronto based solar-energy start-up, has developed an innovative low cost and lightweight CPV module known as the *Sun Simba*. The traditional CPV modules make use of mirrors or lenses to focus light onto the cell. This results in bulky and

heavy modules with relatively expensive material costs. To overcome this, MSI has developed a light-guiding optic that makes use of total internal reflection to concentrate light onto the cell. This innovative design significantly reduces the CPV module's size and material costs relative to competing CPV modules, making it a potential game changer in the CPV industry. For intellectual property reasons the nature of the light guiding optic will not be considered in this work. Since *Sun Simba* is an emerging technology, rigorous testing and reliability studies were needed to advance market readiness through performance characterization and issues identification. To this end, an outdoor PV test facility was constructed at the University of Ottawa (uOttawa) to study the performance of the *Sun Simba* and to gather site-specific insolation data. The test site consisted of two 2-axis solar trackers, a comprehensive measurement system, and a remote data storage system. Further to this, a facsimile of this test site was also constructed in Little Rock, California with the future aim of comparing PV module performances between the two locations. The design, specifications, implementation, and the associated challenges for both of these systems are described in detail in this thesis.

1.1 Thesis Overview

This thesis comprises six chapters, of which this chapter is the first. It describes CPV's current standing relative to competing PV technologies and the need to reduce its levelized cost of energy if it is to ever occupy a sizeable portion of the PV market share. A brief description of the MSI technology is introduced providing the context and motivations behind the work presented in this document.

Chapter two introduces the theoretical concepts and tools related to CPV and takes a top-down approach starting from the solar resource, thence to the optics and finally to the cell. First, the solar resource and the factors affecting its properties are described. The different types of tracking and optical systems currently used are described. An overview of the operation of the PV cell is given along with some of the fundamental physical laws that describe its properties and its performance. The basic properties of the multi-junction cell are also documented. Finally, heat transfer concepts are introduced to ensure a basic understanding of the heat transfer physics behind the thermal modelling done in Chapter 3.

A finite element numerical thermal model is developed in Chapter three to model the heat transfer of a cell-on-carrier assembly. Since the cell efficiency drops with rising temperature, it was constructive to relate the carrier design to cell efficiency. With this model, potential improvements of the optimal geometrical configurations of the carrier are explored. Both carrier form factor and channel configurations are studied. Moreover, the choice of insulator, typically a ceramic, is studied as its thermal conductivity affects the heat transfer of the carrier. The effect of the heat sink cooling power on the cell temperature is considered. Solder voids that exist between the cell and carrier are also modelled. This is done to ascertain the void conditions that lead to cell failure.

In chapter 4, the design of the test systems at uOttawa and Little Rock are described. Basic specifications of system components are provided. The associated design choices are explained, the challenges experienced are described, and an overview of the issues related to the uOttawa test site trackers is given. The misalignment of the installed MSI modules is quantified and the subsequent corrective methodology is explained. The data storage component of the system and the user friendly data interfaces are described.

In chapter 5, some brief analyses of specific system properties are outlined. First, a long-term performance analysis of the MSI optics is given. This analysis makes use of the IEC 60891 [45] standard to correct the measured quantities to a standard reference condition to ensure equitable performance comparisons. An unexpected hysteresis characteristic of the current output of some of MSI optics was explained with the help of the instrumentation. Finally, the thermal numerical model and the measured data are used to estimate the heat sinking performance of the MSI modules installed at the uOttawa test site.

In chapter 6 a summary of the test system performance at uOttawa is given. The modelling and analyses results are also summarized. Gaps remaining in the understanding of the system performance and modelling are illustrated and suggestions for future work to fill in these gaps are provided.

2 Theory

Successfully moving towards efficient and cost-effective concentrating photovoltaic (CPV) system designs relies upon the knowledge of the elements that make up the system. The depth of knowledge of each system element dictates the technical leverage available to minimize the overall system losses. Beyond that only the design, the environmental, and the financial constraints can limit system performance. Thus, a detailed understanding of the theory behind CPV systems is crucial to achieving optimum system performances. The primary elements that make up a CPV system and the types of associated losses are shown below in Figure 2-1, which outlines the order that a CPV system follows to efficiently convert sunlight (photons) into electrical energy. To begin, a CPV system starts with an understanding of its energy source, the sun. The nature of the sun and the effect that the atmosphere has on sunlight must be understood. Next, a means to track the sun and optics to focus the light must be described. Then the performance of a solar system under various operating conditions needs to be quantified in order to optimize performance. Finally, the generated electrical energy must be converted into useable or standard forms. This chapter follows this structure to understand the sources of loss and to better appreciate their effects downstream. The expected behavior of a practical CPV system will also become apparent. Furthermore, for each of the elements, significant research effort must be dedicated to overcome many inherent challenges. The scope of this work consists of the design of a CPV test system for a research-stage technology, its realization and subsequent performance analysis. This work also addresses fundamental aspects of cell-on-carrier thermal optimization. To summarize, this chapter will specifically focus on the theoretical aspects and derivations behind CPV performance metrics and heat transfer aspects during the description of the CPV system elements.

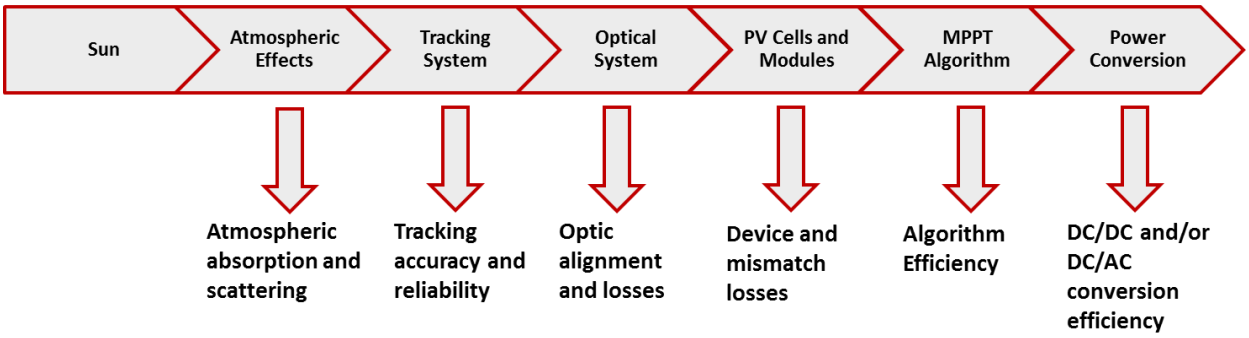

Figure 2-1: PV system elements and their associated loss mechanisms.

2.1 The Sun, the Atmosphere and the Solar Spectrum

The sun is at the heart of our solar system and it fundamentally sustains all life on earth. The sun, a massive ball of plasma, provides both the gravitational forces that keep the earth orbiting the sun, and the energy to drive processes required for life on earth – such as photosynthesis, rain, and convection currents. Being predominantly hydrogen, the sun converts hydrogen into helium through a thermonuclear reaction within its core. The radiation emitted from the core then

traverses the radiative and convection zones, eventually emerging from the photosphere, which has an approximate blackbody temperature of 5800K. For an earth-sun distance of 1.50 x 10^9 km, the generally accepted extraterrestial solar irradiance of 1366.1 W/m^2 [9, 10]. The extraterrestial solar irradiance is relatively stable but does vary slightly for several reasons. Primarily, the ellipticity of the earth's orbit causes it to vary by as much as 3.39 % [11]. This fluctuation occurs slowly over the course of the year as the earth travels through its elliptical orbit. Other sources of fluctuations result from solar oscillations, sunspots, and other solar anomalies. In addition, knowledge of the spectral content of the sun's irradiance and those factors that alter its spectrum are necessary in optimizing and characterizing CPV systems.

2.1.1 The Blackbody

A *blackbody* is an idealized object that absorbs all electromagnetic radiation falling upon it. In thermal equilibrium, its emission spectrum is governed by the Planck distribution, which states that the emissive power of an ideal blackbody is the power emitted per unit area in the wavelength range of λ to $\lambda+d\lambda$ [12]. The Planck distribution can be expressed as,

$$E(\lambda, T) = \frac{2\pi hc^2}{\lambda^5 (e^{\frac{hc}{\lambda kT}} - 1)}, \tag{2.1}$$

where E is the power unit area, k is the Boltzmann constant, c is the speed of light, T is the mean temperature of the blackbody, λ is the wavelength, and h is the Planck constant. As seen in Figure 2-2, the emission spectrum of an ideal blackbody is dependent on temperature. Specifically, as an object's temperature increases its emission shifts to shorter wavelengths. This is precisely why we can observe a metal turning red and eventually white as its temperature continues to rise. While an ideal blackbody does not exist, the emission spectra of some objects can be approximated very well with blackbody curves.

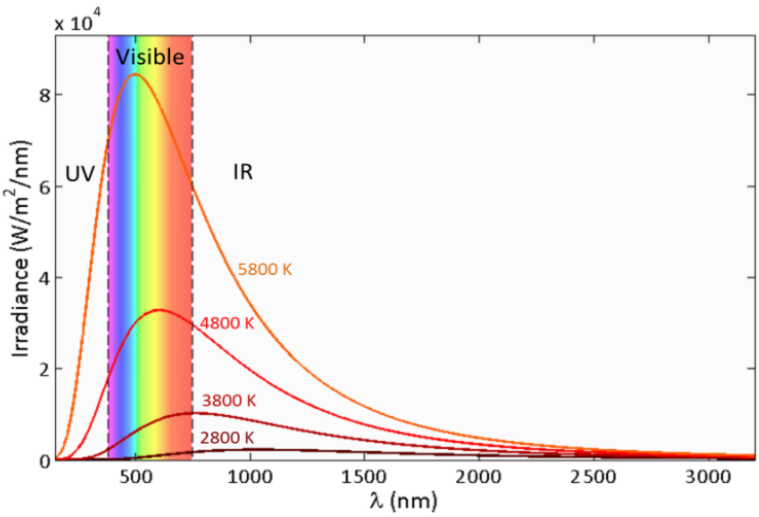

Figure 2-2: Blackbody curves at various temperatures. The higher the temperature of an object, the more electromagnetic radiation it emits.

2.1.2 The Atmosphere

As sunlight passes through the earth's atmosphere it is significantly affected by cloud cover and the atmospheric constituents that both absorb and scatter light. This has a significant effect on the solar spectrum observed at the earth's surface, particularly the irradiance – the integrated spectral intensity. Sunlight reaching the earth's surface consists of the direct beam sunlight (direct irradiance) that makes up approximately 90% of the total solar energy, and the diffuse sunlight that makes up the remainder of the available solar energy. The diffuse portion is made up of light scattered by the atmosphere and light that is reflected off the ground. The sum of the direct, diffuse, and reflected irradiance is known as the global irradiance. The direct normal irradiance (DNI) is the irradiance measured on a surface normal to the sun's rays and it is the only harvestable portion of the solar energy in CPV systems. This is because the DNI is made of near-parallel rays that can be focused onto the cell whereas the diffuse and reflected components are coming in many different directions and cannot be focused. However, diffuse and reflected components can be harvested by flat plate PV systems and so contribute to the energy produced by these types of systems. Finally, the dominant atmospheric constituents that absorb sunlight in their specific wavelength ranges are (in no particular order) ozone (O_3), oxygen (O_2), methane (CH_4), nitrous oxide (N_2O), carbon dioxide (CO_2), and water (H_2O), as illustrated in Figure 2-3. These considerably alter the solar spectrum reaching earth's surface.

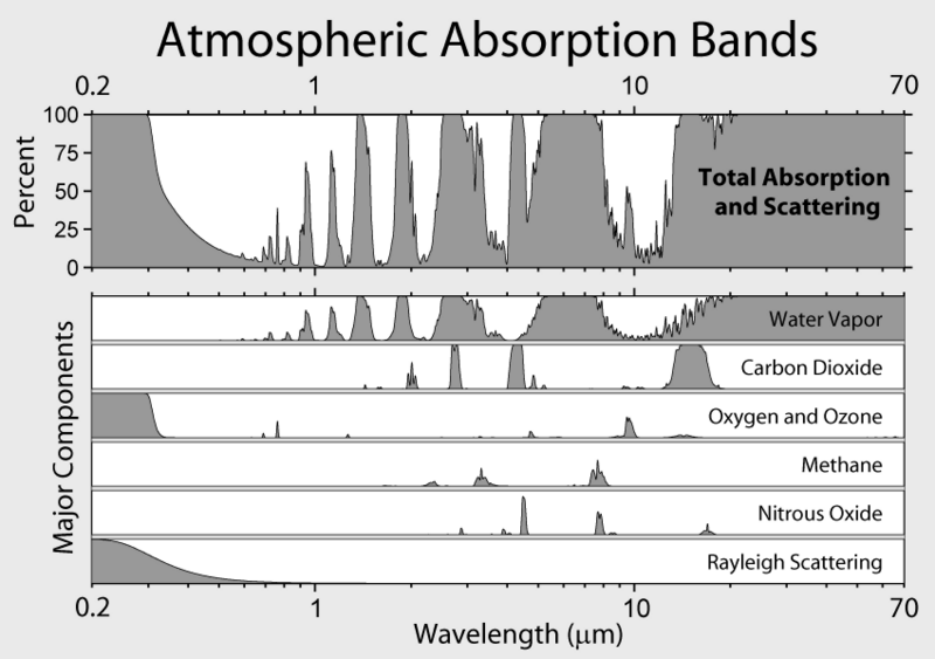

Figure 2-3: The major atmospheric constituents that affect the sunlight that reaches the earth's surface. The absorption and scattering of various atmospheric constituents is shown (Copied from [17]).

2.1.3 Tracking the Sun

CPV systems take advantage of their increased cell efficiencies at higher concentrations by focusing light with an optical system. This requires that the nominally parallel rays light impinge normal to the focusing lens or device. Hence, the apparent motion of the sun from the earth's

surface must be well understood if the CPV system is to harvest the sun's energy. This understanding begins with the knowledge of the earth's orbit around the sun as well as the earth's rotation and tilt with respect to the sun.

To specify the sun's position, a coordinate system is needed. From the surface of the earth, we can define the sun's position with two co-ordinates if we assume the earth-sun distance relatively constant. The sun's elevation or altitude, θ, is the angle between the sun's position and the point directly overhead. Likewise, the sun's azimuthal angle, ω, is the angular position of the sun east or west of south. In this way, ω=0° is facing south and values of ω less than zero imply an east-facing orientation whereas values of ω greater than zero imply a west-facing orientation.

The earth moves around the sun at an average speed of 108 000 km/h in a slightly elliptical orbit. The period of the orbit is approximately 365 earth days (*i.e.*, one year). Being elliptical, the mean earth-sun distance is approximately 1.496 x 10^{11} m; the actual distance varies with the day number, *n*, as [14]

$$d = 1.496 \times 10^{11}\left[1 + 0.017\sin\left(\frac{360(n-93)}{365}\right)\right], \tag{2.2}$$

where January 1st is considered the first day of the year (n=1). The aphelion, or point that the earth is farthest from the sun occurs around July 4th (n=185). The earth is closest to the sun (perihelion) on January 3rd (n=3). The earth's orbital ellipticity is illustrated below in Figure 2-4. Furthermore, as the earth moves about the sun it spins on its polar axis, completing a full rotation in approximately 24 hours (or one day). With respect to the earth-sun orbital plane, the earth's polar axis is inclined at an angle of 23.45°. This inclination causes the apparent motion of the sun to change over the course of the year and is also the cause for the change of seasons. Particularly, in the northern hemisphere we observe longer sunlight hours in the summer and shorter sunlight hours in the winter, with the sun tracking higher in the sky in the summer. Solar noon, the point where a shadow points directly north or south, depends on latitude. Solar noon with the sun directly overhead occurs at the Tropic of Cancer (23.45°N) on the summer solstice, at the Tropic of Capricorn during the winter solstice (23.45°S) and at the equator during the spring and fall equinoxes. Over the course of a year the declination angle, δ, which corresponds to the latitude where the sun is directly overhead at solar noon, varies as

$$\delta = 23.45°sin\left(\frac{360(n-80)}{365}\right), \tag{2.3}$$

where *n* is the day number of the year and n=1 on January 1st. Furthermore, the solar declination can be used to determine the sun's elevation at solar noon for any given latitude as such,

$$\theta_{solarnoon}(n) = 90° - latitude + \delta(n) \tag{2.4}$$

.

The amount of time the sun spends above the horizon, or amount of sunlight hours, is directly tied to the latitude and time of year. This dictates the elevation the sun reaches in a day and how quickly the sun rises or sets. Also, the distinction and relation between clock time (CT) and solar

time (ST) must also be made since the world runs on clock time. Thus, the equations that fully define the sun's position (given the latitude, the longitude, and the clock time) are a complex but straightforward set. However, a complete description of the mathematics behind calculating the solar position is beyond the scope of this chapter. Full mathematical descriptions can be found in [13, 14].

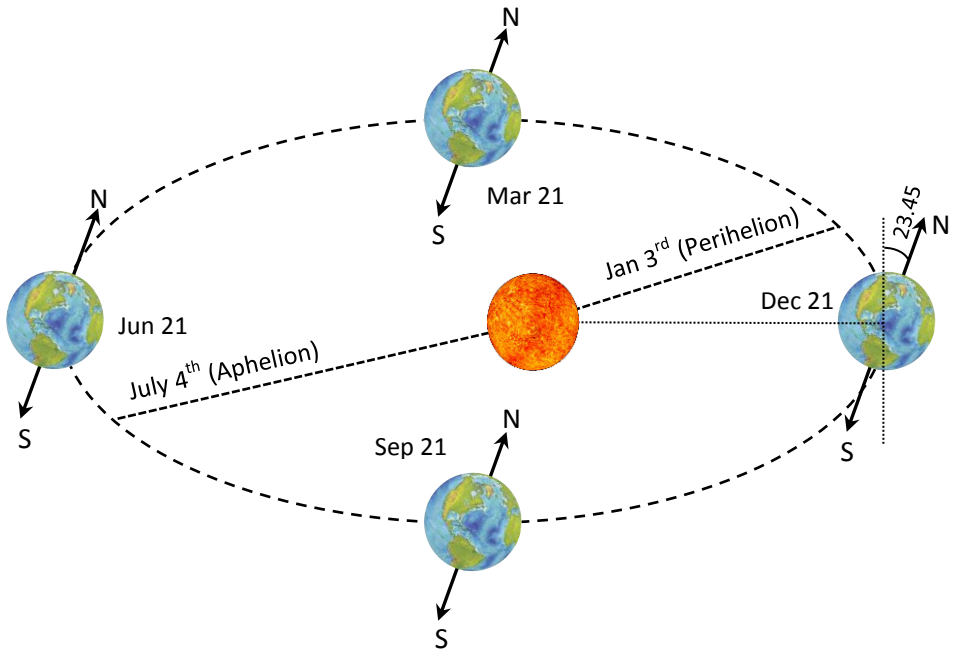

Figure 2-4: Earth's orbit around the sun where the aphelion (furthest from the sun) and the perihelion (closest to the sun) are noted. The summer and winter solstices occur on June 21st and December 21st, respectively. The autumnal and spring equinoxes occur on September 21st and March 21st, respectively.

Air Mass

The amount of atmosphere light has to travel through to reach the earth's surface affects the radiation reaching the surface of the earth at a particular point. This measure is known as the *air mass* (AM) value. As an example, when the sun is directly overhead and skies are clear the sunlight has to pass through the equivalent length of one atmosphere. Thus, the AM value in this case would be one, or AM1. As the sun moves closer to the horizon, the sunlight has to pass through a greater path length of atmosphere and the AM value must increase. Thus, the air mass value is only dependent on the sun's elevation as [12-14,18]

$$AM = \frac{1}{cos\theta}. \tag{2.5}$$

Of course, the atmospheric density changes with depth so this value is based on the assumption that the atmosphere is non-refractive and homogenous. Close to the horizon this air mass calculation can produce an error of up to 10% [19]. Nevertheless, this metric is commonly used in industry to describe the radiation conditions for test and measurement. In fact, AM1.5 is the accepted industry standard for photovoltaic measurements. AM0 refers to the extra-terrestrial irradiance at the earth orbit before it passes through any atmosphere. For the testing of CPV

systems, a standard spectrum known as AM1.5D is used, where the '*D*' indicates that the spectrum only includes the direct beam portion of the sunlight [16]. A comparison of the extraterrestrial spectrum, the AM1.5D spectrum, and a 5800K blackbody curve is given in Figure 2-5. The small but noticeable spectral differences between the sun and an ideal black body are apparent, as are the absorption and scattering effects of the atmosphere (AM0 spectrum compared to the AM1.5D spectrum).

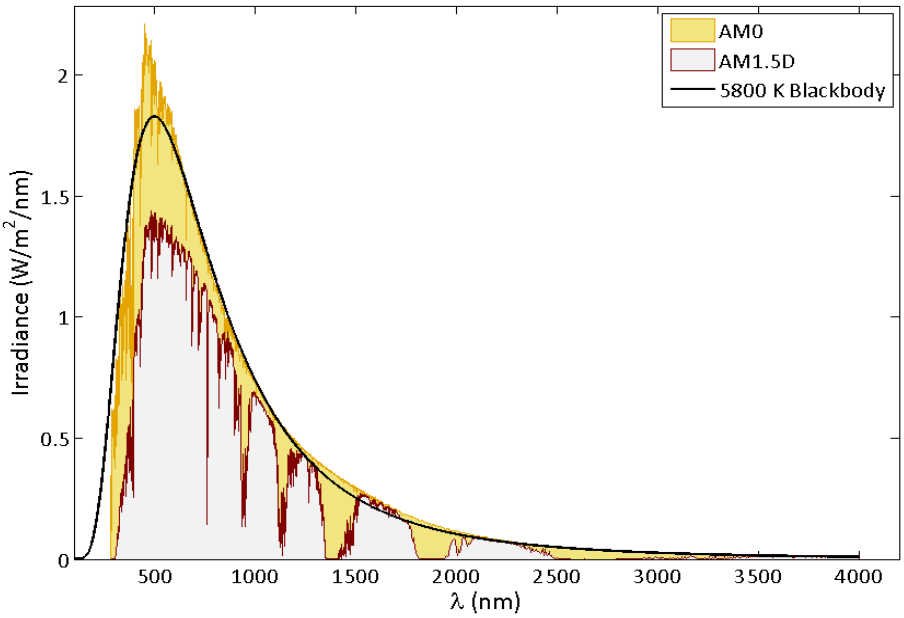

Figure 2-5: Comparison of extra-terrestrial (AM0), terrestrial solar spectra (AM1.5D) and an ideal 5800K ideal blackbody.

2.2 Tracker's and Optical Systems

Solar thermal systems and PV systems are the two main methods of converting solar energy into electricity. Different technologies and methodologies exist for either of the approaches. Only concentrating PV systems will be discussed in this thesis. All CPV technologies make use of optics to focus sunlight onto a photovoltaic cell, both to take advantage of the cell's greater efficiency at higher concentrations and to trade off the more expensive PV cell costs against the cheaper concentrating optics. Various levels of concentration can be achieved depending on the optical design. Typically, low concentration PV (LCPV) technologies employ concentration factors below 100x, based on reflective mirror technologies, and use monocrystalline silicon cells [23]. Low concentration technologies may or may not use solar trackers. High concentration PV (HCPV) technologies range in concentrations of 300x and up and are the focus of this work [23].

Typically, HCPV technologies use high-efficiency multi-junction cells to leverage the high efficiency of these cells at fairly high concentrations. This is shown in Figure 2-6 where a

typical quantum dot enhanced cell (QDEC) from Cyrium Technologies Inc. exhibits a maximum efficiency at about 500 suns [20]. However, as the concentration factor increases, the angular acceptance of the optical system decreases. Consequently, the higher the concentration ratio of the optical system, the higher the required solar tracking precision. This also impacts the nature of the optical train: CPV systems can employ a single primary optic, but a secondary optic is often used to reduce chromatic aberration and improve the angular acceptance by evenly distributing the photon flux on the cell.

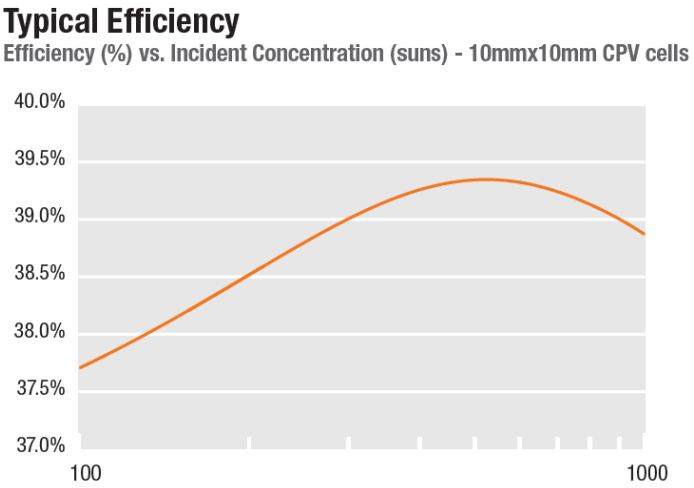

Figure 2-6: Efficiency as a function of concentration for Cyrium's QDEC multi-junction solar cell (Copied from [20]).

Dish and heliostat systems are examples of one approach to HCPV technologies. Such systems use reflective optics to concentrate light onto dense-array multi-junction PV cells. Due to the very high heat flux, these cells require active cooling to keep them at their operating temperatures. Heliostat systems use dispersed rotating mirrors to reflect light onto a stationary, centrally located, dense array of PV cells. Alternatively, dish systems use a parabolic reflector to focus light onto a dense array of PV cells. Figure 2-7 shows a 500 kW CPV dish type system installed at Bridgewater, Australia [21]. Pole mount trackers are used for such systems, which have the advantage of using minimal ground space. However, these types of trackers require a strong concrete base buried well beneath grade to handle the weight and wind loading requirements. Cassegrain reflectors can also be used in dish configuration, as can other optical configurations.

Figure 2-7: Installed SolarSystems CPV dish system that makes use of reflective mirrors to achieve concentration (Taken from [21]).

Lens-based concentrating optics are the most commonly used designs in CPV applications. Fresnel lenses are typically used as primary optics because their small thicknesses limit the CPV panel's weight and volume. The reduced lens thickness comes at the expense of poor imaging, which is not a concern in CPV systems. A secondary optic, a homogenizer, is often included to help reduce chromatic aberration and to improve the uniformity of the light flux on the cell. This helps to improve performance by optimizing optical coupling to the cell, and by improving the angular acceptance of the optic, as shown in Figure 2-8 [22].

Various different CPV solutions exist in the emerging CPV market. Suncore, a joint venture between Emcore and Sanan Optoelectronics, have begun to position itself in the CPV market with its own lens based CPV module. A tilt and roll tracking system is being used, which allows many modules to be placed on a single tracker as shown in Figure 2-9. However, the focus in this thesis will be on Morgan Solar Inc. "flat panel" light-guiding modules implemented on a Golden Sun GS3500 ring type tracker. The advantage of the ring tracker is that it is able to be installed above ground without any trenching or digging. It is mounted on, and self-ballasted by, large concrete forms. The drawback is that the tracker base has a relatively large footprint on the ground and it sits closer to the ground. A Morgan Solar Savannah tracker, installed at Little Rock, California, is shown in Figure 2-11. The Savannah tracker is a self-ballasted box-frame style tracker with four individual tracking heads. Installed on each of the tracking heads are panels of Morgan Solar's third generation Light-guide Solar Optics (LSO).

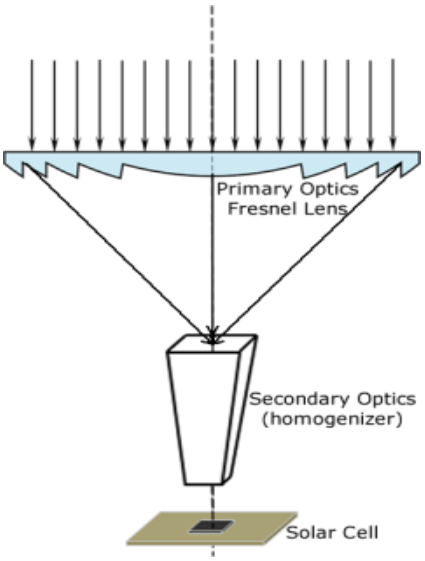

Figure 2-8: Typical optical configuration of a lens based CPV optic. Light is focused by a primary lens, which then passes through a homogenizer to achieve a uniform distribution of light on the cell (Copied from [22]).

Figure 2-9: Suncore CPV panel on tilt and roll tracker.

The Golden Sun tracker was outfitted with Morgan Solar light-guiding optics at the University of Ottawa. Morgan Solar has a proprietary light-guiding optic, using nonimaging waveguiding technology to concentrate light onto the PV cell rather than the more typical imaging optics. This light-guiding approach means lighter weight, smaller volume, and potentially cheaper materials can be used than appear in Fresnel lens and reflective based CPV systems [24]. Concentrating by light-guiding is accomplished with two layers to redirect the light. The first layer known, as the deflection layer, refracts the light in such a way that it couples into the second light-guiding layer (LGL). The LGL layer is the waveguiding layer and through internal reflection guides the light to the PV cell. The Morgan Solar optic is shown below in Figure 2-10, compared to other common approaches currently used in CPV.

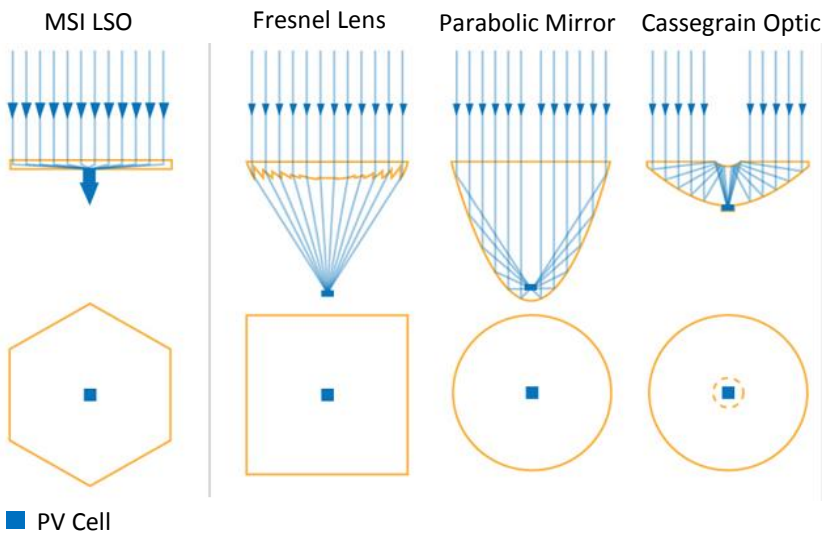

Figure 2-10: Comparison of Morgan Solar's light-guide optic compared to other conventional CPV optical configurations (Taken from [24]).

Figure 2-11: Implementation of Morgan Solar's Gen III LSO optic panels on a box-frame tracker.

2.3 Cell Electrical Properties

Solar cells, also known as photovoltaic (PV) cells, are semiconductor devices that convert light into electrical energy. The stream of photons yields a current, the voltage being set by the band gap of the semiconductor material. The process arises from local photon-matter interactions in photovoltaic material. Photons with energies above the band gap liberate electrons from the atoms to which they were originally bound. An electric field built into the solar cell then sweeps the electrons out of their generation region to deliver an electrical current to a load connected

externally to the solar cell. Understanding the process behind this energy conversion requires a basic understanding of solar cell physics.

2.3.1 Semiconductors

Solar cells, like most semiconductor devices, are most often made from group IV elements such as silicon or germanium. A silicon atom, for example, contains four valence electrons. Consequently, each silicon atom forms covalent bonds with four adjacent silicon atoms producing an ordered crystalline silicon solid. As the temperature of the silicon material increases electrons are freed from their atomic nuclei and are able to flow as electrical current. Thus, as the temperature of the silicon increases so does its conductivity. However, the conductivity is still small at ambient temperatures. Adding a relatively small amount of dopants to the pure (intrinsic) silicon semiconductor significantly increases the conductivity of the silicon. Often, phosphorous atoms are used to dope intrinsic silicon; a density of one phosphorous atom for every one thousand silicon atoms is not atypical. Four of the five phosphorous atom's valence electrons are tightly bound by covalent bonds with surrounding silicon atoms. The fifth electron is free to move about the crystal structure. Also, the phosphorous atom is left as a positive ion once the fifth electron moves away. Thus, the material remains electrically neutral but contains free electrons or carriers. Doped materials such as this with free negative charge carriers (electrons) are known as n-type materials. Similarly, doping a semiconductor with a dopant such as boron forms a semiconductor with positive charge carriers and fixed negative ions since boron possesses only three valence electrons. One boron atom for every ten million silicon atoms is typical in silicon. Moreover, the positive charge carriers are commonly referred to as holes. Holes are the absence of electrons and appear to move about the crystal lattice the same way a particle would and so it is helpful to treat them as such. Materials with free positive charge carriers (holes) are referred to as p-type materials. Furthermore, group III and group V elements can be used together, such as Gallium Arsenide (GaAs), to form a compound semiconductor. III-V materials are currently used in multi-junction solar cells as they provide the most extensive design space, particularly in their ternary and quaternary forms. II-VI materials such as Cadmium Telluride (CdTe) are also used to make semiconductors [14], but these are for lower efficiency thin-film solar cells.

2.3.2 The PN-Junction

We now consider forming a pn-junction by joining a p-type material with an n-type material, as shown in Figure 2-12. When this junction is formed, the free electrons in the n-type material diffuse towards the p-type material where they occupy the holes in the p-type region. In so doing, the electrons leave behind immobile positive charges in the n region. Likewise, holes in the p-type material diffuse towards the n-type material and can also be understood as occupying electrons in the n-type region. As these holes diffuse away from the p-type material they leave behind immobile negative charges. These immobile ions create an electric field that opposes the diffusion of the charge carriers. With continuing diffusion, the electrical field grows larger until the diffusion of charge carriers ceases. The exposed immobile charges that form the built-in

electric field are all found near the junction and form what is known as the depletion region since it is depleted of charge carriers. Forward biasing the pn-junction applies an electric field that opposes the built-in electric field. Once the applied forward bias is greater than the built-in voltage the charge carriers are then able to diffuse across the junction once again and current flows freely through the device. On the other hand, if we apply a negative voltage across the terminals, a reverse bias, then we are reinforcing the electric field across the junction. Thus, the only current that flows in the device is a result of thermally generated charge carriers that get swept across the depletion region. This current is known as the reverse saturation current, I_o. Now if we sweep the bias voltage across the pn-junction we would measure a current-voltage (IV) curve. This curve is described by the Shockley diode equation

$$I_{dark} = I_o(e^{\frac{qv}{nkT}} - 1)\ . \tag{2.6}$$

This describes a conventional diode, or a pn junction device without illumination, which is why the diode current is known as the dark current.

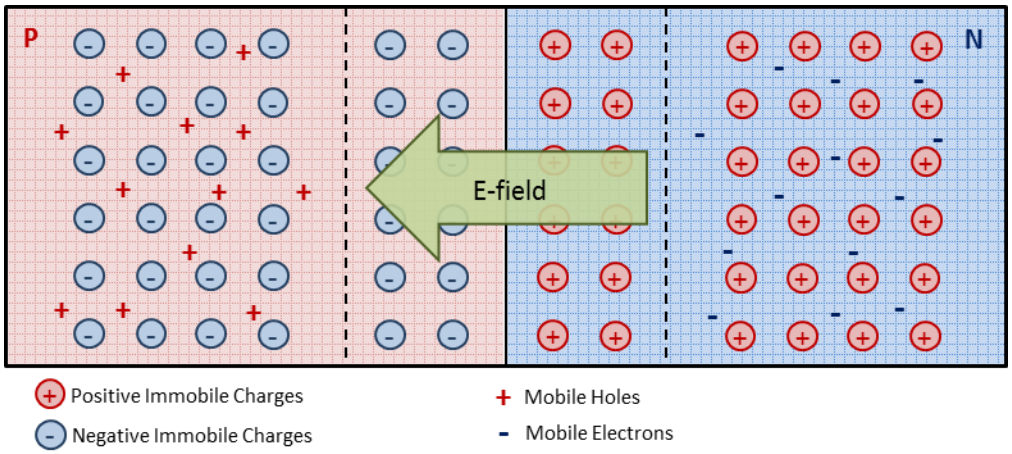

Figure 2-12: Illustration of charge separation in a PN-junction without external bias, which results in an internal built-in electric field.

If a diode absorbs photons, which would occur when exposed to sunlight, then the absorbed photons would create free electron-hole pairs in the diode. If these electron-hole pairs are created close enough to the junction, then the electric field will push the holes to the p side and the electrons to the n side. This charge separation at each end of the diode creates a voltage that can be used to deliver current to an electrical load. This photocurrent alters the Shockley diode equation as such,

$$I = I_{photo} - I_o\left(e^{\frac{qv}{nkT}} - 1\right) = I_{sc} - I_{dark}. \tag{2.7}$$

As demonstrated in Figure 2-13, the irradiance on the cell and the generated photocurrent are directly proportional. On the other hand, the open circuit voltage of the cell increases logarithmically with the irradiance.

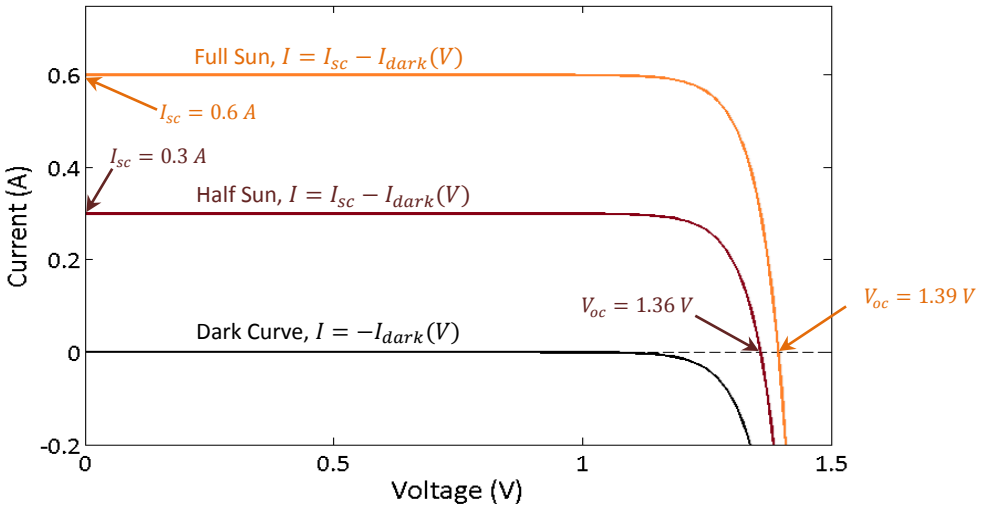

Figure 2-13: Effect of light-intensity on IV-curve. Short-circuit current increases linearly with irradiance whereas the open circuit voltage increases logarithmically with irradiance.

2.3.3 The impact of Band-Gap on Solar Cell Efficiency

An important property of solar cells is their absorption characteristics. Specifically, every semiconductor has a material-dependent bandgap energy, E_g. This bandgap energy is the energy required to free an electron from its atomic nucleus, allowing it to freely move about the crystal lattice and to contribute to current flow. Electrons bound to their nuclei are said to be in their ground (or valence band) state, whereas electrons that are free to move are said to be in the conduction band. Thus, the band gap energy is the energy required to move the electrons from the valence band to the conduction band, as shown in Figure 2-14. The energy needed to overcome the bandgap and move an electron from the valence band to the conduction band can come from sources such as heat (phonons) or light (photons). That is, at absolute zero there is no thermal energy available to move an electron to the conduction band. As the semiconductor heats up, an increasing number of electrons move to the conduction band, leaving holes behind in the valence band. In a pure material, electrons cannot occupy energy levels between the valence band and the conduction band.

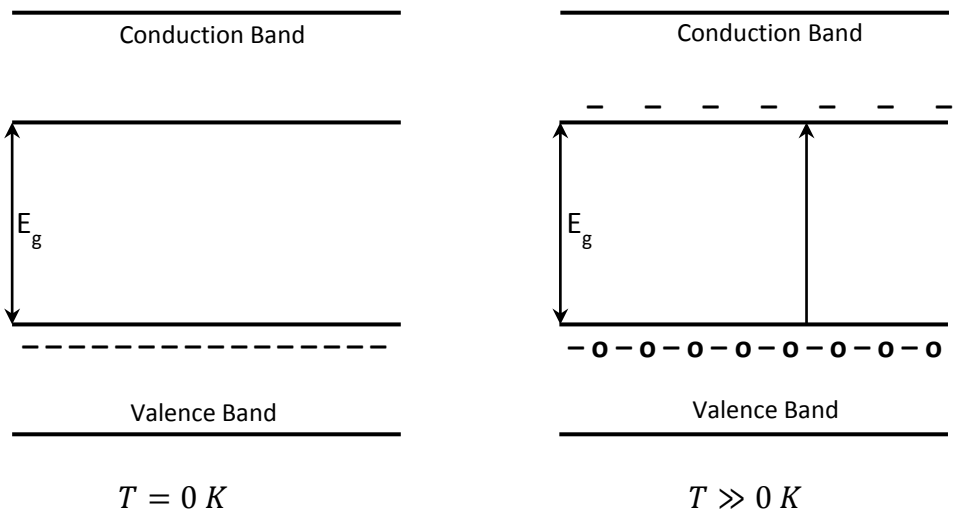

Figure 2-14: Availability of states in valence band and conduction band in a semiconductor at different temperatures (Adapted from [14]).

Phonons (heat) and photons (light) with energy equal to or greater than the bandgap energy create electron-hole pairs in a solar cell. The energy of a photon is dependent on its frequency (*f*), and thus inversely proportional to its wavelength (λ), as

$$E_{photon} = hf = \frac{hc}{\lambda}. \tag{2.8}$$

Therefore, photons incident on the solar cell with energy below the bandgap passes through the cell unabsorbed [13-15, 18]. Thus the cell appears transparent to photons below the bandgap and so the energy is lost. Photons with energy above the bandgap are absorbed and create electron-hole pairs with excess energy as seen in Figure 2-15. This excess energy is wasted as heat within the solar cell by a process called *thermalization* [13-15].

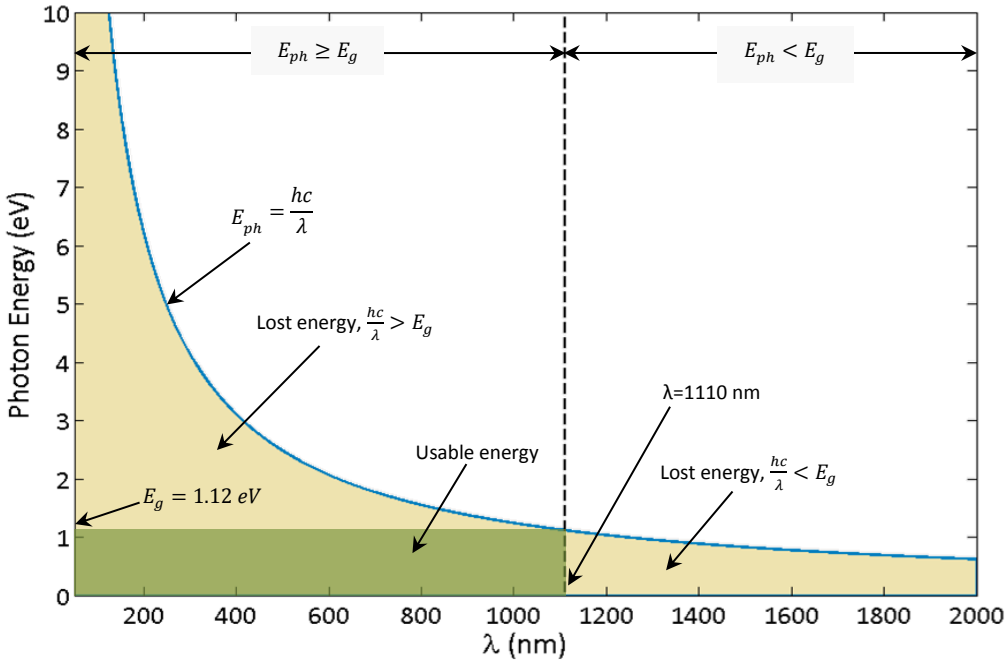

Figure 2-15: Photons with energy above the bandgap are absorbed and can excite electrons. Silicon has a bandgap energy of approximately 1.12 eV, which corresponds to absorption of photons with wavelength less than 1100 nm. Materials appear transparent to photons with energy below the bandgap. [Adapted from [13]].

2.3.4 Quantum Efficiency

The probability that an electron-hole pair is created when a photon of certain energy impinges upon the solar cell is known as its quantum efficiency (QE). The quantum efficiency of a solar cell depends upon its charge separation, its charge collection efficiency, and the absorption properties of the solar cell. Thus, it is a crucial parameter in determining a solar cell's performance under different spectral conditions and determining the photocurrent delivered by the solar cell. The photocurrent generated by a solar cell in short circuit is dependent on the product of the incident spectrum of light and the cell's quantum efficiency as [15]

$$I_{photo} = q \int b_s(\lambda) QE(\lambda) d\lambda \,, \tag{2.9}$$

where b_s is the photon flux density, which can be derived from the solar spectra.

2.4 Solar Cell Performance Characteristics

2.4.1 Ideal Equivalent Circuit Model

With a basic understanding of the solar cell operation we can now discuss the concepts and quantities used to characterize and measure a solar cell's performance. First, with an understanding of the solar cell operation and equation (2.7), an equivalent circuit model for an ideal solar cell can be constructed using a variable resistive load, R_L. When the terminals of the cell are shorted, setting R_L to zero, there is a zero voltage drop across the cell and the current I_{photo} is equivalent to the short circuit current of the cell I_{sc}; this can be verified from equation (2.7) by setting V equal to zero. Conversely, if the cell terminals are open circuit ($R_L=\infty$) then the

dark current has to precisely cancel the photogenerated current at V_{oc}. Thus an equivalent circuit consists of an ideal current source in parallel with an ideal diode, as shown in Figure 2-16. The open circuit voltage may be found by isolating *V* in equation (2.7) for *I*=0, which gives

$$V_{oc} = \frac{nkT}{q}\ln(\frac{I_{sc}}{I_o} + 1)\ . \tag{2.10}$$

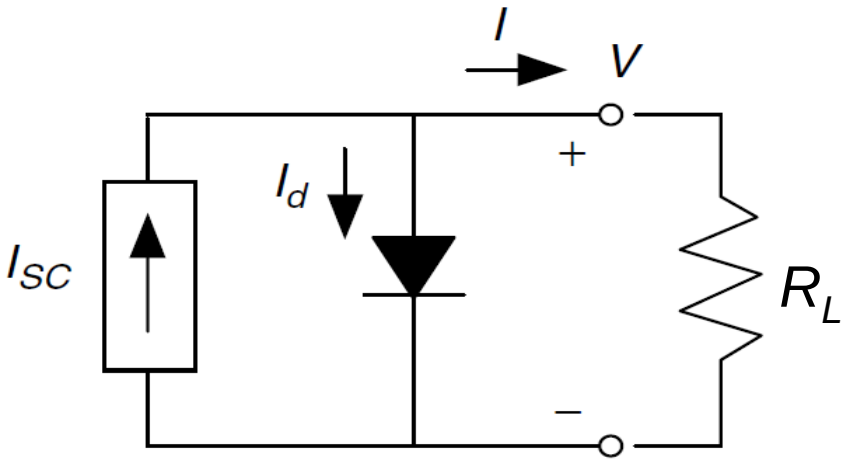

Figure 2-16: Ideal equivalent circuit model for solar cell (Taken from [13]).

2.4.2 Maximum Power Point and Efficiency

The two performance characteristics of a solar cell are I_{sc} and V_{oc}; I_{sc} is directly proportional to the solar irradiance on the cell and V_{oc} gives the bias range of operation. If the product of the current produced and the bias voltage is plotted against the bias voltage, a power-voltage curve is produced, as shown in Figure 2-17. Clearly, a point on the power curve exists showing where maximum power is delivered to the load; this is known as the maximum power point. The cell current and voltage at this particular point are known as the maximum power point current (I_{mp}) and the maximum power point voltage (V_{mp}), respectively. Thus, the optimal load on a solar cell is given by [15]

$$R_{optimal} = \frac{V_{mp}}{I_{mp}}\ . \tag{2.11}$$

Furthermore, the fill factor, which describes the squareness or 'idealness' of a solar cell's IV curve, is given by [15, 18]

$$FF = \frac{V_{mp}I_{mp}}{V_{oc}I_{sc}}\ . \tag{2.12}$$

The efficiency of a solar cell is calculated by [15, 18]

$$\eta = \frac{P_{mp}}{P_{inc}} = \frac{V_{mp}I_{mp}}{P_{inc}}\ , \tag{2.13}$$

where P_{inc} is the incident irradiance (power) on the solar cell. The efficiency can also be related to the fill factor by substituting equation (2.12) into equation (2.13), which gives [15, 18],

$$\eta = \frac{V_{oc} I_{sc} FF}{P_{inc}}. \tag{2.14}$$

In summary, the key performance metrics of a solar cell are V_{oc}, I_{sc}, fill factor, and efficiency.

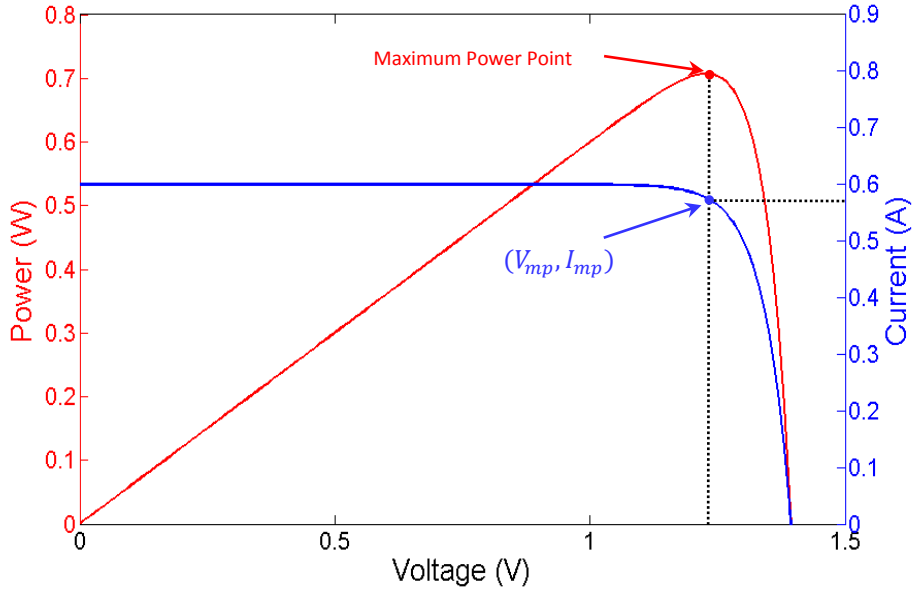

Figure 2-17: The solar cell power curve compared to the *I-V* curve. The maximum power point is indicated.

2.4.3 Non-Ideal Solar Cell

In practice, solar cells are not ideal devices and the generated power may suffer both shunt and series losses, the former through leakage currents past the solar cell, and the latter through resistive losses within the solar cell [13, 14]. A more accurate equivalent circuit model can be developed to address these effects, as shown in Figure 2-18. Here, a shunt resistance (R_{sh}) models the current leakage losses and a series resistance (R_s) models the cell's resistive and contact losses. Incorporating these parasitic resistances, the diode equation (2.7) now becomes [12-15, 18]

$$I = I_{sc} - I_o\left(e^{\frac{q(V_d + IR_S)}{nkT}} - 1\right) - \left(\frac{V + IR_S}{R_{sh}}\right). \tag{2.15}$$

These resistive losses can significantly affect both the *I-V* curve and the fill factor of the solar cell. The value of R_s should be kept as low as possible (ideally R_s=0) and the value of R_{sh} should be kept as high as possible (ideally R_{sh}=∞) in the design and fabrication of a solar cell.

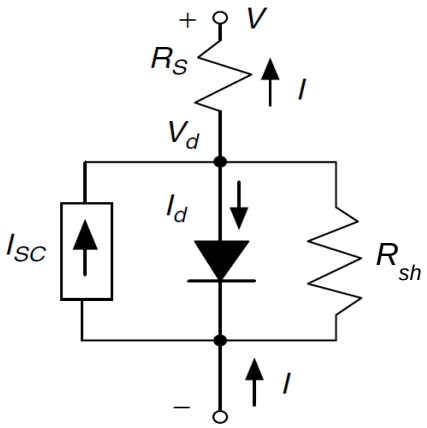

Figure 2-18: A realistic equivalent circuit model for a solar cell, which includes series and shunt losses (Taken from [13]).

2.4.4 Effect of Temperature

The temperature of the solar cell has a significant impact on V_{oc}, which implies that the efficiency of a solar cell is also affected by the cell temperature. Equation (2.10) appears to suggest that V_{oc} and the cell temperature are directly proportional; however, this is not the case because I_o is also highly temperature dependent [25]. To better understand this dependence we consider the general expression for the saturation current of a pn-junction, which is

$$J_0 = q\sqrt{\frac{D_e}{\tau_e}}\frac{n_i^2}{N_A}\left\{\frac{S_e\sqrt{\frac{\tau_e}{D_e}}\cosh\left(\frac{x_p}{\sqrt{D_e\tau_e)}}\right)+\sinh\left(\frac{x_p}{\sqrt{D_e\tau_e)}}\right)}{S_e\sqrt{\frac{\tau_e}{D_e}}\sinh\left(\frac{x_p}{\sqrt{D_e\tau_e)}}\right)+\cosh\left(\frac{x_p}{\sqrt{D_e\tau_e)}}\right)}\right\} + q\sqrt{\frac{D_h}{\tau_h}}\frac{n_i^2}{N_D}\left\{\frac{S_h\sqrt{\frac{\tau_h}{D_h}}\cosh\left(\frac{x_n}{\sqrt{D_h\tau_h)}}\right)+\sinh\left(\frac{x_n}{\sqrt{D_h\tau_h)}}\right)}{S_h\sqrt{\frac{\tau_h}{D_h}}\sinh\left(\frac{x_n}{\sqrt{D_h\tau_h)}}\right)+\cosh\left(\frac{x_n}{\sqrt{D_h\tau_h)}}\right)}\right\}, \tag{2.16}$$

where n_i is the intrinsic carrier concentration, N_D and N_A are the donor and acceptor concentrations, respectively. S_h and S_e are the surface recombination velocities in the n and p type material, respectively. x_n and x_p are the thicknesses of the n and p type layers, respectively. D_h and D_e are the diffusion constants of holes and electrons where τ_h and τ_e are the hole and electron lifetimes. For a solar cell, this expression can be simplified to [25]

$$J_0 \cong q\sqrt{\frac{D_e}{\tau_e}}\frac{n_i^2}{N_A}. \tag{2.17}$$

Herein, J_0 is strongly dependent on temperature through its proportionality to the square of the intrinsic carrier concentration by

$$n_i^2 = 4M_cM_v\left(\frac{2\pi kT}{h^2}\right)^3(m_e^*m_h^*)^{\frac{3}{2}}e^{\frac{-E_g(T)}{kT}}, \tag{2.18}$$

where h is Planck's constant, M_C and M_v are the equivalent minima in the conduction and valence bands and m_e and m_h are the effective masses of electrons holes, respectively. The bandgap, E_g, is also temperature dependent by the Varshni equation [53]. We also assume that

$$\frac{D_e}{\tau_e} \propto T^{\gamma}. \tag{2.19}$$

where γ is dependent on the diffusion and carrier lifetimes, D_e and τ_e in this instance, which have a complex dependence on temperature that is not well understood for most materials. Often, it is either neglected or used as a fitting factor when comparing experimental results [25]. Putting equations (2.17), (2.18), and (2.19) together gives the proportionality of J_o to the temperature, which is

$$J_0 \propto T^{\left(3+\frac{\gamma}{2}\right)} e^{\frac{-E_g(T)}{kT}}. \tag{2.20}$$

Therefore, substiting equation (2.20) into equation (2.10) and then differentiating with respect to temperature gives an expression for the temperature coefficient of V_{oc} as [25]

$$\frac{\partial V_{oc}}{\partial T} = -\frac{1}{T}\left(\frac{n}{q}E_g - V_{oc} + \frac{nkT}{q}\left(3+\frac{\gamma}{2}\right)\right) + \frac{nkT}{q}\frac{1}{J_{sc}}\frac{\partial J_{sc}}{\partial T} + \frac{n}{q}\frac{\partial E_g}{\partial T}. \tag{2.21}$$

The effect of cell temperature dependence on the *I-V* curve is shown in Figure 2-19. The temperature coefficient always remains a negative quantity, so V_{oc} is always decreasing with increasing temperature. Note that $\partial V_{oc}/\partial T$ decreases with increasing radiation intensity due to the presence of the $1/J_{sc}$ term, and that J_{sc} increases with temperature. However, the decrease in V_{oc} is much more significant than the increase in J_{sc} with temperature [15]. Thus, cell efficiency drops with an increase in cell temperature.

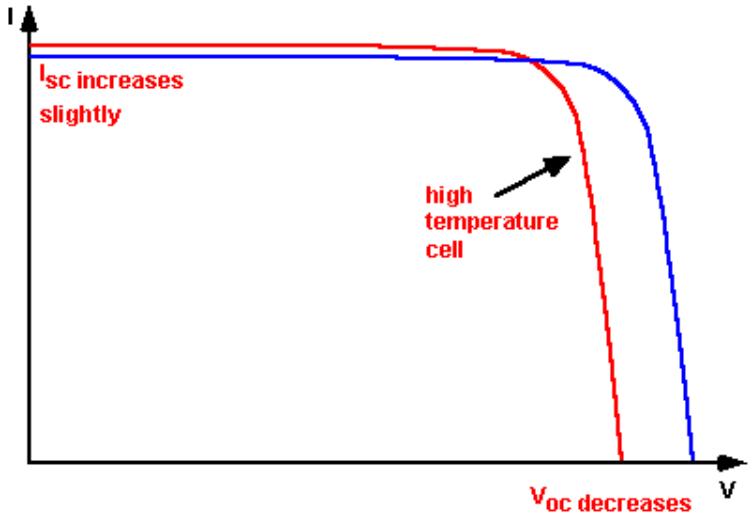

Figure 2-19: As the cell temperature increases, V_{oc} decreases and I_{sc} slightly increases (Taken from [18]).

2.4.5 Cells to Modules

An individual solar cell, with its small voltage and limited power production, is not by itself typically suited for most applications. Rather, the solar cell is the building block of a photovoltaic *module*, which is an assembly of series and/or parallel interconnected solar cells providing higher voltages and currents, as illustrated in Figure 2-20 [13, 18]. Modules can also be connected in series or parallel to produce yet higher voltages or currents if needed. Cells or modules connected in series add voltages and are limited by the lowest current producing cell or module [13, 18] as such,

$$V_{cell} = V_{top\ cell} + V_{middle\ cell} + V_{bottom\ cell}\ , \tag{2.22}$$

$$I_{cell} = \min(I_{top\ cell}, I_{middle\ cell}, I_{bottom\ cell})\ . \tag{2.23}$$

Likewise, cells connected in parallel add currents. If two modules are connected in parallel with different voltages, the module with the lower voltage will load the module with higher voltage resulting in wasted energy. If the difference is great enough the panel with lower voltage may be damaged, so this situation should be avoided. Thus, if all the cells in the module have exactly the same *I-V* characteristic and are operating at exactly the same temperature and receiving the same illumination, then from equation (2.7), the module *I-V* curve can be modelled as [18]

$$I_{module} = MI_{sc\ cell} - MI_o\left(e^{\frac{qV_{module}}{NnkT}} - 1\right), \tag{2.24}$$

where M is the number of cells connected in parallel and N is the number of cells connected in series within the module; series and shunt losses have been neglected. To demonstrate the enhancement of I_{sc} and V_{oc} when connecting cells in series and a parallel, a typical module *I-V* curve is plotted in Figure 2-20 [18].

In practice, due to manufacturing variability, cells connected together in a module almost never have precisely the same characteristics. Furthermore, differences in cell temperature and shading across the module can also result in drastic changes in the module *I-V* curve due to the differences between the individual cell *I-V* characteristics. These differences result in mismatch losses. For example, if one cell (or module) in a series-connected string is shaded, the current it produces will be much less than the more fully illuminated modules. The entire string will then output much less power since the current will be limited by the shaded cell (or module). Again, when cells or modules connected in parallel are at different voltages, current will flow from the higher voltage module into the lower voltage module, resulting in power losses. Typically, mismatch losses are responsible for less than 1% power losses in a good PV module [26]. However, such losses may increase over time as cell performance characteristics tend to degrade with age.

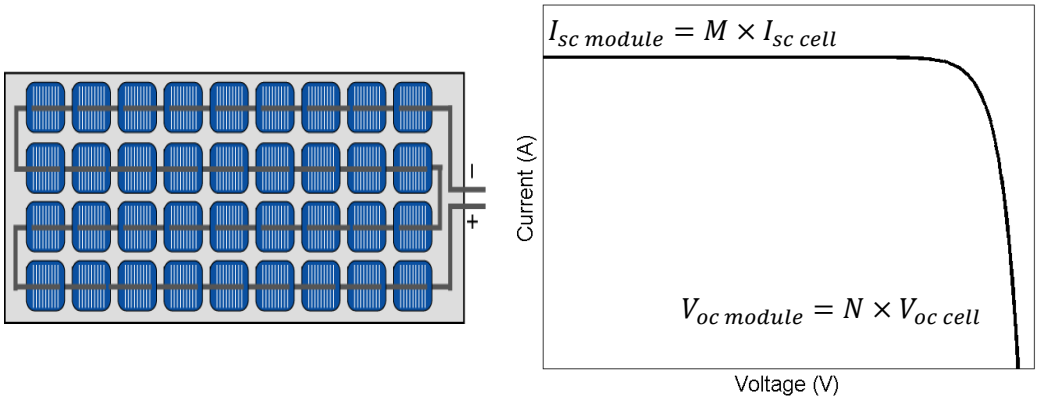

Figure 2-20: Solar module with 36 cells wired in series and the effect of connecting solar cells in series and parallel (Adapted from [18]).

2.5 Multi-Junction Cells

Efforts toward a maximally efficient solar cell have led to the development of many different solar cell designs beyond the silicon solar cell. One of the most promising technologies is the multi-junction solar cell. As noted above, photons with energy near the bandgap are most efficiently absorbed. Multi-junction cells make use of this fact by stacking several junctions (or sub-cells) of different bandgaps, thus allowing more photons to be efficiently absorbed. This occurs because each junction harvests a different portion of the solar spectrum.

A common triple-junction solar cell (3JSC) configuration is shown in Figure 2-21a. It begins with a relatively high bandgap (e.g., 1.8 eV) material as the first junction [25]. Higher energy photons are absorbed by this sub-cell. Some of the lower energy photons that pass through this top sub-cell are absorbed by the middle sub-cell (a bandgap of 1.4 eV) and still lower energy photons are partially absorbed by the bottom sub-cell (a bandgap of 0.67 eV). Tunnel junctions are placed between the sub-cells, connecting them in series to eliminate the voltage drop (or blocking diode type behavior) that arises when pn-junctions are directly connected.

An equivalent circuit model of a triple-junction cell can be constructed by series connecting the equivalent circuit model of Figure 2-18 as shown in Figure 2-21b. Since the sub-cells are series connected, the total voltage of the cell is the sum of the sub-cell voltages. Likewise, the current of the entire cell is limited by the sub-cell with the lowest current. Hence, it is important to engineer the triple-junction cell in such a way that each sub-cell produces the same current. Since sub-cell current production is spectrally dependent, this can be challenging since the solar spectrum varies over the course of the day and with changing atmospheric conditions.

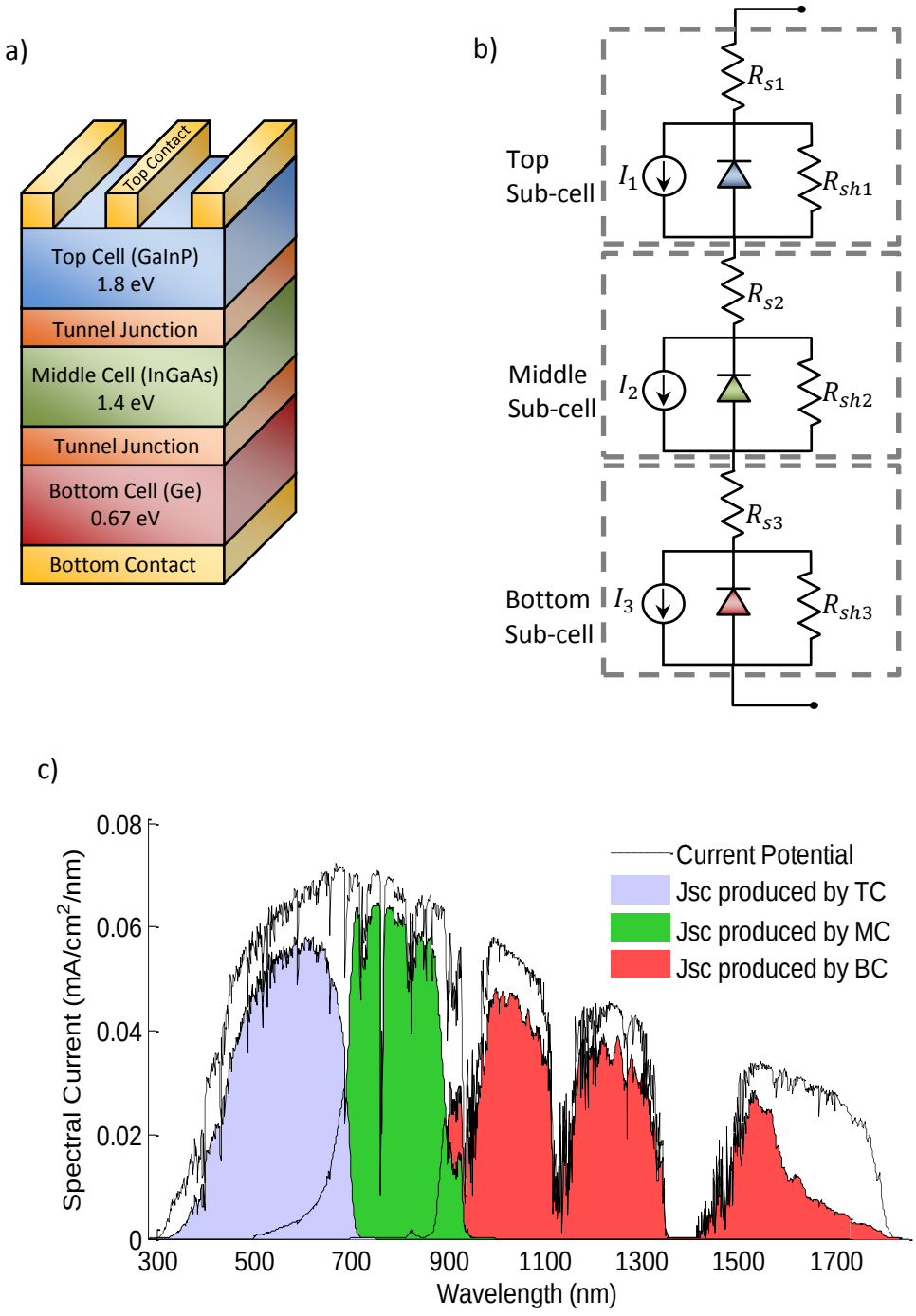

Figure 2-21: a) Simplified structure of a triple-junction solar cell. Three sub-cells, Ge, InGaAs, and GaInP are connected in series by tunnel junctions. b) Equivalent circuit model of a triple-junction solar cell. C) The absorption spectra of each sub-cell in a III-V triple junction solar cell. Each sub-cell absorbs the incident light in a specific range of wavelength (Taken from [28]).

2.6 Heat Transfer

An important aspect of CPV systems if peak cell efficiency is to be attained is the thermal management of the CPV cell. To this end, the understanding of heat transfer in a cell-on-carrier device is necessary. Some heat transfer fundamentals are presented below to support the work presented in this thesis.

The flow of thermal energy, or heat, occurs when a temperature difference ΔT exists between two systems as stipulated by the first law of thermodynamics. Heat always flows in the direction from a region of high-temperature to a region of low-temperature, and the rate of heat flow depends on the magnitude of the temperature difference between the two regions. Additionally, the rate of heat flow Q depends on the thermal resistance of the object R_{total} as

$$Q = \frac{\Delta T}{R_{total}} . \tag{2.25}$$

The thermal resistance of an object is an intrinsic physical property that governs the object's ability to resist the flow of heat. There are three mechanisms through which heat transfer can take place. These three fundamental mechanisms are: convection, thermal radiation, and conduction. The overall thermal resistance of a system or object is dictated by these three mechanisms, which independently contribute to the overall thermal resistance as

$$R_{total} = R_{cond} + R_{conv} + R_{rad} . \tag{2.26}$$

2.6.1 Convection

Convective heat transfer occurs due to the movement of fluids, which moves heat from one place to another. In many situations, convection is used to describe the heat transfer between a solid surface and an adjacent fluid that is in motion. In this way, the solid heats up the surrounding fluid through conduction and the movement of the fluid transfers the heat away from the solid. The greater the motion of the fluid the greater the convective rate of heat transfer. In this way, solids are often cooled using either passive (or natural) convection or forced convection. If the cooling requirements for the solid are stringent then forced convection can be used to enhance the cooling of the solid by forcing a fluid, such as air or water, over the solid. Otherwise, passive convection can be used to cool the solid where the movement of the fluid is due to buoyancy forces as a result of the thermally-induced density differences in the fluid. For CPV systems with concentrations under 1000 suns, passive heat sinks are sufficient to dissipate the thermal load [27].

The rate of heat transfer by convection Q_{conv} can be determined from Newton's Law of cooling, which states

$$Q_{conv} = hA(T_{surf} - T_{fluid}) , \tag{2.27}$$

where T_{surf}, is the temperature of the surface of the solid, T_{fluid} is the temperature of the surrounding fluid, A is the area of the surface in contact with the fluid, and h is the convective heat transfer coefficient. The convective heat transfer coefficient is neither a property of the fluid

nor the solid. Rather, it is dependent on all the variables that can affect convection, such as surface geometry, fluid velocity, and the thermal properties of the fluid and solid. Typically, the convective heat transfer coefficient must be determined experimentally. Moreover, comparing equation (2.27) with equation (2.25) tells us that the convective thermal resistance is given by

$$R_{conv} = \frac{1}{hA}. \tag{2.28}$$

2.6.2 Thermal Radiation

Thermal radiation is a form of electromagnetic energy emitted from matter by virtue of its temperature. The thermal motion of the particles that make up matter results in charge acceleration, which produces a spectrum of electromagnetic radiation related to the distribution of kinetic energies. This radiation can be absorbed by surrounding matter, resulting in radiative heat transfer. Since thermal radiation is by definition electromagnetic radiation, it enables heat transfer through vacuum, which is how the sun's energy reaches the earth. The heat thermally radiated from a body Q_{rad} is described by the Stefan-Boltzmann law as

$$Q_{rad} = \varepsilon\sigma A(T_{body}^4 - T_{amb}^4), \tag{2.29}$$

where σ is the Stefan-Boltzmann constant, T_{body} is the temperature of the body, T_{amb} is the temperature of the surrounding environment, and ε is the emissivity of the surface. From equation (2.29) we notice that the thermal resistance due to radiative heat flow is,

$$R_{rad} = \frac{1}{\varepsilon\sigma A}. \tag{2.30}$$

2.6.3 Conduction

Conduction, or conductive heat transfer, is the transfer of thermal energy from energetic particles to less energetic neighbouring particles via inter-particle interactions. Conduction occurs in solids, liquids, and gases. Conduction in liquids and gases are a result of the random molecular collisions within the substances, whereas conduction in solids is caused by lattice vibrations as well as the transport of free electrons. Mathematically, conduction is modelled by Fourier's Law, also known as the law of heat conduction, which gives the heat flux density in a given direction in terms of the temperature gradient in that direction as

$$\vec{q}_{cond} = -k\nabla T, \tag{2.31}$$

where k is the material's thermal conductivity.

One-dimensional conduction

To develop a conceptual understanding, consider the case where heat flows in only one direction, as shown in Figure 2-22. This situation is described by the one-dimensional form of Fourier's law, which is

$$\vec{Q}_{cond} = -kA\frac{dT}{dx}. \tag{2.32}$$

Over a known material thickness t, integration of equation (2.32) gives the one-dimensional heat flux, or rate of heat transfer by conduction, as

$$\vec{Q}_{cond} = -\frac{kA}{t}(T_1 - T_2)\,. \tag{2.33}$$

This reveals that the transfer heat in one-dimension is dependent on the thermal conductivity of the material and its thickness. Manipulating equation (2.33) allows us to easily deduce that the one-dimensional conductive thermal resistance is given by

$$R_{1D} = \frac{t}{kA}\,. \tag{2.34}$$

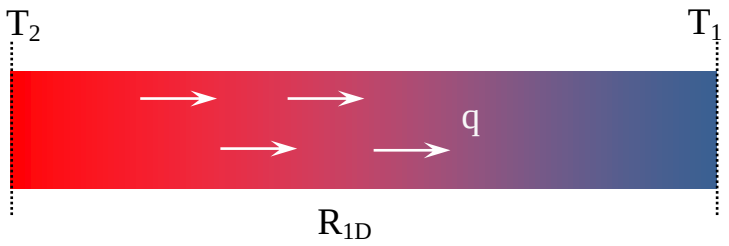

Figure 2-22: One-dimensional temperature difference created by the flow of heat or transfer of thermal energy.

Spreading Resistance

In the context of carrier design, heat spreading (also known as thermal spreading resistance) must be considered. Heat spreading occurs as heat flows conductively between a heat source (*e.g.*, a solar cell) and a region of larger cross-sectional area (*e.g.*, the carrier). This allows heat to flow in three dimensions, and the resulting lateral spreading of the heat flux lines is advantageous when moving heat from a small heat source to a larger heat sink. Consider a planar rectangular heat source on top of a larger rectangular multi-layer flux channel, or heat spreader, as shown below Figure 2-23. The heat source has length *a* and width *b*, the heat spreader has length *c* and width *d*, and the two layers of the heat spreader have thicknesses t_1 and t_2 and thermal conductivities k_1 and k_2, respectively. The cooling of he bottom surface of the spreader is described by a uniform heat transfer coefficient, *h*. This *h* value can be thought of as characterizing the heat sink's thermal performance. The remaining lateral boundaries are assumed to be adiabatic. Under these assumptions, the overall thermal resistance of the heat spreader can be found analytically [28, 29]. Assuming that the total surface area of the heat spreader is sufficiently small that the radiative thermal resistance is negligible compared to other terms, then the total thermal resistance of the spreader can be expressed as

$$R_{total} = R_{1D} + R_{spread} + R_{conv} = \left(\frac{t_1}{k_1 A} + \frac{t_2}{k_2 A}\right) + R_{spread} + \frac{1}{hA}\,. \tag{2.35}$$

The spreading resistance is determined analytically using the above boundary conditions via a Fourier series representation as,

$$R_{spread} = \frac{1}{2a^2cdk_1}\sum_{m=1}^{\infty}\frac{\sin^2(a\delta_m)}{\delta_m^3}\cdot\phi(\delta_m) + \frac{1}{2b^2cdk_1}\sum_{n=1}^{\infty}\frac{\sin^2(b\lambda_n)}{\lambda_n^3}\cdot\phi(\lambda_n) + \frac{1}{a^2b^2cdk_1}\sum_{m=1}^{\infty}\sum_{n=1}^{\infty}\frac{\sin^2(a\delta_m)\sin^2(b\lambda_n)}{\delta_m^2\lambda_n^2\beta_{m,n}}\cdot\phi(\beta_{m,n})\,; \tag{2.36}$$

the eigenvalues are

$$\delta_m = \frac{m\pi}{c}, \qquad \lambda_n = \frac{n\pi}{d}, \text{and} \quad \beta_{m,n} = \sqrt{\delta_m^2 + \lambda_m^2}\,. \tag{2.37}$$

The contributions to the spreading resistance from the different heat spreader layers are accounted for in $\phi(\zeta)$, and may be found via

$$\phi(\zeta) = \frac{\left(\alpha e^{4\zeta t_1} + e^{2\zeta t_1}\right) + \psi\left(e^{2\zeta(2t_1+t_2)} + \alpha e^{2\zeta(t_1+t_2)}\right)}{\left(\alpha e^{4\zeta t_1} - e^{2\zeta t_1}\right) + \psi\left(e^{2\zeta(2t_1+t_2)} - \alpha e^{2\zeta(t_1+t_2)}\right)}, \tag{2.38}$$

where

$$\psi = \frac{\zeta + h/k_2}{\zeta - h/k_2}, \qquad \alpha = \frac{1 - k_2/k_1}{1 + k_2/k_1}. \tag{2.39}$$

Though not immediately obvious, note that the spreading resistance decreases as the thickness of the heat spreader increases whereas the one-dimensional resistance increases as the thickness of the heat spreader increases [28, 29]. This is clearly seen in Figure 2-24 where the heat spreader has a minimum thermal resistance at a certain thickness. As the thickness of the heat spreader increases, the heat flux lines spread out, allowing a more uniform heat distribution over the base of the spreader and a greater total heat exchange rate out of the spreader. On the other hand, as the thickness of the heat spreader increases so does the temperature difference between the heat source and base of the spreader. Therefore, it is clear that an optimal heat spreader thickness exists as a result of the competing effects between the conductive thermal resistances. Furthermore, as the area ($c \times d$) of the spreader increases, the total thermal resistance of the heat spreader decreases as the exchange area between heat source and heat sink is increased, allowing a greater transfer of heat from the heat source to the heat sink. This effect is also seen Figure 2-24.

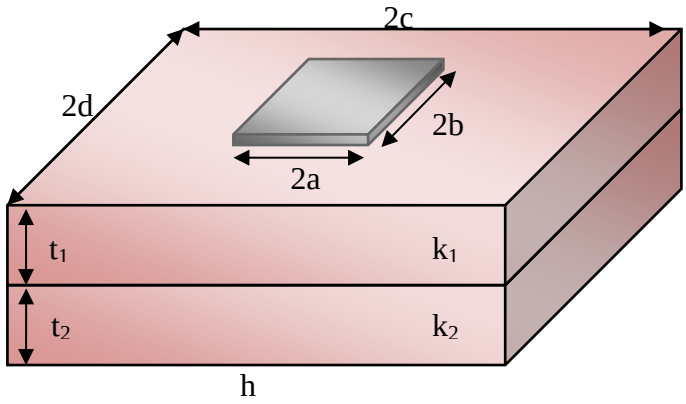

Figure 2-23: Heat source (solar cell) on a two-layer heat spreader.

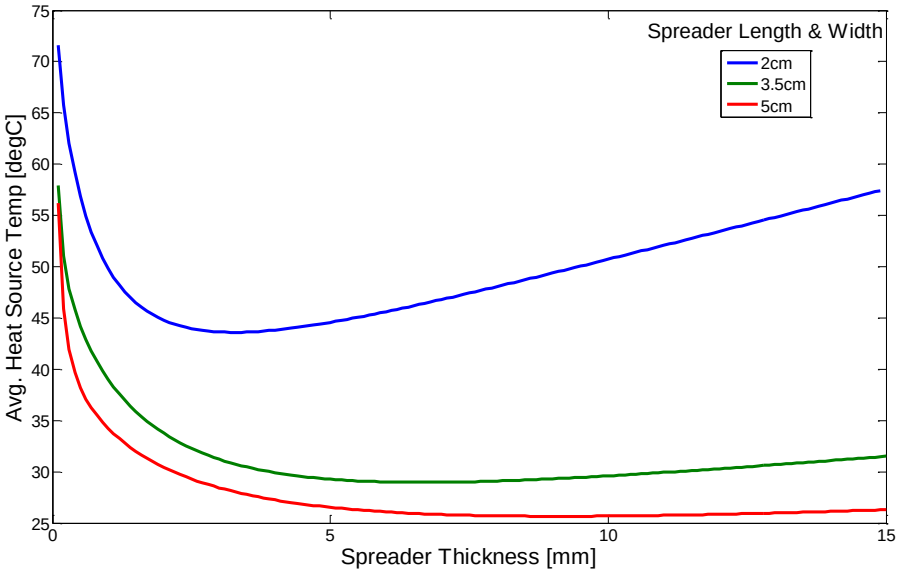

Figure 2-24: Implementation of equation (2.36). A minimum temperature exists due to the counteracting effects of the thermal spreading resistance and the one-dimensional thermal resistance.

3 Thermal Modelling of a CPV Carrier

In CPV systems, the design approach is to concentrate light onto a relatively small surface area cell so the highest efficiency solar cells are used. These are III-V multijunction cells, but while they are expensive to manufacture, the small surface area can be leveraged to build a higher efficiency system at a cost comparable to the more conventional flat panel PV technologies. In particular, cell efficiencies of slightly better than 44.4% under concentrations of 302 suns have been reported [8]. This means that, under ideal operating conditions, 60% of the incident solar radiation is still converted into thermal energy, significantly raising the cell temperature. Furthermore, as cell temperature increases, cell efficiency decreases. In particular, an increase in cell temperature reduces both the open circuit voltage of the cell by 5 mV/C° and the solar cell efficiency by 0.05 %/C° [25]. Thus, to attain maximal efficiency in photovoltaic systems it is important for the cells to operate at as low a temperature as practically possible. This is particularly important in CPV systems as the cells are subjected to intense irradiance. Sufficiently elevated temperatures not only significantly reduce cell efficiency but also rapidly lead to cell failure if the thermal management of the cell is not carefully considered.

In the interest of developing an economically viable CPV system, it is vital that a cost effective thermal management system be used. In most current CPV systems with concentrations lower than 1000 suns and cell sizes of 1 cm^2 or less, passive heat sinks, or advanced passive heat sinks in the most extreme case, are able to provide sufficient thermal sinking [27]. However, CPV passive cooling systems must primarily rely on natural convection to remove heat from the CPV modules since wind flow cannot be guaranteed. Considering the relatively intense heat-flux densities to which the cells are exposed, it is necessary to use a heat spreader to enhance the heat transfer characteristics of the passive cooling system. The geometry of the heat spreader is such that the contact area between the heat sink and heat source is enhanced, which increases the overall heat capacity of the system, allowing for a greater heat transfer. The result is a greater system cooling capacity and a lower average cell temperature. Though the carrier is primarily meant to provide the mechanical support and the electrical contacts to the cell, it also serves as a heat spreader since its geometry must have a length and width greater than the cell to provide the electrical contacts. However, the typical CPV carrier is suboptimal as a heat spreader and has inherent heat transfer limitations. Thus, optimizing the design of the carrier is conducive to achieving the maximal cell efficiency.

Both the geometry and the material properties of the carrier can significantly impact the thermal performance of the carrier and its ability to spread heat. Typically, a CPV carrier consists of a ceramic substrate, most often alumina, sandwiched between a top and bottom copper contact. The bottom of the carrier is in contact with a passively-cooled heat sink. A typical carrier design is shown below in Figure 3-1.Though various manufacturers of CPV cells usually package their cells using the same basic carrier structure, there are many variations on carrier design and few, if any, manufacturers use the exact same design. Since the geometry of the carrier, the choice of carrier materials, and the quality of the thermal contact between the

carrier and heat sink all significantly affect the thermal properties of the carrier, the thermal performance between two carrier variations is likely to be different.

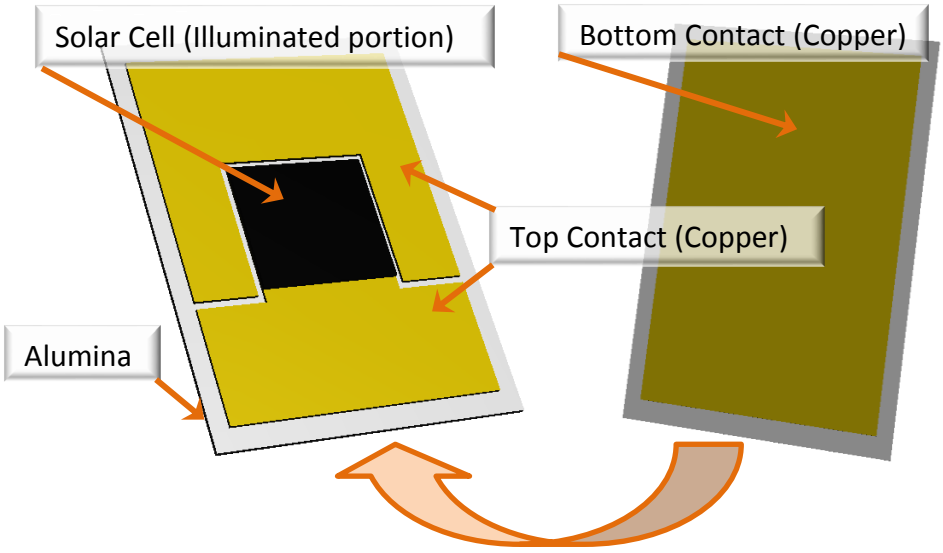

Figure 3-1: Typical cell-on-carrier geometry. The top contact, on which the cell is mounted, is divided by a channel to create the cathode and anode. The bottom contact and top contact are separated by an electrically insulating ceramic such as alumina.

In view of the complex geometry of the carrier, no analytical descriptions of the thermal behavior of the cell-on-carrier are known. Therefore, numerical methods must be used to determine the optimal or best physical configuration of the CPV carrier. In the following, the carrier‘s parameter space is explored to produce a more optimal carrier design for improved cell efficiency.

3.1 Finite Element Method Model

To explore the properties and parameter space of the carrier, an archetypal three-dimensional finite-element numerical model of the carrier was developed using COMSOL Multiphysics. The archetypal model was constructed with geometry identical to cell-on-carrier assemblies available in-house. This facilitated a means to verify the numerical model through comparison of the numerical results and the experimental data. Furthermore, only heat transfer by conduction was accounted for within the carrier. This was the suitable choice since the carrier is solid. The mathematical model governing the steady state heat transfer by conduction can be stated generally as,

$$-\nabla \cdot (k\nabla T) = Q, \tag{3.1}$$

where, k is the thermal conductivity of the medium, Q is the heat flux from a known source or sink, and T is the material temperature. Convective and radiative heat transfer was modelled along the exterior surfaces of the carrier using the generalized heat-flux boundary condition,

$$\mathbf{n} \cdot (k\nabla T) = q_o + h(T_{bulk\ amb} - T) + \varepsilon\sigma(T_{amb}^4 - T^4), \tag{3.2}$$

where **n** is the unit normal to the boundary, q_o is the heat flux density incident on the boundary, h is the convective heat transfer coefficient, $T_{bulkamb}$ is the ambient bulk temperature, T_{amb} is the temperature of the surrounding radiative environment, ε is the surface emissivity, and σ is the Stefan-Boltzmann constant.

In addition to the general shape and dimensions of the cell-on-carrier, several assumptions regarding its environment and physical properties need to be made. First, it was assumed that the MJSC was effectively composed of germanium, with an overall layer thickness of 265μm. This was a valid assumption since the InGaAs and InGaP subcells are much thinner than the germanium substrate and their effect on the thermal conductivity of the cell is minimal relative to the germanium substrate [37]. Next, the germanium, copper, and alumina components were assigned appropriate thermal conductivities, k, as given in Table 1. Furthermore, the top surface of the solar cell was assumed to be uniformly illuminated with concentrated light. Consequently, a constant heat flux, q, was applied to the top surface of the solar cell with a power density proportional to the concentration factor. The concentration factor used is specified in Table 1, assuming that one sun equals 1000 W/m^2. Therefore, the heat flux flowing into the solar cell is expressed as,

$$q = \text{Concentration} \times 1000\, W/m^2 \ . \tag{3.3}$$

The numerical model addresses only the worst case scenario where the cell is at V_{oc} and all photons are absorbed and converted into thermal energy. The results from the modelling are assumed to be taken at V_{oc} unless otherwise noted. However, when the cell is biased at its maximum power point the heat absorbed by the cell is reduced by the efficiency that the cell converts photons to electricity as

$$q_{mp} = (1 - \eta) q_{Voc}, \tag{3.4}$$

where q_{mp} is the heat absorbed by the cell at maximum power point, η is the efficiency of the cell when biased at its maximum power point, and q_{Voc} is the heat absorbed by the cell at V_{oc}, which is equal to the incident irradiance on the cell. The thermal resistance of the carrier is constant with changing concentration. Therefore, if desired we can correct the temperature to maximum power point conditions from the simulated result at V_{oc} by

$$T_{mp} = T_{V_{oc}} \cdot \frac{q_{mp}}{q_{Voc}} = T_{V_{oc}}(1 - \eta). \tag{3.5}$$

Next, natural convection was assumed for all surfaces of the cell-on-carrier (except the bottom contact). Notwithstanding a rise in air temperature due to natural convection, it was assumed that the ambient air temperature remained constant at ~25 °C. That is, $T_{bulkamb}$ of equation (3.2) was equal to 25°C. In practice, a temperature gradient exists between the object and the fluid as a result of the convective flow, which reduces the rate of heat flow away from the object. This physical action is accounted for in the h parameter at the boundary conditions. Finally, the bottom surface of the carrier was assumed to be in contact with a heat sink held at constant temperature of 18 °C. A convective heat transfer coefficient, h_{heatsink}, was chosen as an adjustable

system parameter. In reality the heat sink is a solid and would transfer heat by conductive heat transfer. The convective boundary condition is a thermal resistance, albeit in a different mathematical form than conductive thermal resistance as is seen in equation (2.35). Thus, the heat sink's thermal resistance can be equivalently accounted for in a convective boundary condition. In practice, this coefficient encompasses all of a heat sink's physical properties, including the thermal contact resistance between carrier and heat sink, and so can be deduced by comparing simulation and measurement. The archetypal numerical model was then simulated with the parameters shown in Table 3-1, using shape and dimensions identical to typical cell-on-carrier assemblies available for testing. The material properties were found in [60-62]. The length and width of the archetypal model was 3.3 cm and 2.5 cm, respectively. The material stack of the carrier as well as a typical surface temperature distribution are shown in Figure 3-2.

Parameter	Value
***k*, Alumina**	27 (W/m·K)
***k*, Copper**	400 (W/m·K)
***k*, Germanium**	60 (W/m·K)
***h*, all surfaces except bottom**	25 (W/m^{2}K)
$h_{heatsink}$	14500 (W/m^{2}K)
Concentration factor	1000x
***q*, heat flux (1000 suns)**	1 000 000 (W/m^2)
Copper length	22 (mm)
Copper width	25 (mm)
Copper thickness	0.25 (mm)
Alumina thickness	0.35 (mm)

Table 3-1: Simulation parameters.

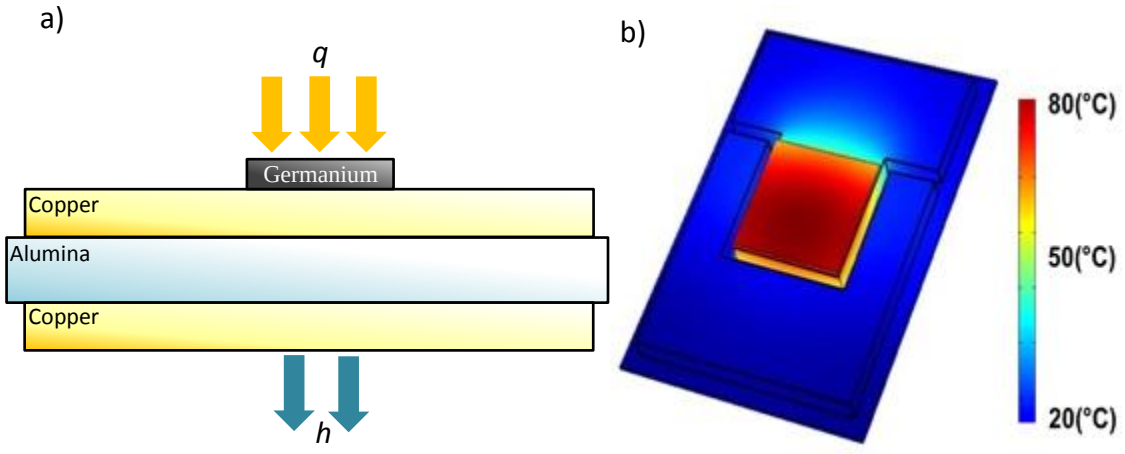

Figure 3-2: a) Material stack of the numerical model. b) Simulated surface temperature of archetypal model under 1000 suns.

3.2 Convergence Study

In numerical modelling, the solution space and the governing physical equations must be discretized so that a finite number of solution points can be computed. In finite element modelling, the solution space is discretized with a mesh. Though a rectangular mesh would be

acceptable in two or three dimensions, meshes made up of simplexes are favoured since they are much more robust as they fit best to any arbitrary object. In the present case, the mesh was made up of tetrahedra since the modelling was three dimensional. An example of a meshed cell-on-carrier is seen in Figure 3-3.

The density of the mesh affects both the precision of the solution as well as the computation resources that are required. A mesh that is too coarse will give an imprecise solution but will use limited computational resources and will compute quickly. Whereas a mesh that is too fine will have a very precise solution but may strain the computational resources. The best way to find a satisfactory balance between the solution precision and the computational resources needed is to perform a convergence test. A convergence test begins with a very coarse mesh to provide a first-order approximation to the solution. The mesh density is then successively increased until the results have converged satisfactorily. This was done with the archetypal model to determine a reasonable mesh density to be used in all subsequent simulations. The results of the convergence study are shown in Figure 3-4 for the average cell temperature as a function of the number of elements (i.e., the number of tetrahedra). Using a 0.1% precision as a required threshold, it was found that the mesh density corresponding to about 60000 mesh elements was necessary. This trade-off between precision and mesh density allowed several thousands of simulations to be calculated within a timespan of approximately two days.

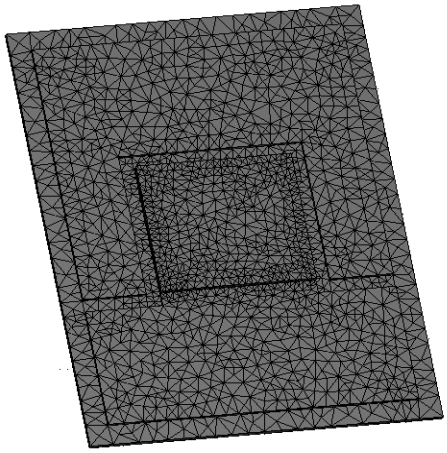

Figure 3-3: Finite element mesh of cell-on-carrier.

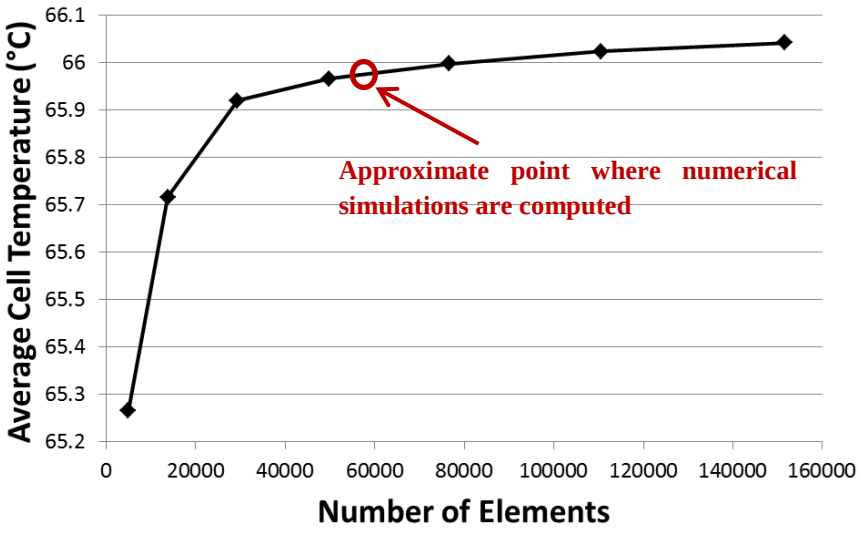

Figure 3-4: Convergence study results for archetypal cell-on-carrier and the point on the convergence curve where the numerical results were taken.

3.3 Numerical Model Calibration Summary

To verify the validity of the numerical model and to determine the experimental convective heat transfer coefficient of the carrier under test (or field) conditions, a calibration of the numerical model was done by fitting simulation results with experimental data. That is, the concentration and the convective heat transfer coefficient were varied and the average cell temperature determined in simulation. The simulations produced a set of cell temperature vs concentration curves for each value of *h*. The elements of this set were then compared with the experimentally determined average cell temperature vs concentration curve, as described below, to extract the environmentally specific convective heat transfer coefficient.

3.4 Experimental Measurements

The average cell temperature under fixed concentration was determined by observing the shift in V_{oc} due to temperature. When a solar cell is illuminated, the open circuit voltage follows the simple diode equation, which when solved for V_{oc} gives,

$$V_{oc} = \frac{k_B T}{q} \ln\left(\frac{J_{sc}}{J_0} + 1\right). \tag{3.6}$$

V_{oc} is not only logarithmically proportional to the irradiance, or concentration, but also to the temperature since the saturation current J_o depends on temperature. Under continuous high concentration, the cell temperature rises appreciably, which negatively impacts the cell efficiency. The increase in cell temperature causes a significant decrease in V_{oc} but a much less significant rise in J_{sc}. The net effect is a reduction in the maximum power available from the cell. Since the reduction in V_{oc} increases with increasing temperature, which results from increasing continuous illumination, there is a departure from the logarithmic response seen under transient temperature, where temperatures remain unchanged. V_{oc} then can used to estimate the average

cell temperature. A reference curve of V_{oc} as a function of concentration is generated for known and constant cell temperatures, which can be done with flash (transient) solar simulators. Then under continuous-wave high concentration, either with simulators or in the field, the change in V_{oc} caused only by the change in temperature can be determined by removing the change in V_{oc} due to concentration noted in the reference curve.

The reference curve of V_{oc} vs concentration, measured using a Newport Oriel flash solar simulator for low concentrations and a Sinton flash solar simulator for higher concentrations, is shown below in Figure 3-5. Measurements under the Oriel were performed in house at the SUNLab solar testing facility and performed by former graduate student Simon Chow. The Sinton measurements were done at Cyrium Technologies. The measurements under the Oriel were taken at 25 ºC under an AM1.5D spectrum. The irradiance was measured using a power meter. The temperature and spectrum during the measurements under the Sinton are not definitively known, but the results found are consistent with the Oriel data and thus these quantities have been assumed to be comparable. In all instances it was assumed that one sun is equal to 1000 W/m^2.

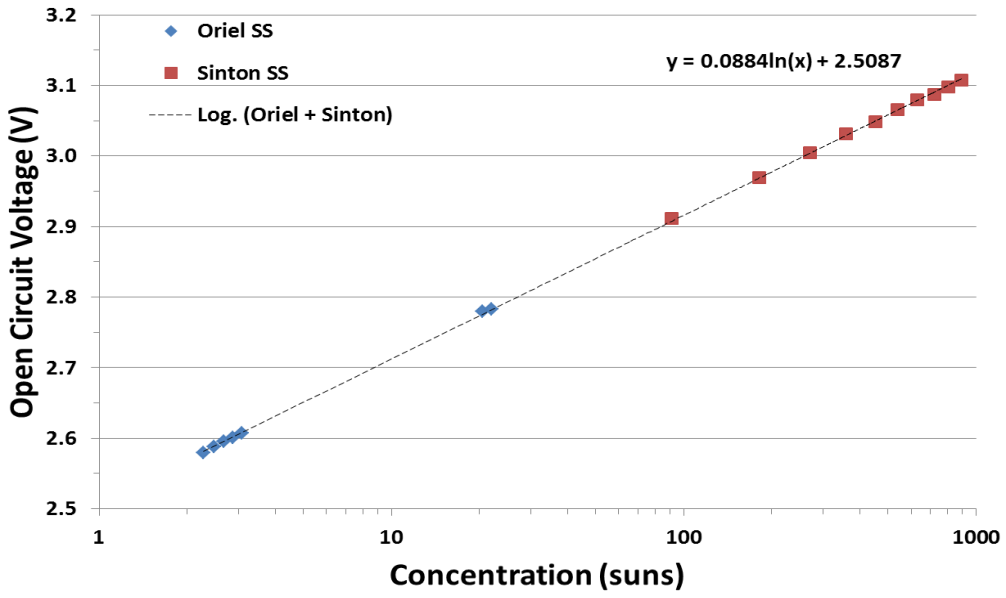

Figure 3-5: Reference curve of V_{OC} vs concentration .

I-V measurements of the cell were taken using the Spectrolab XT-30, a high concentration continuous wave solar simulator. The concentration was determined using a calibrated reference cell with a known J_{sc} vs concentration relationship. The concentration X was determined from the measured J_{sc} using the relation

$$X = \frac{Jsc(@X_{suns})}{Jsc(@1_{sun})}, \tag{3.7}$$

where it was here assumed that J_{sc} is negligibly affected by cell temperature. Shown below in Figure 3-6 are the resulting V_{oc} dependences on concentration (as a linear – log plot) for cell-on-carrier assemblies affixed to the heat sink with (crosses) and without (triangles) thermal paste. The former is similar to anticipated field conditions. Data for flash measurements (blue – Oriel, red – Sinton) are likewise plotted (square symbols) as a reference. The logarithmic dependence of this reference curve is apparent, and the departure from logarithmic behaviour under continuous wave illumination is indicative of the increasing cell temperatures. There is a greater departure when the thermal contact to the heat sink is poor, indicative of a lower heat transfer coefficient.

The increase in average cell temperature due to continuous illumination is found by comparing the flash and continuous measurements as

$$\Delta T(X) = \frac{V_{OC@25°C}(X) - V_{OC\,XT-30}(X)}{\frac{dV_{OC}}{dT}} = \frac{0.0884\ln(X) + 2.509 - V_{OC\,XT-30}(X)}{\frac{dV_{OC}}{dT}}, \qquad (3.8)$$

where $V_{OC@25°C}$ is established by the logarithmic reference and $V_{OC\,XT-30}$ by the XT-30 data. While the dV_{oc}/dT term is temperature dependent, it varies but slightly above a concentration of 200 suns. A value of -4.4 mV/C° was assumed based on results from Kinsey *et al.* [1] and Cyrium Technologies [20].

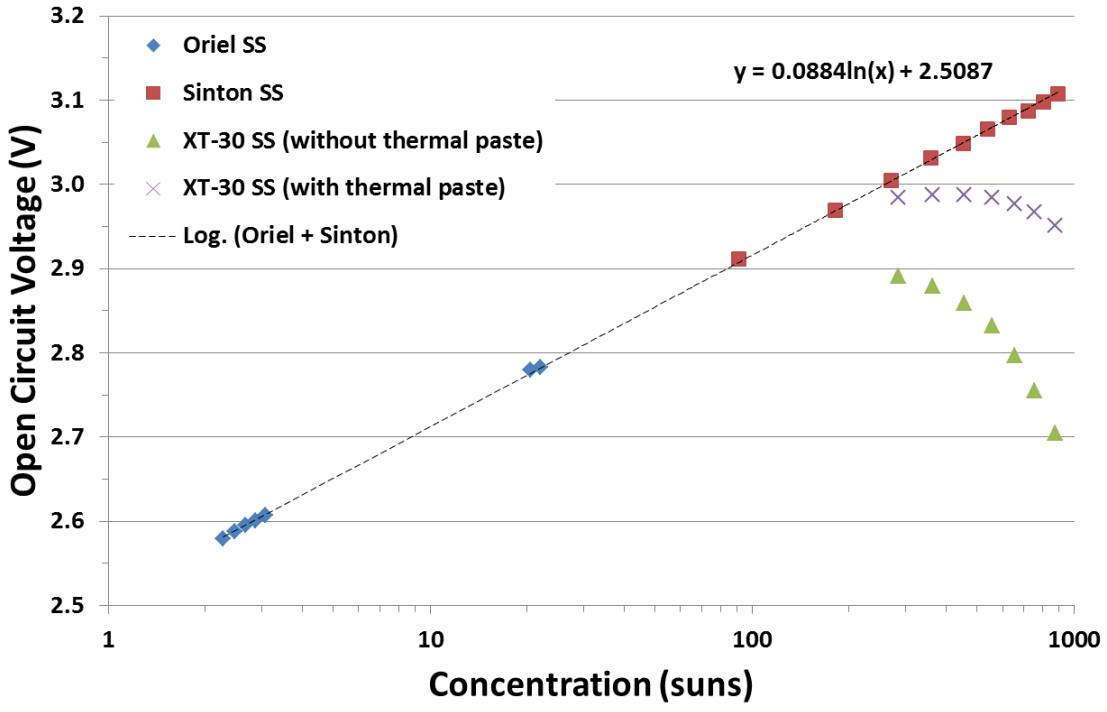

Figure 3-6: V_{OC} Measurements showing it's dependence on temperature.

With the measured cell temperature vs concentration calculated, a comparison of the simulated and measured data was done to calibrate the numerical model to the test conditions.

Plots of the simulated and measured average cell temperature vs concentration are shown below in Figure 3-7. The simulated data was selected such that the slopes of the best fit lines of the measured and simulated data were equal as the slope is proportional to the heat transfer coefficient. The vertical intercepts of the simulated curves are self-consistent with the simulation reference temperature of 18 °C. However, the vertical intercepts of the measured data are not found to agree with the 25 °C temperature of the reference cell under flash testing. This may be partially caused by an overestimation of the concentration since the effects of temperature on J_{sc} were not accounted for when determining XT-30 concentration. Cyrium Technologies quotes a J_{sc} temperature coefficient of 10.5 mA/C° at a concentration of 500 suns [20], but has a slight temperature dependence. Further, equipment measurement accuracy and environmental control in the lab also contributed minor errors to the results.

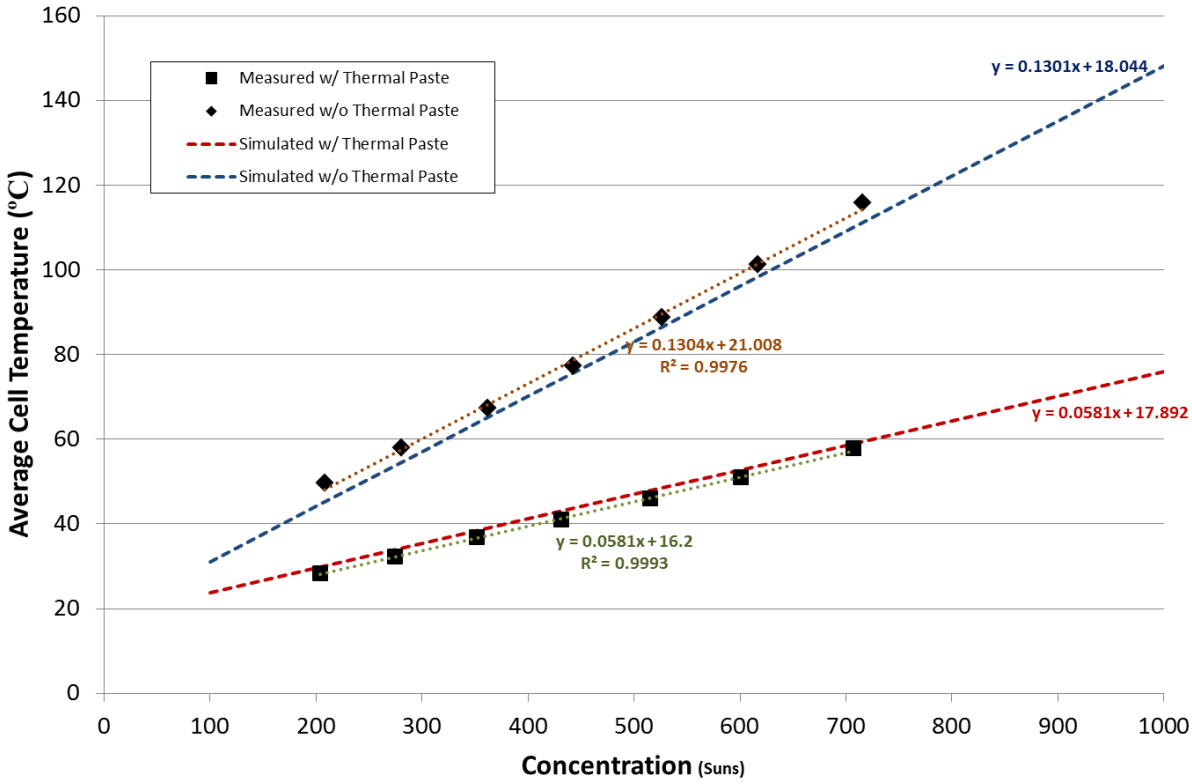

Figure 3-7: Measured average cell temperature compared with the numerical modelling results.

3.5 Results

With a calibrated thermal model developed the parameter space was explored to ascertain the optimal carrier configuration.

3.5.1 Optimal Thickness

Copper and Alumina Thickness Study

The carrier should have an optimal thickness that minimizes the total thermal resistance of the carrier. Since the carrier is made up of three layers, the effect of varying the thickness of each layer was explored. The thicknesses of the copper layers were assumed to be the same and were varied independently of the alumina thickness. In practice, having an equal amount of copper on both sides of the layer of alumina would help to balance the mechanical stresses, particularly when the carrier undergoes rapid temperature changes driving thermal expansion or contraction. The simulations were conducted by varying the thicknesses of the copper and alumina of the archetypal numerical model. The results are shown below in Figure 3-8.

Increasing the thickness of the alumina acts only to increase the thermal resistance of the carrier, which is reflected in the increasing average cell temperature with alumina thickness in Figure 3-8. Consequently, removing the layer of alumina completely would result in the lowest average cell temperature; however, the alumina serves several purposes, as noted below, and thus cannot be removed. For fixed alumina thickness, there is an optimum copper thickness that minimizes the thermal resistance of the carrier. This is reflected in the minimum that exists as a function copper thickness as seen in Figure 3-8.

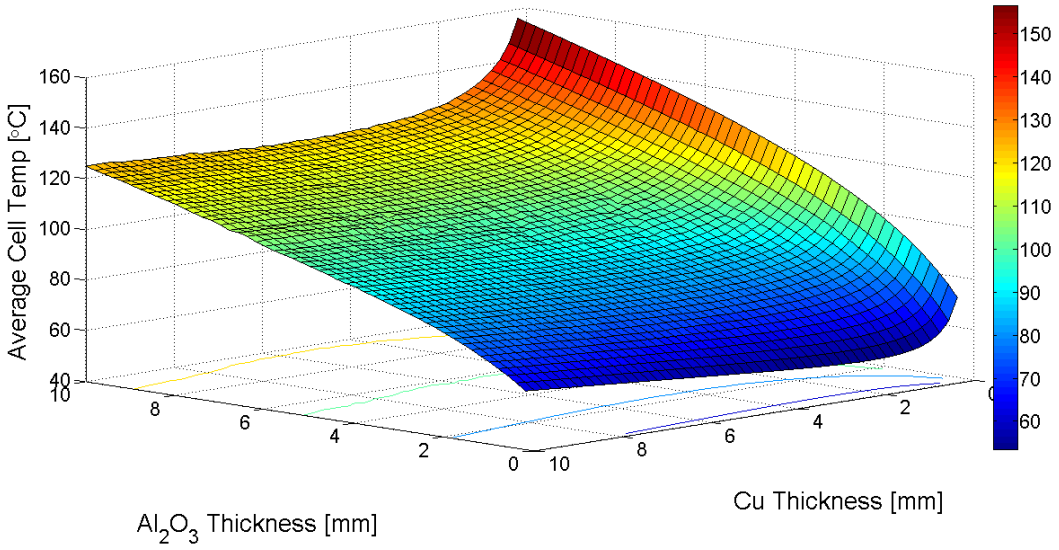

Figure 3-8: Results of varying the alumina and copper thicknesses. Decreasing the thickness of the alumina results in better thermal performance of the carrier.

3.5.2 Copper Thickness and Side Length Study

The effect of varying the length and width of the carrier against the copper thickness was also studied. For the sake of simplicity, it was assumed that the carrier had equal length and width, and the copper thicknesses were assumed to be equal. The results are shown below in Figure 3-9. An optimal copper thickness exists that minimizes the average cell temperature, for any given carrier side length. Furthermore, the greater the side length, for fixed copper thickness, the lower

the average cell temperature. The thermal spreading resistance largely dominates the overall thermal resistance at copper thicknesses less than about 1.5 mm. That is, as the copper layer becomes sufficiently thin, the heat does not spread away from the solar cell as easily resulting in a rise in average cell temperature. There is also a rise in average cell temperature as the copper thickness is increased beyond 3 mm, where the one-dimensional thermal resistance dominates the overall thermal resistance.

The average cell temperature of the archetypal model (3.3 cm by 2.5 cm) was also compared with the average cell temperature of a square carrier with optimal copper thickness and equal footprint (8.25 cm^2). In this case the optimal copper thickness of the square carrier was 2.5 mm with side lengths of 2.87 cm. Moreover, it was found that the archetypal model had an average cell temperature of approximately 66 °C whereas the optimized square carrier had an average cell temperature of 50 °C, an average cell temperature reduction of 16 C° at V_{oc}. Assuming a cell efficiency of 40% (η=0.4), the equivalent performance when biased at V_{mp} (the maximum power point) can be calculated with equations (3.4) and (3.5). Then at V_{mp} an average cell temperature reduction of 9.6 C° was found, which lead to an increase in cell efficiency of about 0.5% under 1000 suns. Moreover, the optimum copper thickness of the archetypal model was found to be 2.4 mm resulting in an average cell temperature of 57.2 °C leading to an improvement of cell temperature of 8.8 C° at V_{oc}. At V_{mp} this temperature reduction would be 5.3 C° corresponding to an improvement in efficiency of approximately 0.26% at 1000 suns when optimizing the copper thickness only. Not included in the modelling are the electrical leads or wires that are bonded to the carrier as well as the bypass diodes. These components dissipate their heat through convection, which represents a fairly significant thermal resistance and minimal heat loss. Thus, the effect of these components on the results is negligible.

It is important to note that CPV carriers are direct bonded copper substrates, made by bonding copper sheets to either side of the ceramic through a high temperature-oxidation process. The ceramic in this case is alumina. Typically, the copper thicknesses of direct bonded copper substrates are in the ranges of tens to hundreds of microns, which is an order of magnitude less than the optimal copper thicknesses [16]. Therefore, to achieve the optimal thicknesses the direct bonding process would need to change or an alternative method would need to be used to construct the carrier.

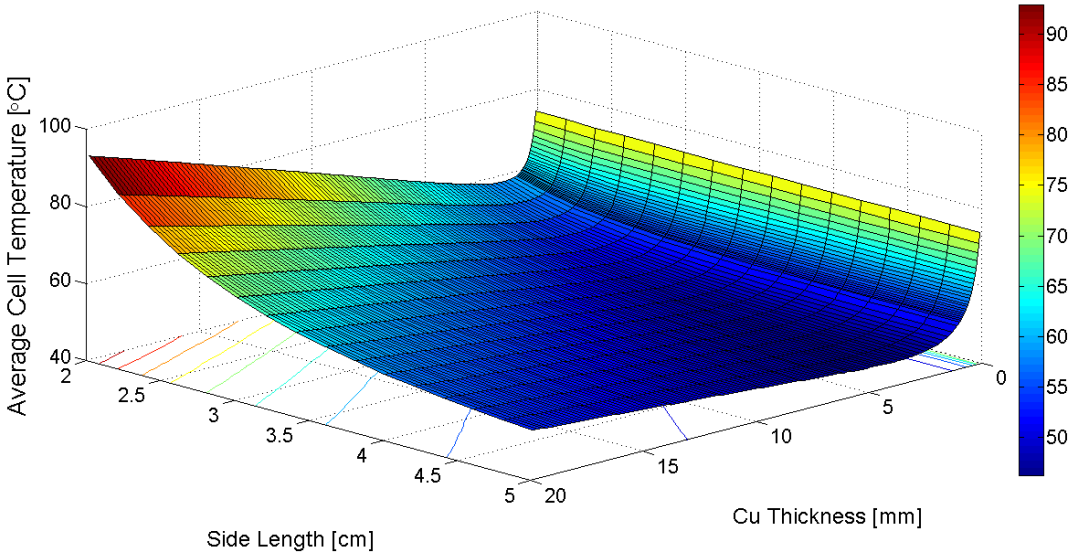

Figure 3-9: Results of varying carrier side length and copper thicknesses. An optimal copper thickness clearly exists due to the competing effects of the thermal spreading resistance and the one-dimensional thermal resistance. Increasing the side length of the carrier improves its thermal performance but with diminishing gains as the side length is increased.

3.5.3 Ceramic Substrate

The purpose of the carrier's ceramic substrate is to electrically isolate the carrier from the surrounding environment while providing mechanical support under varying temperatures for many years. This requires a material that is electrically resistive and thermally conductive, yet mechanically strong and stable. Ceramics are the only materials that are able to provide all of these properties and there are a limited number. These ceramics are alumina (Al_2O_3), boron nitride (BN), silicon nitride (Si_3N_4), aluminum nitride (AlN), and beryllium oxide (BeO) [32]. In determining the thermally optimal carrier, the principal focus is the thermal conductivity of the ceramic substrate. However, the optimal design goes beyond the thermal, and parameters such as cost, the coefficient of thermal expansion (CTE), and mechanical strength must all be considered. With all this in mind, the archetypal model was solved with a range of thermal conductivities for the ceramic substrate to evaluate the efficiency gains. The copper thicknesses were also varied to ensure that the maximal cell efficiency could be obtained for the carrier geometry at each choice of thermal conductivity. The results are plotted below in Figure 3-10, specifics of which are discussed below. The thermal conductivities for each of the ceramic substrate candidates are given in Table 3-2.

Alumina

Alumina is the ceramic substrate preferred by industry since it has the necessary electrical, thermal, and mechanical properties at a competitive cost [32]. It is also favourable as a CPV carrier as its coefficient of thermal expansion is similar to germanium, which reduces stress on the cell when temperature changes occur. It is for these reasons that alumina carriers were available in-house and that the archetypal model was constructed with alumina. Since alumina is

the substrate used in the archetype model the results are those stated above. To restate, a thermal conductivity of 27 W/(m·K) at 25 °C gives an average cell temperature of 57.2 C° at V_{oc} with an optimum copper thicknesses of 2.4 mm.

Silicon Nitride

Silicon nitride has a similar thermal conductivity to alumina and the thermal performance is expected to be nearly identical to alumina near room temperature. However, silicon nitride may be an attractive substitute for alumina as it is a much stronger material than any of the other ceramics. This may make it the more mechanically reliable given the thermomechanical aging the carrier tends to experience [32].

Boron Nitride

Boron nitride has a thermal conductivity slightly higher than alumina. Assuming a boron nitride substrate with a thermal conductivity of 40 W/(m·K) at 25 °C [32], then the optimal copper thickness would be approximately 2.2 mm. This would result in an average cell temperature of 54.0 °C at V_{oc}, an absolute increase in efficiency of 0.1% at V_{mp} when compared with alumina.

Aluminum Nitride

Aluminum nitride is a much more thermally conductive ceramic than alumina, in the range from 80 W/m/K to 200 W/(m·K), depending on the manufacturing processes used. Assuming a thermal conductivity of 170 W/(m·K) at 25 °C, a value quoted by some manufactures [32], the optimal copper thicknesses were found to be about 1.8 mm. This produced an average cell temperature of 49.3 °C at V_{oc}, an absolute increase in efficiency of 0.24 % at V_{mp} when compared with alumina. Furthermore, the mechanical properties of aluminum nitride are similar to alumina, which would make it a thermally superior substitute to alumina. However, aluminum nitride, despite being competitively priced, is still slightly more expensive than alumina, which is what limits its attractiveness.

Beryllium Oxide

Of all the electrically insulating materials, beryllium oxide has the highest thermal conductivity, second only to diamond. With 300 W/(m·K) at 25 °C ambient, it was found that optimal copper thicknesses of approximately 1.8 mm resulted in an average cell temperature of 48.4 °C at V_{oc}. This represents a 0.27 % increase in efficiency compared to the carrier with alumina at V_{mp}, and slightly thermally superior to aluminum nitride. While beryllium oxide has mechanical properties similar to that of alumina and aluminum nitride, it is toxic to humans and is a known carcinogen. It is avoided in most applications including CPV.

Material	Thermal Conductivity (W/mK)
Alumina (Al_2O_3)	27
Silicon Nitride (Si_3N_4)	20-30
Boron Nitride (BN)	27-70
Aluminum Nitride (AlN)	80-200
Beryllium Oxide (BeO)	200-300

Table 3-2: Ceramic thermal conductivities.

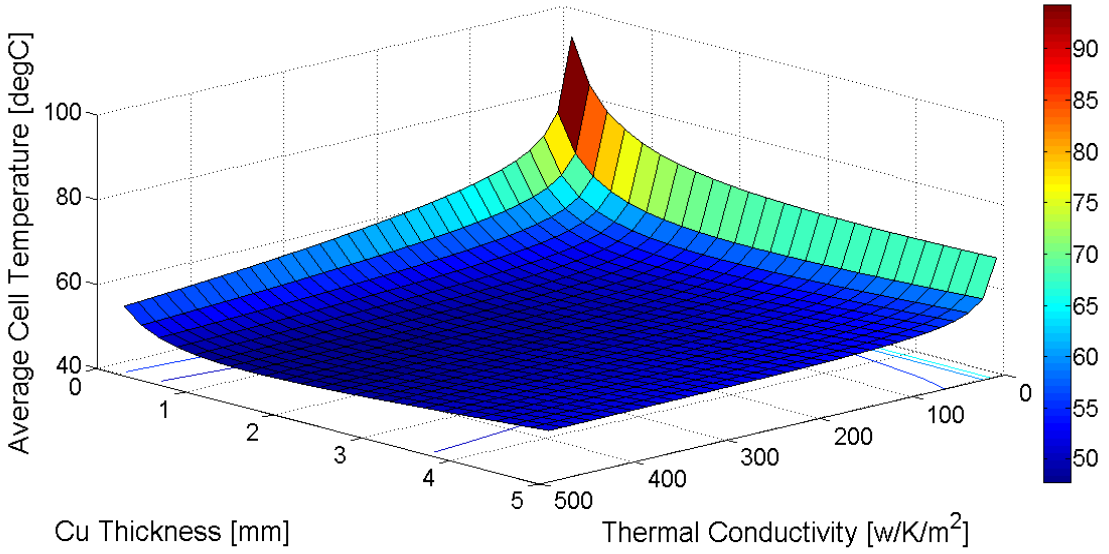

Figure 3-10: Varying thermal conductivity of ceramic substrate. The thermal performance of the carrier can be improved by using ceramics with good thermal characteristics. Only modest gains in the carrier's thermal performance are realized when compared with the alumina carrier.

3.5.4 Channel Configuration

The carrier's material properties and geometry have been seen to all play a role in the carrier's ability to dissipate heat. Specifically, appropriate choice of layer thickness and lateral carrier area can appreciably reduce the thermal spreading resistance of the carrier. However, the channel layouts on the top layer of the carrier also impact heat spreading. The channels serve to electrically partition the top layer of the carrier to allow for a practical contact to the cathode and anode of the cell. In doing so, the channels also limit the spreading of heat flux lines in the top layer of the carrier, which limits the heat exchange between the carrier and heat sink and effectively increases the thermal resistance of the carrier. Therefore, channel configuration also requires optimization. Figure 3-11 presents the channel layout variants that were studied, overlaid with the top layer temperature determined via numerical simulation. The parameters used for all layouts were those of the archetypal model (of which the tophat channel layout is itself part), given in Table 3-1. The average cell temperatures that were determined are shown in Figure 3-12. Single U and straight line channels yield cell temperatures some 4 C° lower than the tophat and L channel configurations, with the double U variant somewhere in the middle. Clearly, layouts that maximize the contiguity of the top layer with the cell are optimal for heat

transfer. However, there are other technical requirements that must be considered in choosing the appropriate layout.

The L-channel layout and the tophat channel layouts provided the highest average cell temperatures but both are commonly used since they allow for wire bonding to the anode carrier contact on two sides of the cell. Despite limiting the heat spreading the L-channel configuration is favoured by many vendors such as Suncore or Spectrolab [30,31] since it allows for the mounting of a bypass diode while minimizing the carrier area, which translates to minimizing cost. However, the tophat channel shape would still allow for ample room to mount the bypass diode with sufficiently large side lengths. However, this requires a larger carrier, which implies higher material costs.

The double-U channel layout allowed for slightly lower average cell temperature than the L-channel or tophat channel layouts since it facilitated more heat spreading in the top layer of the carrier. An increase in efficiency of approximately 0.05% at V_{mp} under 1000 suns can be achieved compared to the archetypal model. Also, with the cell operating temperature 1 C° lower on average than the archetype at V_{oc}, reliability and performance would be improved over the lifetime of the cell. The double-U channel also allows for wire bonding to partitions in the top layer of the carrier from two sides of the cell. However, these two partitions that form the anode contact are physically separated and need to be electrically connected externally from the carrier to form a single anode contact and to keep series resistances minimized. For example, in a CPV module a metallic post can be mounted adjacent to the carrier where the wiring from the carrier anode can be connected to form a single connection point. This single connection point can then be used when stringing cells in series. Though the double-U channel provides improved thermal performance, the added wiring complexity is likely to hinder its desirability since more time and wiring will be required in the construction of a module. Moreover, the added wiring also potentially introduces one more thing that can go wrong, possibly counteracting any reliability benefits gained from operating at a slightly lower average cell temperature.

The straight channel and single U channel layout achieved the lowest cell temperatures, with significant efficiency increases of approximately 0.12% at V_{mp} compared to the archetypal (tophat channel) layout. Operating about 4 C° cooler at V_{oc} can also significantly reduce reliability issues. However, both of these layouts only allow wire bonding on one side of the cell, increasing series resistance losses and potentially nullifying any thermal gains in efficiency. That is, the farther the electrons have to travel through the cell to get to the anode carrier contact the greater the resistive losses.

Numerical simulations have shown that the channel layouts on the carrier have a significant impact on the thermal performance of the cell-on-carrier. However, improving the thermal performance by thermally optimizing the channel layouts generally means that simplicity of design and construction is sacrificed, which may hinder their desirability and

practicality. If these challenges can be overcome then these carrier designs are likely to be worth implementing and additional layouts explored further.

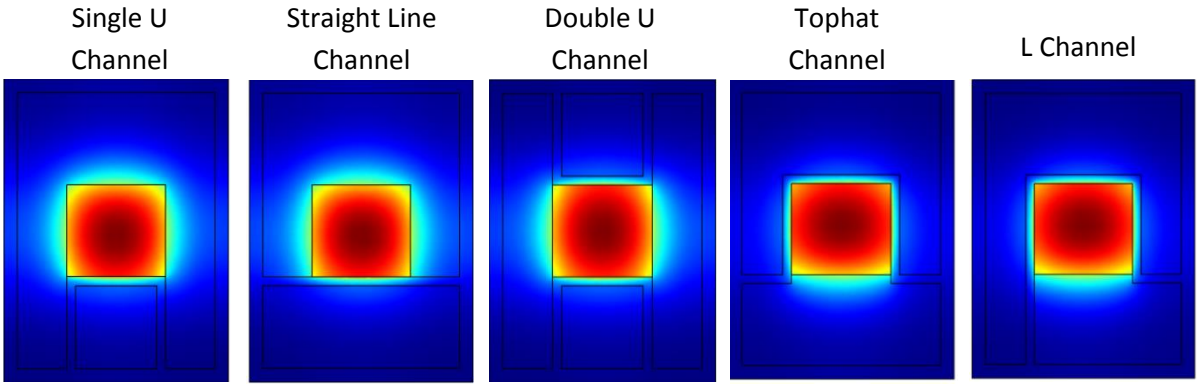

Figure 3-11: Alternative channel layouts.

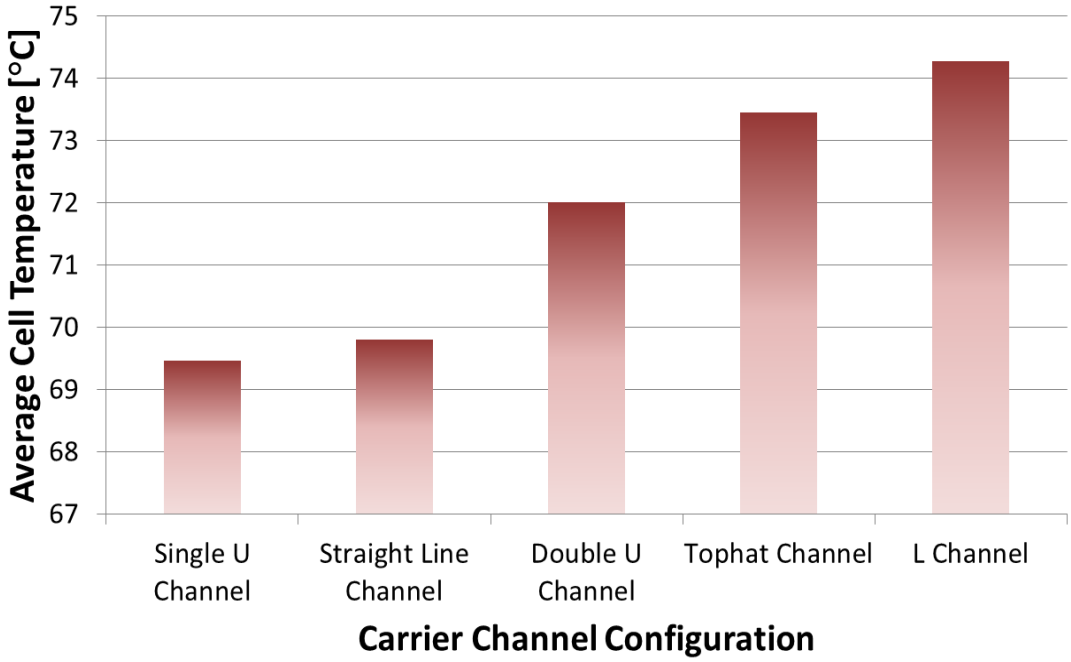

Figure 3-12: Effect of carrier channel configurations on average cell temperature at $V_{oc.}$ Alternate channel configurations can enhance the thermal spreading and improve the performance of the carrier.

3.5.5 Heat Sink Coefficient

One of the challenges faced when designing a suitable thermal management system for CPV is the choice of appropriate heat sink. Since both the thermal resistances of the cell-on-carrier assembly and its cooling requirements are generally known, the question that must be addressed is how best to dissipate the known heat production. However, heat sink designs are extensive, affected by the nature of the operating environment, and constrained by other concerns such as cost. The current perspective within the CPV industry is that passive heat sink designs are sufficient for systems operating under 1000 suns or less for cell sizes of 1 cm^2 or less [27].

Numerical simulation has been addressed in terms of an effective convective heat transfer coefficient to enable the appropriate choice of passive heat sink. Though the convective heat transfer coefficient depends on the heat sink and the environment, values for the convective coefficient can range from 50 W/(m^{2}K) to in excess of 5000 W/(m^{2}K) [33,34]. A numerical study with the archetypal model was carried out to ascertain the average cell temperature within this range of effective thermal convection coefficients. Again, the copper thicknesses were varied as well to be sure that the minimum cell operating temperature was being obtained. The results are plotted below in Figure 3-13 where an average cell temperature of 74.3 °C is observed at V_{oc} when the copper thickness is optimized at 2.4 mm for a cooling power of 5000 W/(m^{2}K). This represents a very good and likely a realistic passive heat sink. Values any higher than this are likely in the active heat sink domain. Decreasing the copper thickness to 200 μm for a convective heat transfer coefficient of 5000 W/(m^{2}K) yields an average cell temperature of 104.35 °C. This is a high cell temperature and is about the limit the cell should reach as reliability issues arise at temperatures of 100 °C and higher. Likewise, an average cell temperature of 158.8 °C at V_{oc} or 103 °C at V_{mp} is observed when the copper thickness is optimized at 4 mm for a cooling power of 1100 W/(m^{2}K). This represents a realistic value for a heat sink but it is clear it would not be adequate under 1000 suns of concentration as most vendors recommend an operating temperature less than 100 °C [31].

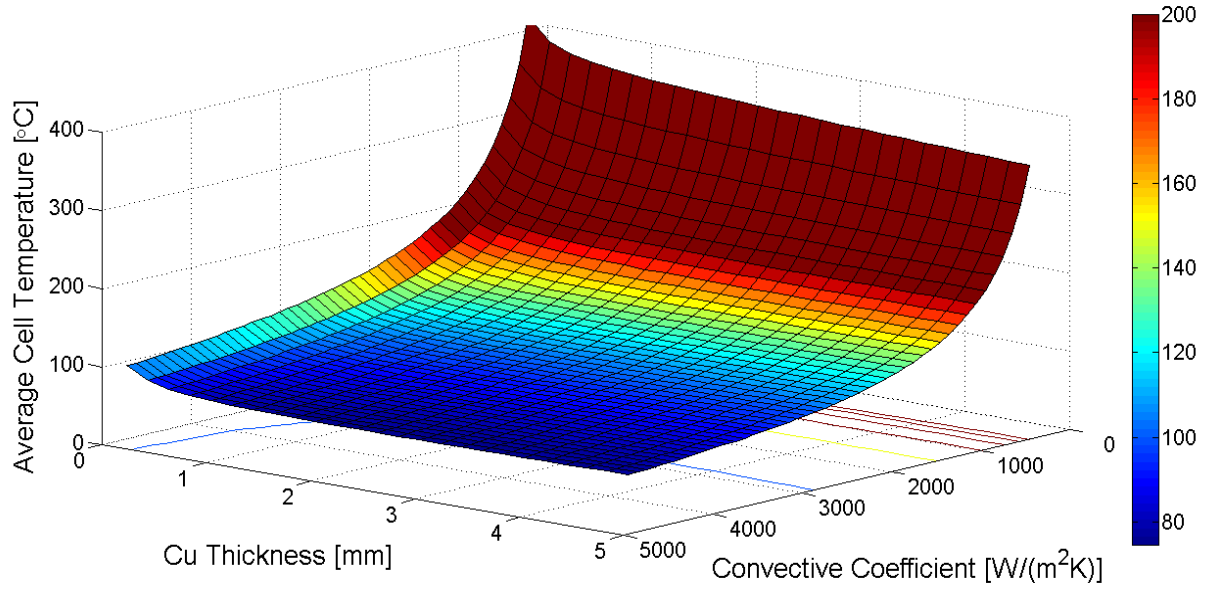

Figure 3-13: Simulation results with thermal convection varied from 500 W/(m^{2}K) to 5000 W/(m^{2}K).

3.5.6 Voids

Cells are bonded to their carriers with either a solder layer or a conductive epoxy layer. During manufacturing, voids may form in these bonding layers. The degree to which voids affect the heat transfer depends on void dimension. As both heat and electrical current must flow around these voids, the current density is locally increased, causing these regions of the cell to heat up

slightly due to Joule heating. In addition, if the heat transfer through the bonding layer is sufficiently degraded locally, then under concentrated light the cell temperature will increase in the regions directly above the voids. Both the increased current density and the increased thermal resistance contribute to the creation of a hot spot above a void. The short-term and long-term reliability of the cell depends on the temperature of these hot spots. If the voids' effect on the current crowding and the thermal resistance of the solder layer is minimal, then the hot spot temperature increase will be small, although there may still be degradation in performance and reliability over a long period of time. If voids do produce intense hot spots in the cell, these will result in large temperature gradients that can stress the cell and create fractures or contact de-lamination. More significantly, if these spots are hot enough, thermal runaway may be induced, further exacerbating cell failure modes.

To assess the direct impact of voids, they were incorporated into the thermal model to ascertain their effect on cell temperature. The results of the simulations are shown in Figure 3-14 to Figure 3-17, where the temperature scale has been fixed to aid direct comparison. These figures show plots of cell surface temperature for a single hemispherical void placed at a depth of 30 μm in the center of a 50 μm thick solder layer. Figure 3-18 summarizes the results as maximum cell (hot spot) temperature vs void diameter, with datasets for 20 μm and 50 μm depths included to demonstrate the relative insensitivity on depth, except for the widest of voids. From these results we deduce that a 25% area void (Figure 3-16) is enough to melt the indium solder that is sometimes used to bond the cell to the carrier as the cell reaches a temperature above 150 °C. This could possibly lead to cell failure if the solder were to move around and create larger voids. However, it has been found that a ~4% area void at the edge of the cell is sufficient to lead to thermal runaway [35], which is a common failure mechanism Given the generic temperature distribution across the cell surface, the local cell temperature above a corner void will be about 20% less than its temperature at the center of the cell [36]. This means that a 25% area void at the center of the cell will have approximately the same effect as a 20% area void at the corner of the cell, if only thermal effects are considered. Thus, there is a discrepancy between thermal modelling predicting potential failure at 25% and failures observed in practice caused by a 4% void. Therefore, the thermal model must be extended to include the effects of current crowding and mechanical strain if the failure mechanisms in the cell are to be fully appreciated and accurately quantified. That is, the cell failure mechanisms are a multiphysics problem requiring the physics of heat transfer, electromagnetics, joule heating, and mechanical deformation to be modelled accurately and make meaningful conclusions.

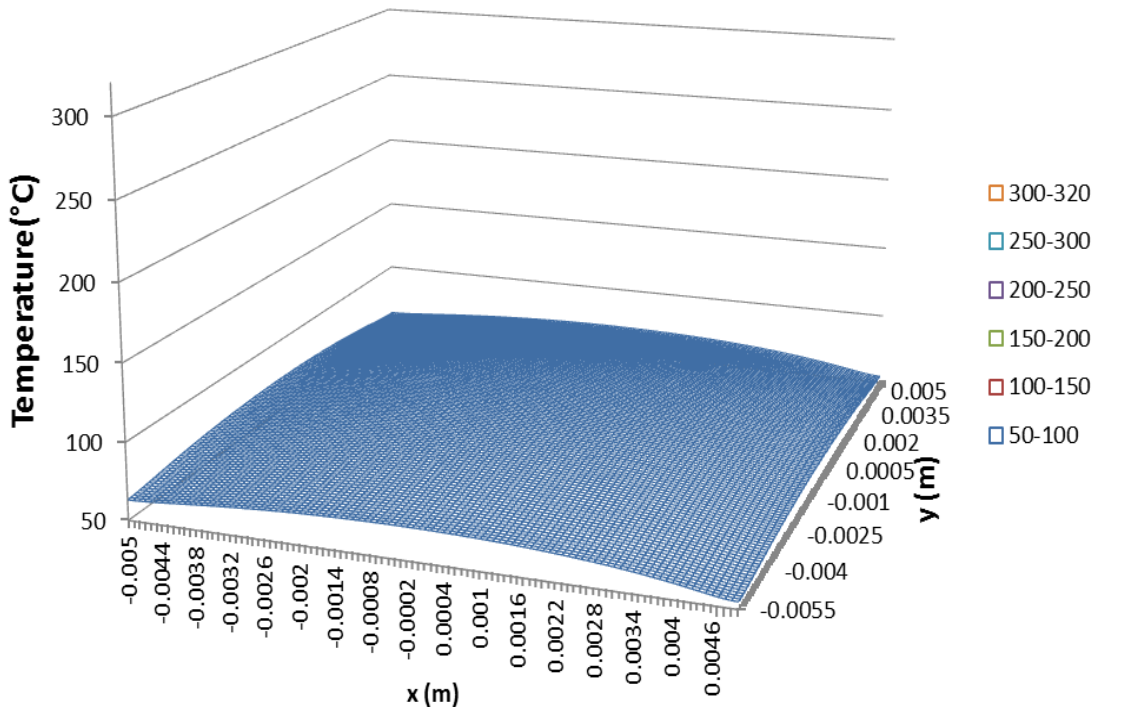

Figure 3-14: Void diameter = 0.02mm (replaces 4% of the solder volume).

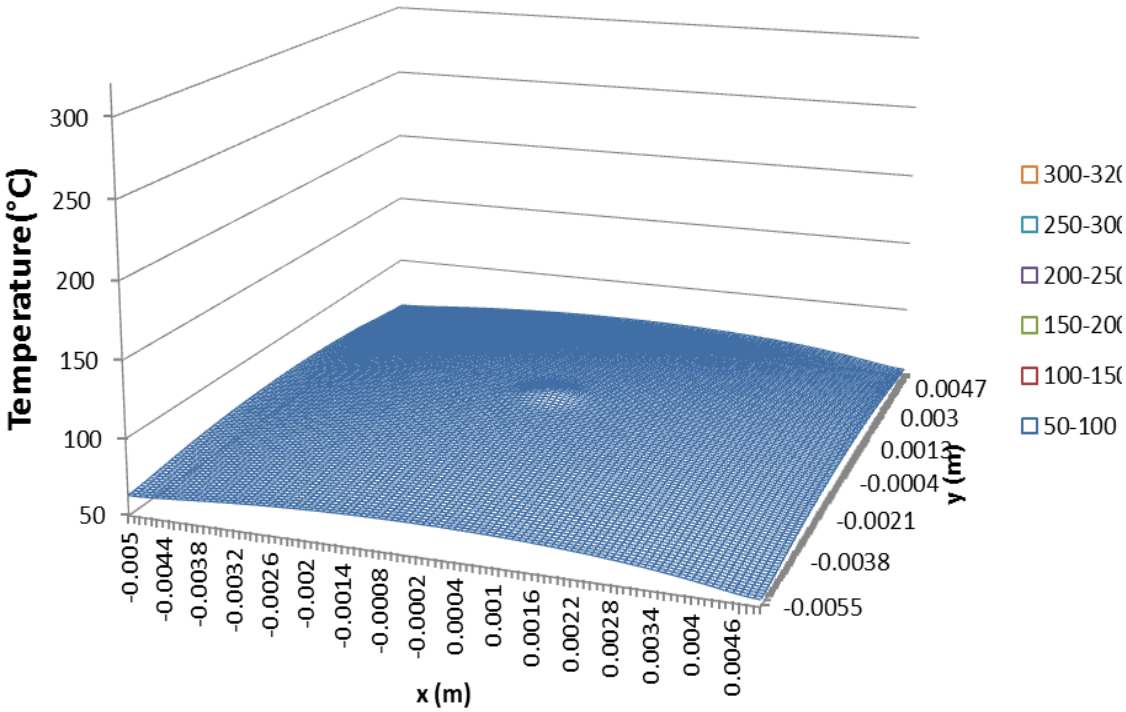

Figure 3-15: Void diameter = 1mm (replaces 10% of the solder volume).

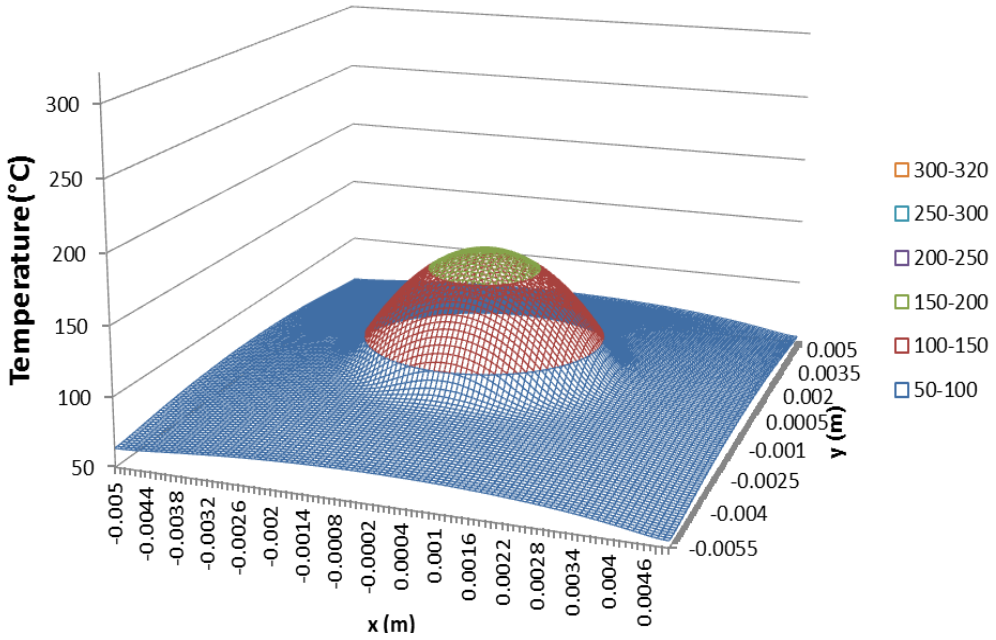

Figure 3-16: Void diameter = 5mm (replaces 25% of the solder volume).

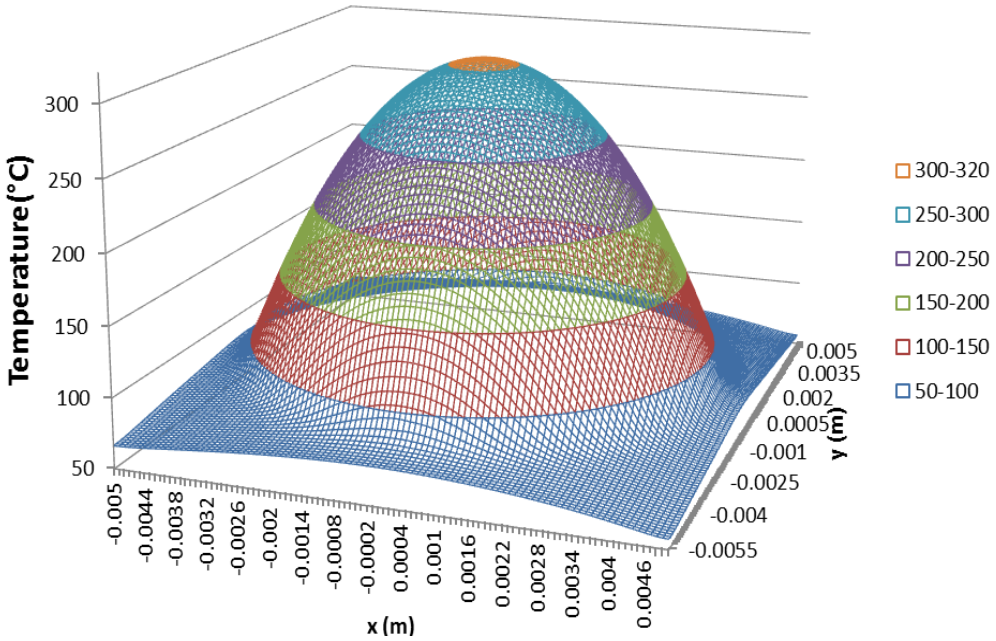

Figure 3-17: Void diameter = 9mm (replaces 81% of the solder volume).

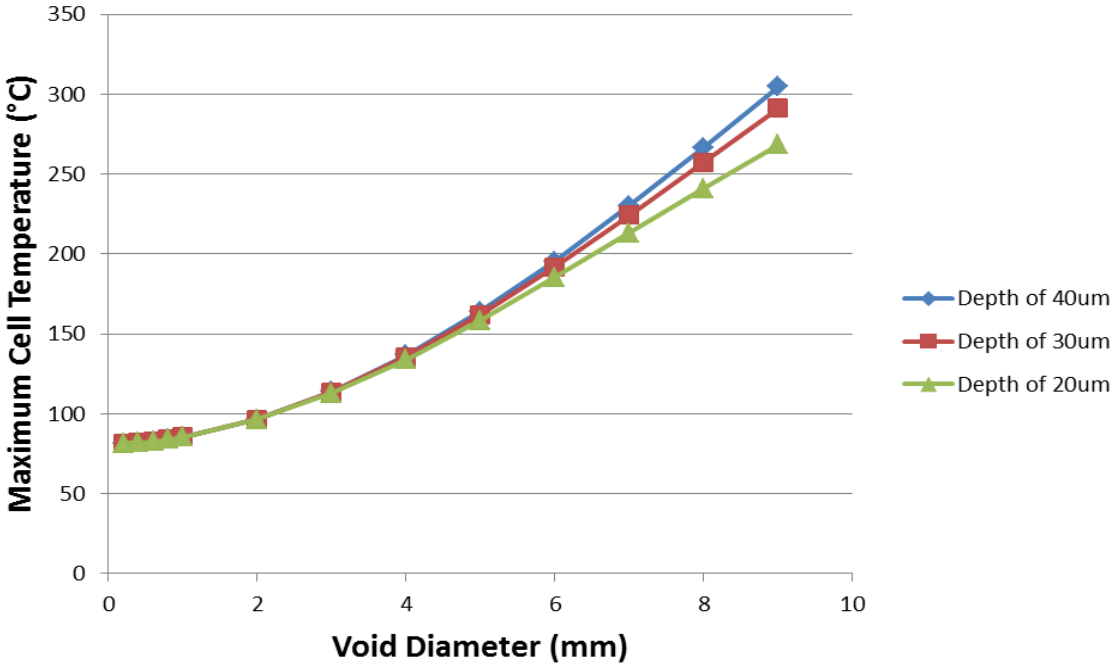

Figure 3-18: Average cell temperature as a function of void diameter and depth.

4 System Design

The design and implementation of the outdoor CPV test and measurement systems are discussed in this section, with particular focus on a hardware description of the systems located at the uOttawa and Little Rock test sites. Since both systems are controlled by the same software, with similar database requirements, software and data management are discussed in site-independent fashion.

4.1 uOttawa PV Test System

4.1.1 uOttawa Test Site Overview

To advance research on subjects related to photovoltaics, an outdoor photovoltaic test system was built at the University of Ottawa to test and characterize photovoltaic technologies in the field. The system was initially built to characterize the novel light-guiding CPV technology of Morgan Solar Inc (MSI) and was further expanded over time to measure local irradiance and environmental parameters. The design, construction, and technical specifications of this test system are described below, as are the technical challenges met and overcome.

The photovoltaic system was installed during the winter of 2011 on the top floor of the University of Ottawa's Mann parkade (45.42ºN,75.62ºW). Enclosed within a fenced area, the approximate locations of the two Golden Sun ring-type solar trackers are indicated in Figure 4-1. Installed on tracker 1 were six Morgan Solar second generation Sun Simba™ CPV panels [24], laid out as shown in Figure 4-2. Each panel was made up of five double strings connected in parallel with each double string consisting of twelve optical assemblies connected in series. No panels were mounted on tracker 2. Each assembly comprised a light-guiding concentrating optic illuminating a 0.5 cm x 0.5 cm high-efficiency Spectrolab C1MJ CPV cell that was bonded to a carrier, and subsequently affixed to the common passive heat sink for the string. Among these panels was a string of ten assemblies, located beneath panel 2, where the *I-V* curve of each cell was individually addressable. This allowed individual assembly/cell performance to be comprehensively tracked and analyzed over time.

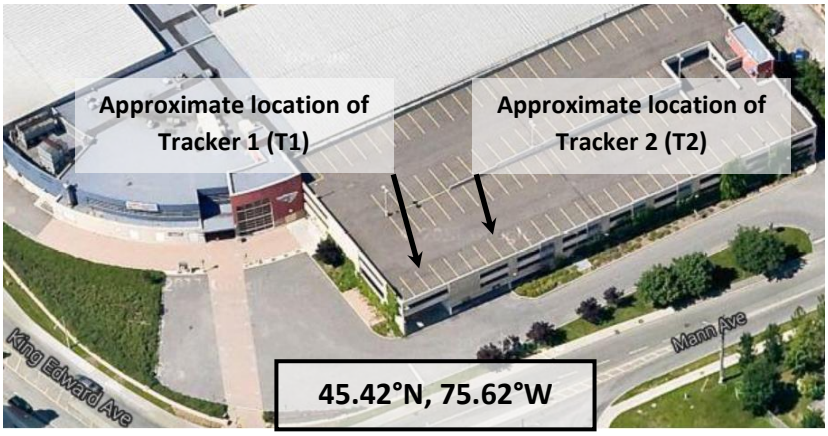

Figure 4-1: Location of the uOttawa test site and trackers.

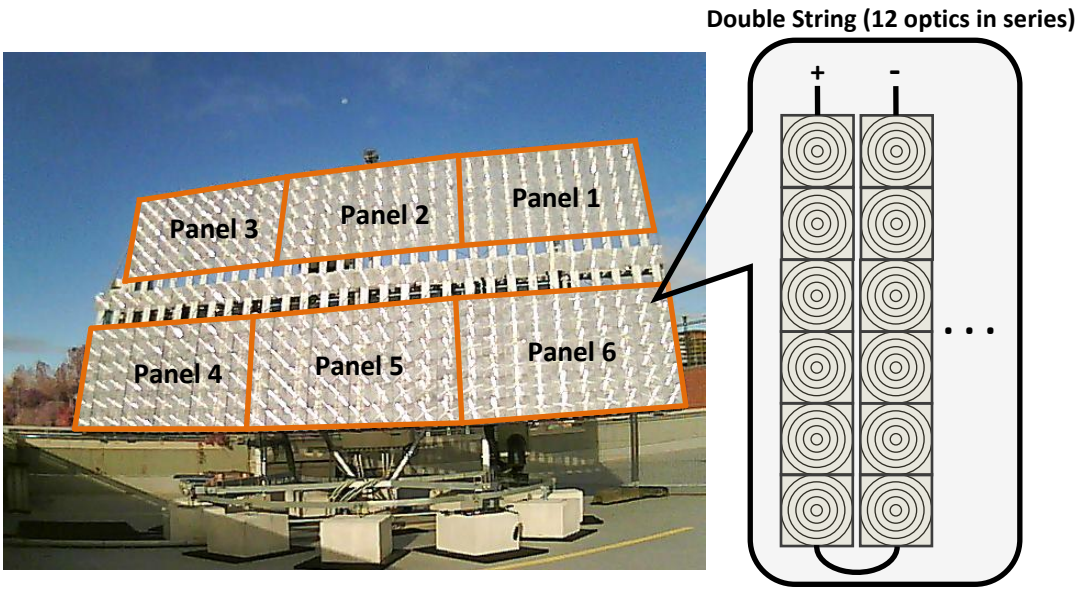

Figure 4-2: Layout of the six panels on tracker 1. Each panel consisted of five double strings (shown on right) connected in parallel.

A custom-built relay-based multiplexer and a Keithley 2600 SourceMeter were used to address and measure the *I-V* curves of the individual assemblies. The panels and individual assemblies were connected to maximum power point trackers (MPPT), from Australian Energy Research Laboratories Pty Ltd (AERL), to maintain maximum power generation at all times and the energy was dissipated by several edgewound 300 W power resistors. The maximum power point currents and voltages were measured with multimeters.

An instrumentation panel was installed on one of the trackers to measure local irradiance and environmental parameters over time. This panel included a pyrheliometer to measure the direct normal irradiance (DNI), a camera directed at the sun to observe cloud conditions, and a spectroradiometer (wavelength range of 350 nm to 1830 nm) to measure the solar spectra. Two additional cameras were installed adjacent to the trackers to monitoring its behavior and the test site conditions. Additionally, a horizontally mounted pyranometer was installed to collect the global horizontal irradiance (GHI). A Suntech 175 W polycrystalline silicon module was mounted on a custom built frame and fixed at a 30º tilt in elevation and south facing in azimuth. The silicon module was grid connected with Enphase M190 208V microinverters. Ambient temperature and wind speed were also monitored.

Data acquisition was controlled by a Campbell Scientific CR1000 datalogger and a remote server. As seen in Figure 4-3, all data were eventually sent to the remote server by way of a remote network connection. Specifically, the datalogger, the spectroradiometer, and the cameras were connected to an Ethernet switch, which was the gateway to the local area network at the test site. The remote server was then able to communicate with the devices on site and to retrieve the data through the remote network connection. The panel current and voltage

measurements were measured at the DC load and sent to the datalogger via an RS-485 link. For the individual optical assembly *I-V* measurements, the datalogger was programmed to control both the multiplexing and the *I-V* measurements to ensure proper timing. The datalogger would first select the assembly to be measured and then send the necessary commands to the Keithley SourceMeter to conduct the measurement. The datalogger recorded the DNI and GHI values by directly measuring the output voltage of pyrheliometer and pyranometer, respectively. Finally, the spectra and the camera images were controlled by remote server through custom software and scripts. All measurements including spectra, *I-V* curves, electrical measurements, DNI and GHI were taken at two minute intervals.

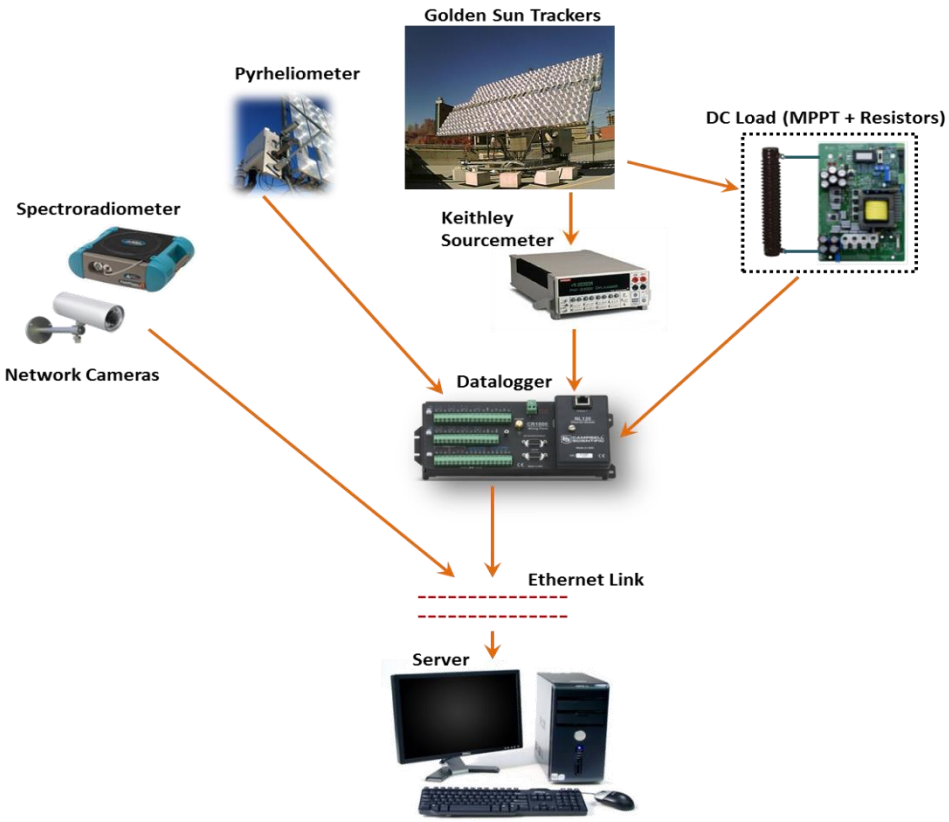

Figure 4-3: Overview of uOttawa test system. Measurements collected stored on a remote server into a database.

4.1.2 The Tracker

The two Golden Sun GS3500 dual-axis trackers installed at the University of Ottawa were ring type and made from galvanized steel. Compared to the alternatives, the Golden Sun trackers were best suited for the test site because they did not need to be secured by any beneath-grade components, being strictly weighted surface mount structures. This was critically necessary because the test site, being on the top floor of a parking garage, did not permit any surface perforation. The trackers offered a 240° tracking range in azimuth and were able to track from 5° (nearly vertical) to 85° (nearly horizontal, the stow position) in elevation, with a tracking accuracy of ±0.1-0.2°. The sun sensor, an array of four photodiodes, was used to achieve the

requisite tracking. Table I summarizes the tracker specifications. The tracker control system was also built by Golden Sun and consisted of a PIC microcontroller with all the necessary peripherals. The two 12 V DC motors used to drive the tracker, one for elevation and one for azimuthal control, were driven by H-bridge circuits. RS-485 and RS-232 transceivers were both available on the tracker control board. An Ethernet-to-serial converter was used to facilitate communication between the remote server and the trackers. From the remote server, software provided by GoldenSun allowed tracker settings to be altered as needed and tracker status parameters to be recorded.

Parameter	Value
Elevation angle range	5°-85°
Azimuth angle range	60°-300°
Tracking Accuracy	0.1°-0.2º
Power Supply	12VDC
Wind Threshold	<40 km/h
Weight Capacity	Up to 450 kg

Table 4-1: GoldenSun GS3500 tracker specifications.

Throughout the course of the project it was clear that the tracker had numerous issues, resulting in unexplained tracking behavior or complete tracking failure. These issues were a result of software bugs in the tracking algorithm, unsatisfactory hardware designs, and inclement weather. The consequences included safety concerns in addition to loss of data and reductions in cumulative energy yield. The specific issues faced are described below, as are the solutions implemented to ensure consistent tracking behavior. To better understand these tracker issues, it is instructive to first understand the expected normal tracking behavior.

Normal operation of the tracker is characterized by going into stow overnight and tracking the sun throughout the day. *Stow mode* or *stow orientation* of the tracker is defined as when the panels on the tracker are in a horizontal orientation (that is, parallel to the ground). Sustained winds greater than 40 km/h have the potential to damage components on the tracker frame if the full force of the wind is encountered, so the tracker is programmed go into stow as a precautionary measure in such cases (including at night). When in stow, the wind load on the tracker is minimized.

The sun tracking algorithm comprises two parts, the open loop component and the feedback loop component. The open loop (or coarse tracking) estimates the sun's position based on astronomical calculations. This gives a good estimate of the sun's location in the sky but it is not sufficient to achieve the ±0.2° accuracy needed for CPV. The deficiency is likely due to certain assumptions inherent to the calculations, such as the nature of the earth's orbit and rotation, as well as inaccurate calibration of the tracker's feedback sensors. Closed loop tracking takes over when the sun is visible, as the sun sensor readings typically enable the sun to be located within the specified accuracy. However, the tracker was found to deviate from its

expected operation in certain situations, and software flaws were determined as the last remaining hypothesis. Unfortunately, details of the tracking algorithm are not known as the GoldenSun software is proprietary.

Position Error

One of the major tracker issues observed was failure to stow at night. Instead the tracker would remain at a near vertical tilt, as shown in Figure 4-4. This occurred on a regular basis, approximately 3 to 5 times a week. At sunrise, the tracker would usually resume normal tracking. However, there were some rare instances when tracking also failed in azimuth at sunrise but continued in elevation. This is shown in Figure 4-5, as evident by the glare on the left side of the tracker. In terms of data integrity, the tracker remaining vertical overnight presented no issue since the tracker almost always functioned normally at sunrise. However, remaining vertical overnight presented safety concerns since the tracker was bearing the full wind load. Additionally, the user was unable to manually stow the tracker overnight because the tracker control system would enter sleep mode during the night time hours. That is, the tracker control hardware would not listen to any commands and so the state of the tracker could not be changed. This meant that if high wind conditions occurred overnight the only way to stow the tracker would be to disconnect the motor from the tracker control hardware and apply 12 VDC directly to the elevation motor. There were also many instances when the tracker would fail to come out of stow and would only follow the sun in azimuth, as seen in Figure 4-6. This was a common occurrence during the summer months.

Figure 4-4: Tracker 1 remaining in a vertical position over night.

Figure 4-5: Tracker 1 tracking only in elevation. Glare, or reflections off of the left side of the tracker makes it apparent the tracker is not on-sun.

Figure 4-6: Tracker 1 tracking only in azimuth. Elevation position of tracker remains stow.

Rather than physically toggling the power to the tracker every morning (the initial short term solution to force normal tracking at sunrise), a Java script was written to reset the tracker through the tracker's software interface. This approach could not be done to force the tracker into stow at night because the tracker control would enter sleep mode and would not accept any instructions. It was noticed, however, that near winter solstice normal tracking tended to prevail but as summer solstice drew closer the frequency of the tracking issues increased, a clear sign of a software bug. Unfortunately, Golden Sun, a Slovakian-based company, could not resolve these issues. It was subsequently discovered that changing the tracker's longitude (an input parameter) to that of Slovakia resolved all the issues. Further trials led to the deduction that the issue was related to a bug in the tracker's software related to the position of the tracker relative to the Greenwich Mean Time (GMT) longitudinal line. That is, the tracker needed to think it was east of the GMT line.

Elevation Sensor

The elevation sensor is a rotary potentiometer that converts the elevation angle of the tracker into an electrical resistance. This is accomplished with a steel cable coupling the tracker's carrier pipe to a wheel attached to the rotary shaft of the potentiometer. Since the carrier pipe is the pivot point in elevation of the tracker, it rotates as the tracker changes its elevation tilt, therefore so does the rotary potentiometer. The elevation sensor mechanism is shown in Figure 4-7 (left panel).

Although this elevation sensor system typically worked, it was susceptible to the elements since it was unprotected. During particularly mild and wet winter storms, it was observed on several occasions that the carrier pipe was encased in ice, as shown in Figure 4-7 (right panel). This caused the steel cable to adhere to the carrier pipe and as the carrier pipe rotated, the steel cable decoupled from the potentiometer wheel. As a result, there was no sensory feedback to the tracker control in elevation and the tracker's behavior became sporadic since it had no accurate sense of its position in elevation. Thus the open loop tracking was completely inaccurate. This also affected the closed loop tracking as the sun sensor has to within a few degrees (~5°-10°) of the solar disk. Correcting this issue required resetting the cable and realigning the tracker and potentiometer positions. This is clear a substandard approach to elevation sensing. A much better approach, easily designed to be weatherproof and unaffected by ice or water build-up, is to use a rotary shaft encoder or a tilt sensor.

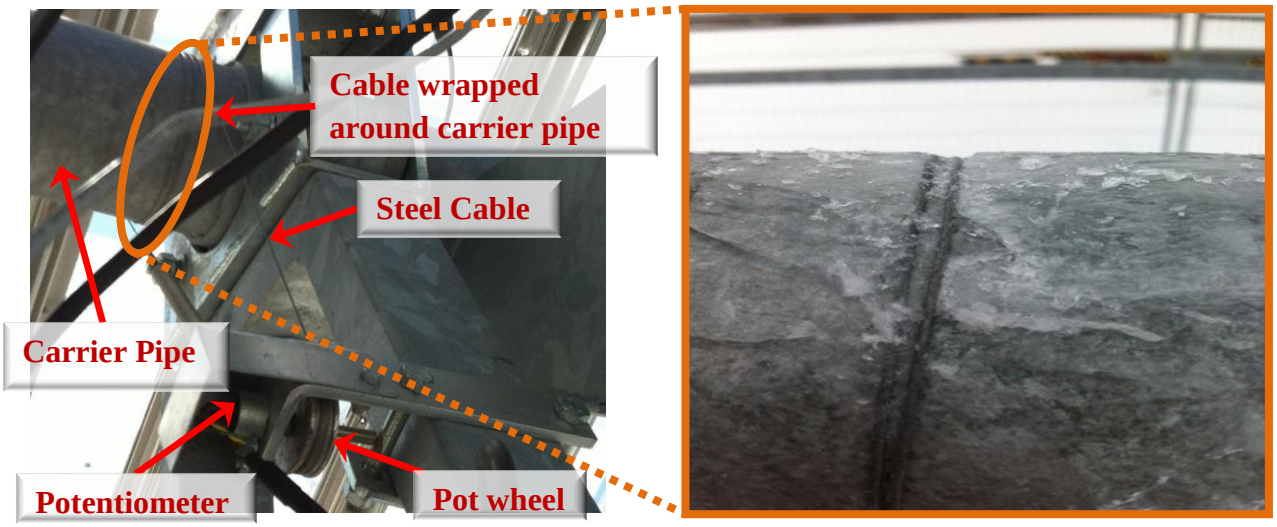

Figure 4-7: Shown on left is the elevation sensor, which is made up of a potentiometer with a steel cable to couple the rotation of the tracker to the potentiometer. Shown on the right is cable that wraps around the tracker's carrier pipe encased in ice. This caused the potentiometer to become uncalibrated as the steel cable was frozen in place.

Icing of rail

During an unusually harsh winter storm, which featured snowfall immediately followed by heavy freezing rain, the tracker rollers to froze to the ice-encrusted rail, as shown in Figure 4-8.

This was a single anomalous event. To restore tracking, the ice was removed manually with a hammer and chisel.

Figure 4-8: Ice build-up on tracker rail resulting in tracker failure. The tracker was unable to rotate in azimuth.

Divots

As shown in Figure 4-9, tracker 2 formed a divot in the tracker rail due to the wheel spinning in place and grinding the rail down. This happened on three different occasions. The formation of the divots can be attributed to a tracker control malfunction or software bug. That is, the azimuth motor wheel would continue to turn in place despite the tracker being stuck. Normally, the tracker control would prevent the azimuth motor from turning if the tracker sensed no movement. The first divot was formed by the tracker running into its physical limit. The second divot was formed when an adjacent roller on the tracker got stuck in the first divot. This caused a second divot to form at the location of the azimuth motor wheel. A third divot was created in a similar fashion. The divots were repaired by building the gaps back up to an even surface through welding and grinding. The welding was done by John Perrins of the uOttawa engineering machine shop. No divot formation was observed on tracker 1.

Figure 4-9: Divot formed in tracker rail due to the grinding of the drive wheel on the tracker ring.

Tracker Communications

On both trackers, the communication protocol originally used to communicate with the tracker controller was RS-485. Specifically, the tracker control board was connected to the Ethernet switch at the test site to provide remote communication with the tracker controller. An RS-485/232/Ethernet converter was connected between the Ethernet switch and tracker controller to constitute the tracker communication.

In April 2011, the RS-485 communication line on for tracker 1 permanently failed. It was determined that the failure occurred within the tracker 1 controller. Unfortunately, the exact hardware or software failure could not be determined. It is likely that the cause of the failure was due to a power surge or an electrical transient condition since the communication failure coincided with the electrical shutdown of the adjacent SITE building. Replacing the RS-485 transceiver chip did not correct the problem. Therefore, the RS-232 transceiver on the tracker control board was used instead as a permanent solution. Also, an optical isolation circuit was implemented between the tracker controllers and the RS-485/232/Ethernet converter as an added surge protection measure, and to prevent ground loops. There have been no further communication issues since the optical isolators have been installed.

Optic Misalignment

Upon installation of the panels, their alignment (that is, their requirement to be normal to the sun's rays) was measured with a custom built alignment tool, designed by SUNLab graduate student Matt Wilkins, that enabled elevation and azimuth misalignment to be determined. The conveniently accessible individual optics within panels were measured, and the results are shown in Figure 4-10. White spaces in the panel maps represent optics whose alignments were not studied. The optics showed broad trends in misalignment within each string, with a slight westward (positive) azimuth bias and a more significant downward (negative) elevation bias, as detailed below. The cause of the optic misalignment was the result of imperfections in the string

manufacturing process, which permanently set their position. Consequently, individually correcting optic misalignment within strings was not possible. Rather, a global approach was taken to achieve the best possible average optic alignment over the tracker. With each optic having an angular acceptance of $\pm 0.6°$, the aim was to ensure that the overall alignment error was within this range for as many optics as possible. Determining the overall misalignment was done by summing the elevation and azimuth alignment errors in quadrature. The frequency of optic misalignment was determined, shown by the histogram in Figure 4-11, and a marked number of optics were found to be outside of the required angular acceptance.

To shift the majority of optics to within the specified range, a global azimuthal adjustment over the entire tracker was made and a global elevation adjustment was made for the top frame of the tracker and another for the bottom frame of the tracker. The adjustment factors were determined by averaging the alignment errors. That is, the average azimuthal alignment error over the entire tracker was 0.38° so a -0.4° correction was applied. In elevation it was found that the upper frame of the tracker had an average elevation alignment error of -0.61° whereas the lower frame of the tracker had an average elevation alignment error of -1.93°. Therefore, an overall adjustment in elevation of 0.6° was made to the entire tracker to correct the upper frame and partially correct the lower frame. Subsequently, an adjustment in elevation of 1.3° was given to the bottom frame on the tracker to complete the adjustment.

The tracker adjustments made to correct the alignment errors were accomplished by shimming and re-bolting the frames to adjust the overall frame alignment in both azimuth and elevation. These adjustments required the boring of bolt holes on the tracker. After the adjustments were made, optics alignments were again measured and the average alignment error was reduced to 0.06° in azimuth and 0.08° in elevation over the entire tracker. As shown by the frequency histogram in Figure 4-12, the global adjustments improved the alignment so that over 70% of all measured optics were within the 0.6° acceptance angle.

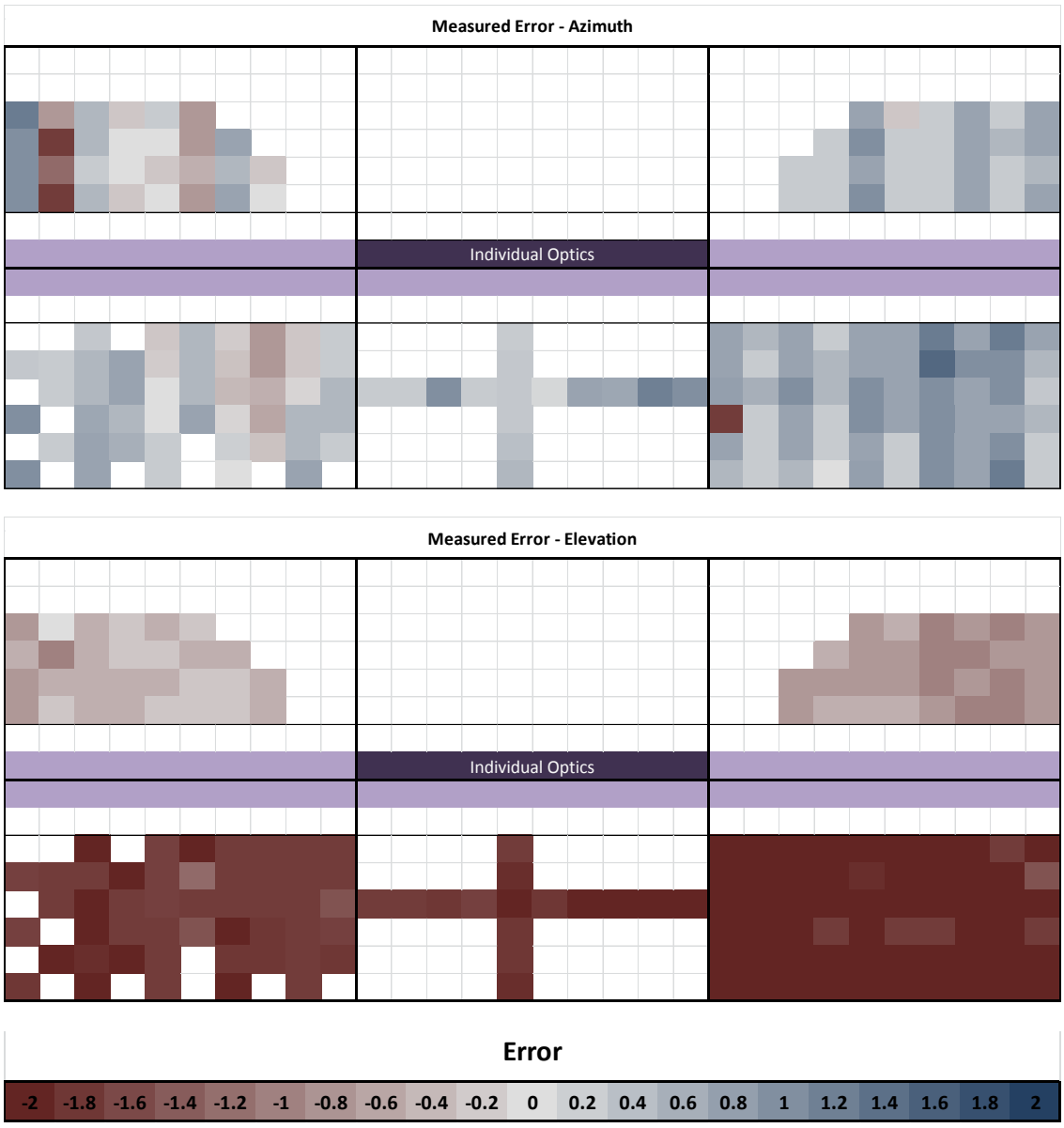

Figure 4-10: Measurement of optic alignment after installation of MSI GenII panels. Positive error in azimuth means the optic is facing too much towards the west. Positive error in elevation means the optic is tilted too high.

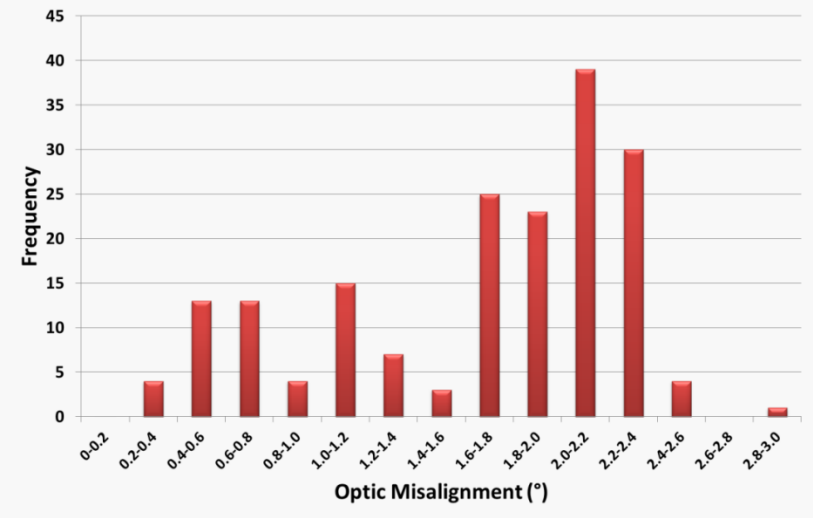

Figure 4-11: Histogram of optic misalignment before alignment correction.

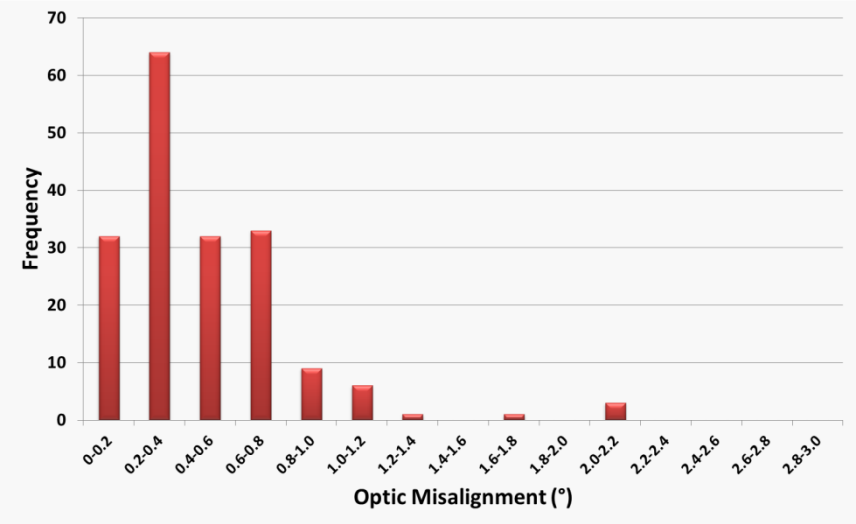

Figure 4-12: Histogram of optic alignment after alignment correction.

Even though the overall alignment of the optics was improved, there was still a fair number of optics with some degree of misalignment. For each misaligned optic, the alignment error represented a decrease in solar irradiance being focused onto the cell. This resulted in a decrease in panel efficiency. However, since double strings of sixteen series connected optics were wired in parallel, the optic that was most misaligned would limit the current produced by the string and thus reduce the overall efficiency of the double string. Subsequently, this also represented an efficiency loss in the panel. Since the currents and voltages were measured from two panels at a time, there was not enough information to experimentally determine this efficiency loss, so no further calculations were pursued.

4.1.3 Datalogger

The CR1000 Campbell Scientific datalogger was used for much of the test site measurement and control. The CR1000's ruggedness and range of measurement and control capabilities made it an ideal choice. In particular, the datalogger had several analog input ports with 0.33 μV resolution, four RS-232 communication ports, and several digital input/output ports. The analog input ports were used to measure millivolt signals from devices such as the pyrheliometer and the pyranometer. Specifically, the datalogger could allow for eight differential analog voltage measurements or sixteen single-ended measurements. The RS-232 ports allowed for communication between the Keithley SourceMeter and the datalogger. Similarly, the RS-232 port coupled with an external RS-232/485 converter allowed the datalogger to retrieve telemetry from the DC load and control the multiplexer for switching of the individual optics. The datalogger was programmed to perform all of its control and measurement routines using the on-board Campbell Scientific flavour of the BASIC programming language. To achieve two minute measurement granularity, the datalogger program executed every two minutes. The measured data was temporarily stored in the datalogger's SRAM and later retrieved by the remote server.

4.1.4 Pyrheliometer

An Eppley normal incidence pyrheliometer was installed on one of the trackers to gather the direct normal incidence (DNI) portion of the incident sunlight, as shown in Figure 4-13. The sensing element of the pyrheliometer was a fast-response wire-wound plated multijunction copper-constantan thermopile (thermocouples wired in series). The thermopile was contained within a black disk with a flat optical absorption profile to convert the DNI insolation into a heat flux. The thermopile would then heat up and produce a measureable electrical signal proportional to the DNI. Encasing the thermopile was a cylindrical tube painted blackened on the inside, with a quartz window over the circular aperture to prevent environmental contamination.

Figure 4-13: Pyrheliometer as it is mounted on tracker 1.

The pyrheliometer has a sensitivity of 8.57 $\mu V \cdot m^2/W$, and outputs a voltage signal in the μV range. It was connected directly with twisted pair cable to one of the differential analog inputs on the datalogger. Given the small signal output level, the differential input ports on the datalogger were necessary to prevent common mode interference from interfering with the pyrheliometer's signal.

Principal sources of error in the DNI measurements were the temperature dependence of the pyrheliometer, its slight non-linearity, and soiling of the quartz window. Generally, misalignment was not a significant source of error as the pyrheliometer had an angular acceptance of 5.7º, which was much greater than the tracking accuracy of the tracker. That is, tracking would have to be noticeably misaligned to affect the pyrheliometer measurement, and its data would clearly be rejected. The temperature dependence of the pyrheliometer induced a maximum measurement error of ±1% over a temperature range of -20 ºC to 40 ºC. Typically, the error was much lower than this as the maximum measurement error occurred at the temperature extremes. A polynomial curve was generated based on information provided by the vendor to compensate for this measurement error. The pyrheliometer was linear within ±0.5% over irradiances between 0 W/m^2 and 1400 W/m^2. The nature of the variations within this range was not known and remained a source of error in all measurements. Finally, it was determined that soiling was a significant source of error in measurements. For example, on September 9 of 2012 the pyrheliometer was cleaned around 1 pm, which corresponded to a noticeable increase in the DNI measurement, as shown in Figure 4-14. This increase corresponded to a relative increase of approximately 2.2 %, a significant source of error. Before this cleaning, the pyrheliometer had not been cleaned for several months. To reduce the source of error due to soiling a cleaning schedule was established. The pyrheliometer was cleaned biweekly or after any significant rainfall or snowfall event.

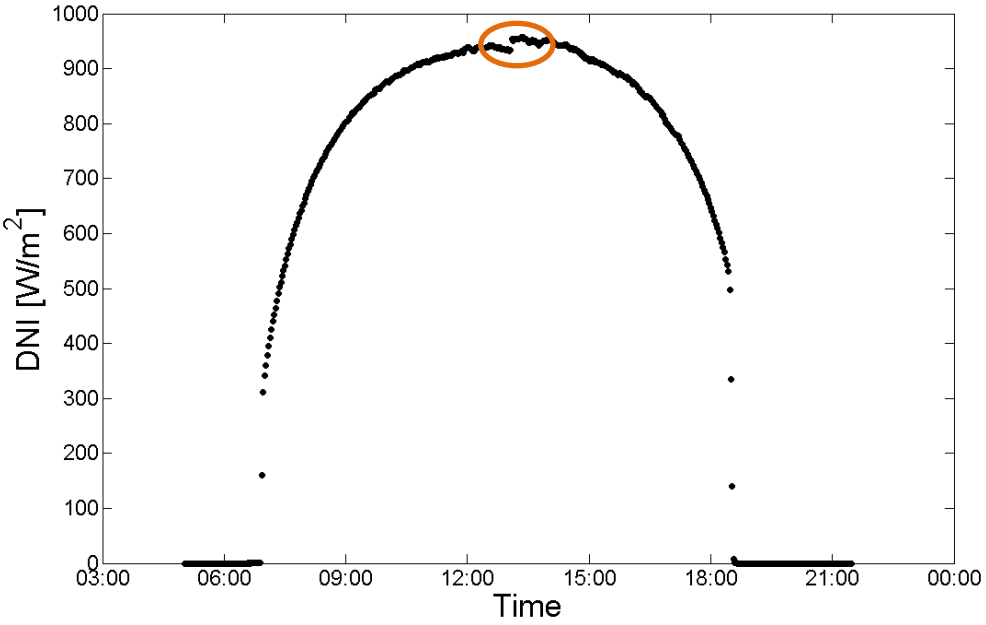

Figure 4-14: Effect of cleaning the pyrheliometer. An increase of 2.2% is observed showing that the effect of soiling is significant.

4.1.5 Spectroradiometer

To measure the spectral content of the incident sunlight, an ASDi Fieldspec spectroradiometer was installed on tracker 1 as shown in Figure 4-15. A direct attachment was used to couple DNI into the spectroradiometer's optical fiber. Also, a heater was installed with the spectroradiometer to keep it operating within its specified temperature range. The spectroradiometer measures spectral DNI, and is an absolutely calibrated instrument that measures the DNI power spectrum of the sun. This is different than a spectrometer, which can only take relative measurements since it is not absolutely calibrated. Absolute spectral measurements are required because the earth's atmosphere significantly alters the solar spectra, depending on air mass and atmospheric constituents. That is, the spectra observed at the surface of the earth are affected by the location of the observer, the air mass, optical depth of aerosols such as ozone, optical depth of water, and cloud cover. Generally, variations in the spectral content of the light can occur over the course of the day or over a year. For example, over the course of a day stronger Rayleigh scattering occurs near sunrise and sunset due to the higher air masses at these times, which induces a red-shift in the measured spectra. Alternatively, the optical depth of water and types of cloud cover may exhibit trends over the course of the year, which might predictably affect the absorption lines in the spectra over the course of a year. Determining these trends is important for CPV since changes in the incident spectra can measurably affect the cell performance. Thus, quantitative measurements of spectra assist the design optimization of CPV systems at specific locations.

The Ethernet communication protocol was used to interface with the spectroradiometer since it was the default protocol of the instrument. This allowed the spectroradiometer to

communicate directly with the remote server to facilitate data collection. A software program implemented in LabView was developed by graduate student Matthew Wilkins to perform the communication and collect the spectra at two minute intervals.

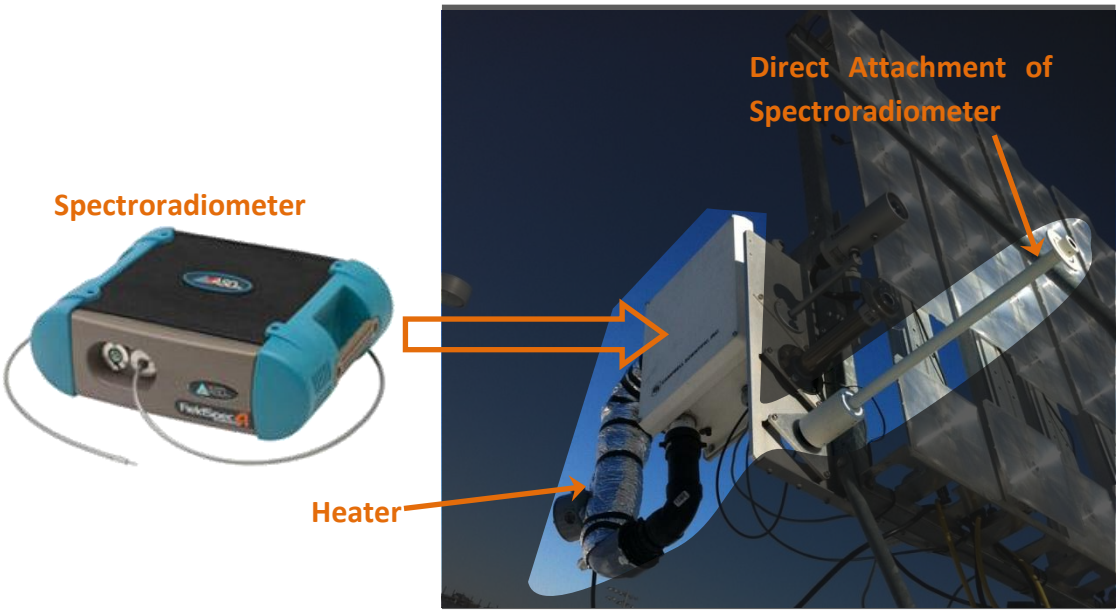

Figure 4-15: Spectroradiometer as it is mounted on tracker 1. The spectroradiometer is mounted inside a weatherproof environmentally controlled enclosure. The direct attachment limits the acceptance angle of the incident light so that the spectra of the DNI is measured.

4.1.6 DC Load

A DC load was created to dissipate the electrical energy generated by the photovoltaic panel and to ensure that the panels operated at their maximum power point. This allowed the electrical performance of the panels to be measured under their expected operating conditions, since most photovoltaic systems are now installed with, or are expected to be installed with, a maximum power point tracker. This is particularly important for grid connected applications where microinverters and module level power optimizers are used to keep the panels operating at their maximum power point. The popularity of these optimizers has been mainly driven by their value proposition in that they reduce the levelized cost of energy for a photovoltaic system by harvesting up to 25% more energy [4,5]. Finally, installing a DC load system mitigated safety issues associated with connecting the system to the grid, and also expedited the installation process.

The DC load consisted of four AERL SMV24 charge controllers for maximum power point tracking, power resistors to dissipate the electrical energy, and two multi-channel input analog modules to measure panel maximum power point voltages and currents. All of these components were installed in an outdoor-rated steel enclosure with forced air intake to keep the power resistors and the surrounding equipment cool. The enclosure was mounted on tracker 1. The DC load wiring diagram is shown in Figure 4-16. Of the four AERL MPPTs, three of them were used for panel maximum power point tracking. Since there were six panels installed on

tracker 1, each MPPT had to provide maximum power point tracking to two panels. This was done by wiring two panels in parallel and connecting them to an MPPT. The MPPTs then delivered the electrical energy to the power resistors, labelled as R_L in Figure 4-16. Furthermore, the AERL SMV24 MPPT's were buck converters meaning they convert the input DC voltage to a lower output DC voltage by some factor. In theory, the input and output power of a DC/DC buck converter is constant. Thus, the output current is higher at the output than the input to compensate for the voltage being lower at the output than at the input. However, there are losses associated with the conversion as a result of the conversion process. Specifically, the efficiency of the conversion is dependent on the V_{in}/V_{out} ratio or conversion factor. The AERL MPPT had peak conversion efficiency when bucking by a conversion factor of 1.6 [38]. Moreover, the Morgan Solar second generation panels had a V_{OC} of 35.2 V, a V_{mp} of approximately 30 V, and an output power of approximately 300 W per panel. With this in mind, the MPPTs were set to provide an output voltage of 24 V, which meant bucking the input voltage by a factor of 1.25 (30 V/24 V) was required. This was an appreciable departure from the peak efficiency condition that occurs when bucking the input voltage by 1.6x. However, the conversion factor of 1.25 was still acceptable [38].

The maximum power point voltages and currents were measured at the inputs of the MPPTs. The voltages were measured with a SuperLogics 8017R-A5 analog input module, which had the ability to measure DC voltages up to +/-150 V [39], well above the V_{OC} of the Morgan Solar panels. Similarly, the maximum current was measured by placing a shunt resistance between the panel and MPPT and measuring the voltage across it. The shunt resistance used was a 50 mΩ resistor and the voltages across the shunt resistor were measured with a SuperLogics 8018 mV analog input module. Both of the SuperLogics modules transferred their measurement data to the datalogger over an RS-485 connection every two minutes.

The power resistor choices were constrained by the nature of the MPPTs. Since the AERL MPPTs have a two stage charging profile designed to charge batteries, their output setting should not exceed 24 V otherwise it would interpret the load as a fully charged battery and it would cease to extract energy from the panels. Consequently, the MPPTs would no longer provide maximum power point tracking for the panels since the MPPTs would not be providing a load, and the panels would be under open circuit conditions. On the other hand, if the output voltage was significantly below 24V, and well beyond the 1.6 (~19V) conversion factor, then the conversion efficiency of the MPPT would drop. Therefore, a resistance value must be chosen that provides a relatively high voltage output. Knowing that the maximum power output of two panels would be approximately 720 W, the required load resistance would be

$$R_L = \frac{V^2}{P} = \frac{(24\ V)^2}{720} \sim 0.8\ \Omega\,. \tag{4.1}$$

However, the maximum output was based on the panel STC rating, and it was determined that the two panels would be producing much less than 600 W most of the time. A lower power, or lower current, implies that a larger resistance is needed to maintain a higher voltage output.

Therefore, an output resistance of 2.5 Ω was chosen. This was implemented as two 5 Ω, 300 W power resistors wired in parallel to provide the 2.5 Ω output load with 600 W of capacity to dissipate the energy per MPPT. In a similar manner, the load resistance for MPPT 4 was determined to be 20 Ω since the STC rating for the string of the ten individual optics was approximately 60 W.

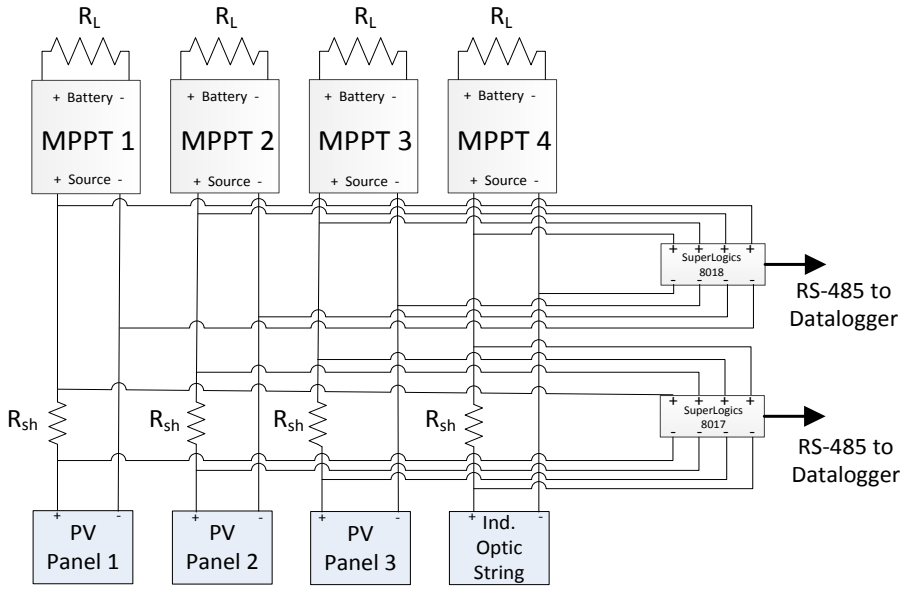

Figure 4-16: DC load wiring diagram. The SuperLogics 8018 measured the input PV voltage and the SuperLogics measured the input PV current by measuring the voltage across a small shunt resistance. The RS-485 communication protocol was used to retrieve data from the SuperLogics devices.

Shown below in Figure 4-17 are the assembled and fully connected DC loads. On the left are the power resistors mounted to a vertical aluminum plate to isolate the wiring and electronics from the heat generated by the power resistors. An intake with a fan to continuously provide forced air flow over the resistors is seen at the bottom left of the box. The exhaust vent is seen at the top left. To the right of the divider are the AERL MPPTs, the SuperLogics analog input modules, a 24V DC power supply to power the SuperLogics modules , 6 kA rated 20 A triple-pole single throw circuit breakers for circuit protection and safety as recommended by AERL [40], and terminal blocks to facilitate the required connections.

Figure 4-17: Fully assembled DC load. The four MPPT's, circuit breakers, terminal blocks, and the SuperLogics measurement devices are seen on the right side of the enclosure. The cooling fan and power resistors can be seen on the left.

4.1.7 Individual Optic Assembly IV Measurements

The individual optic *I-V* measurement system was built to monitor the individual performance of nine individually-addressable optic assemblies over an extended period of time. The motivation behind measuring *I-V* curves is that the *I-V* curve provides all the parameters needed to characterize the performance of the cell such as V_{OC}, V_{mp}, and fill factor. *I-V* curves can also lend insight into why a particular cell might be underperforming or help determine cell failure mechanisms. The *I-V* measurement system consisted of several different components, which were all controlled by the CR1000 datalogger.

The string of individual optic assemblies was connected to a custom built multiplexer board designed and fabricated by graduate student Matthew Wilkins. The multiplexer connected all the optic assemblies in series but would isolate an optic for *I-V* measurement when instructed. As seen in Figure 4-18, each optic assembly had its own relay that could be switched on and off by a SuperLogics 8043 module. The SuperLogics 8043 module was operated as a set of control switches for the relays and it contained 16 channels (or switches) to control the relays. All relays were provided with 24 V and the SuperLogics 8043 module would close the desired control circuit to switch the relay on and connect the desired individual optic assembly directly to the Keithley 2440 sourcemeter. The SuperLogics 8043 modules, and implicitly the relays, were controlled by the datalogger via an RS-485 connection. Likewise, the Keithley 2440 was also instructed by the datalogger and sent the measurement data back to the datalogger over an RS-485 link. The proper timing of the relay control and measurements by the Keithley was

established by the datalogger. It is important to note that Figure 4-18 is a simplified version of what was implemented since the individual optic assemblies were connected in series when the relay was turned off, which is not reflected in Figure 4-18.

Note that a four wire measurement between the Keithley 2440 and the relay board was made. This eliminated resistive losses induced by the cable between the Keithley 2440 and the relay board. This was particularly important since the distance between the Keithley 2440 and the relay board was over 15 m. However, the two-wire connections between the relay board and the individual optic assemblies introduced resistive losses in the *I-V* measurement and their contributions needed to be removed to determine the cell *I-V* curves.

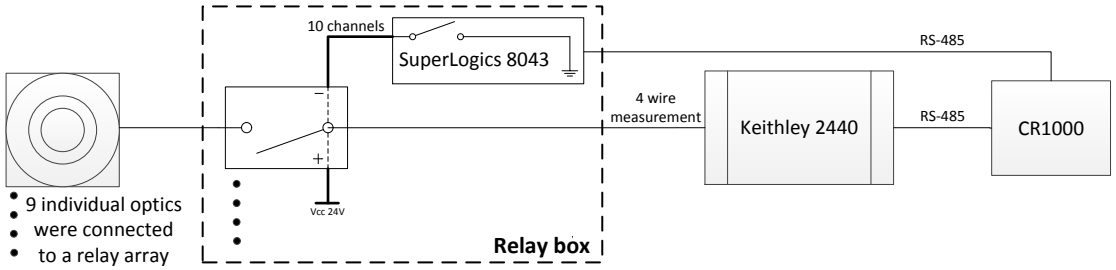

Figure 4-18: Simplified circuit diagram of I-V measurement system. The CR1000 datalogger controls the switching of the relays and the timing of the IV measurement done by the Keithley 2440.

4.1.8 Cameras

Three IP network cameras were installed at the uOttawa test site to maintain a visual log of tracker behavior as well as a visual log of sky conditions. Two of the three cameras were installed to monitor the trackers, one for each tracker. The third camera was installed on tracker 1 and aimed directly at the sun to record cloud conditions, in order to determine how different types of cloud cover would affect the CPV data. For example, high level cirrus or cirrostratus type cloud cover would partially attenuate our DNI, depending on the thickness and pervasiveness of the cloud cover. The network cameras communicated directly to the remote server over an Ethernet network connection. A script was written to capture the images from the three cameras in two minute intervals. The images were stored on the server for further analysis.

4.2 Little Rock PV Test System

4.2.1 Little Rock Test Site Overview

An important aspect of CPV currently being considered is the suitability and cost effectiveness of CPV deployments in lower sunlight regions such as in Ottawa, Ontario [41]. As such, it is important to understand differences in the long term performance and behavior of the Morgan Solar light-guiding technology in different locations and climates if increased deployments into lower insolation regions are to be made. In particular, there might be differences in electrical performance due to climactic variations and spectral differences between two different locations. Likewise, different climates may bring out different reliability issues. These challenges and potential pitfalls must be well understood to design a product that can be deployed widely and

reliably. It is for these reasons that a CPV test system was designed for Little Rock, California. That is, third generation panels were installed at the University of Ottawa test site as well as at Little Rock, California for the purposes of comparing their performance. As such, a second test and measurement system was built for Little Rock, California (34.54°N, 117.94°W).

The primary objective when designing the Little Rock test system was to build a system that would provide data sets as similar as possible to the data sets available at the University of Ottawa. To ensure that the data streams would be equitable, which would allow for direct comparisons of system performance, similar instrumentation, data handling and test methodologies were implemented by designing and constructing a facsimile of the test system built at the University of Ottawa. An outline of the Little Rock system is shown below in Figure 4-19. Four Morgan Solar third generation panels were installed at the Little Rock test site. Three of the four panels were third generation panels containing 6 double strings (90 optics) connected in parallel. The fourth panel was a custom built panel containing thirty individually-addressable optics for *I-V* measurements and the instrumentation rack. The latter included a pyrheliometer to the measure the solar DNI, a spectroradiometer to measure the solar spectra, and a network camera to maintain a visual log of the sky. A second network camera was installed at a location adjacent to the tracker to maintain a visual log of the tracker. Again, AERL charge controllers were used to provide the maximum power point tracking for all four panels. The output maximum power point currents and voltages were measured. The custom built multiplexer and a Keithley 2440 sourcemeter were used to electrically isolate the individual optics and measure the corresponding *I-V* curves. A CR1000 datalogger controlled the individual *I-V* measurements and collected the DNI and panel level measurements. Due to the remote location of the site, a 3G internet connection was provided by Morgan Solar. This allowed the measured data to be transferred back to the server at the University of Ottawa. However, despite the similarities between the Little Rock and uOttawa test site there were some key differences between the two systems. These differences arose out of necessity caused by differences in site landscape and layout as well as logistical constraints. Only the differences between the uOttawa and Little Rock test sites will now be discussed.

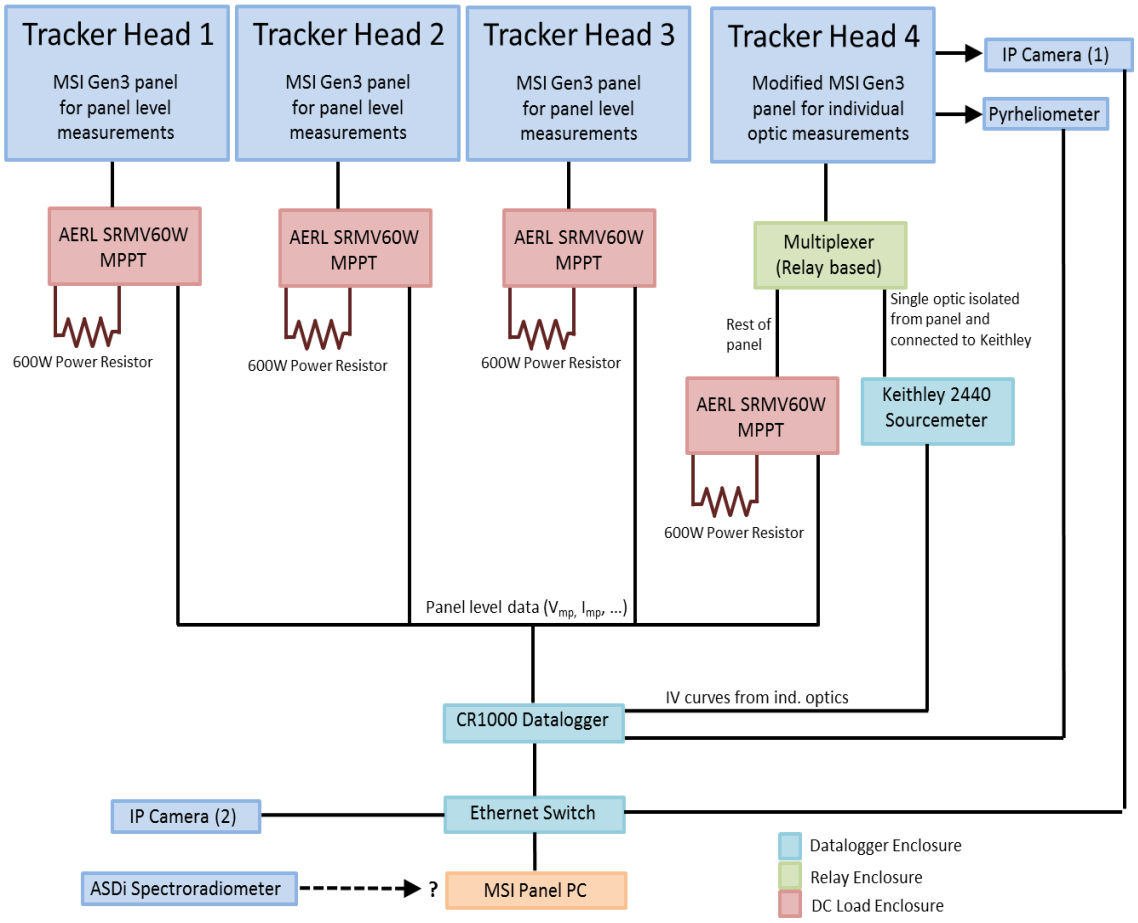

Figure 4-19: Overview of Little Rock test system.

4.2.2 Morgan Solar Savanna Tracker

One of the main differences between the two sites was the choice of tracker. In Little Rock, the Morgan Solar Savanna tracker was used instead of the Golden Sun tracker. The Savanna tracker offered greater reliability over the Golden Sun tracker, and numerous Savanna trackers were already installed at the Little Rock test site, which made it the logical choice for Little Rock. The Morgan Solar Savanna trackers provided two-axis tracking and consisted of a self-ballasting box frame with four individual tracking heads at each of the four corners of the frame, as labelled in Figure 4-20. Each of the individual tracking heads were driven by a separate motor. A panel frame was mounted to each of the tracking heads. Mounted on three of the four panel frames were three regular Morgan Solar third generation panels. The custom built individual optic and instrumentation panel was built on the fourth panel frame.

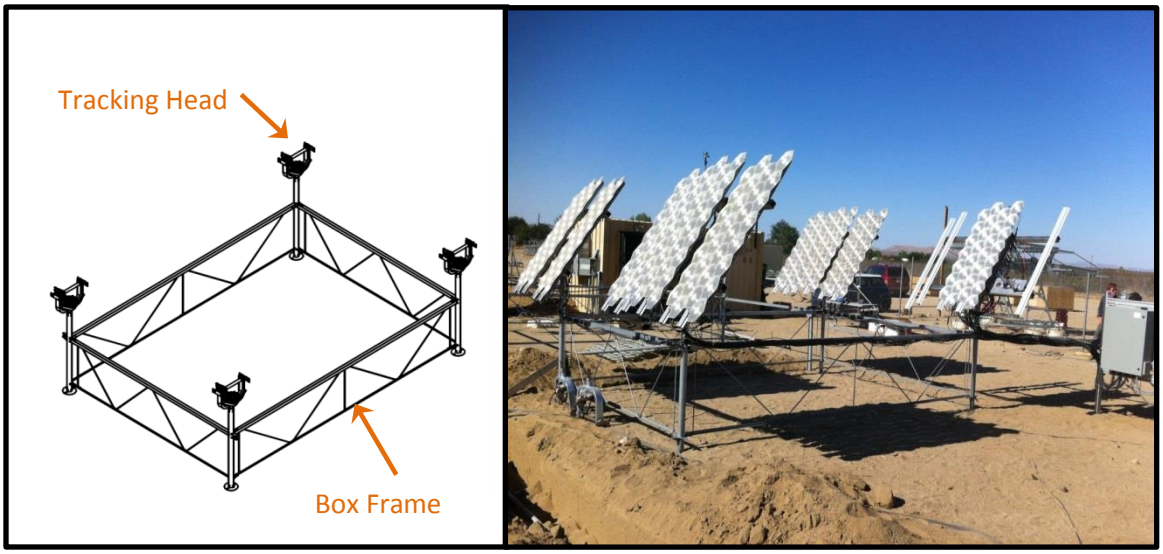

Figure 4-20: Drawing of MSI Savanna tracker on left with GenIII SunSimba panels mounted on an MSI Savanna tracker installed at Little Rock, CA on the right.

4.2.3 Enclosure Mount Frame

Due to the weight load limits of the Savanna tracker, the equipment and their enclosures could not be mounted on the tracker frame. Therefore, an enclosure mounting frame was constructed to hold the four equipment enclosures. The original design is shown in Figure 4-21a: the DC load enclosure, shown in purple, contained the AERL MPPTs; the resistor box, shown in red, contained the power resistors; the box shown in green contained the datalogger and Keithely sourcemeter; and the enclosure shown in light blue contained the multiplexers. The installed enclosure frame, mounted adjacent to the tracker frame, is shown in Figure 4-21b. The final design ended up deviating slightly from the original design; whereas the original design had planned for four legs piled directly into the ground, the final design was two legs secured on concrete piles.

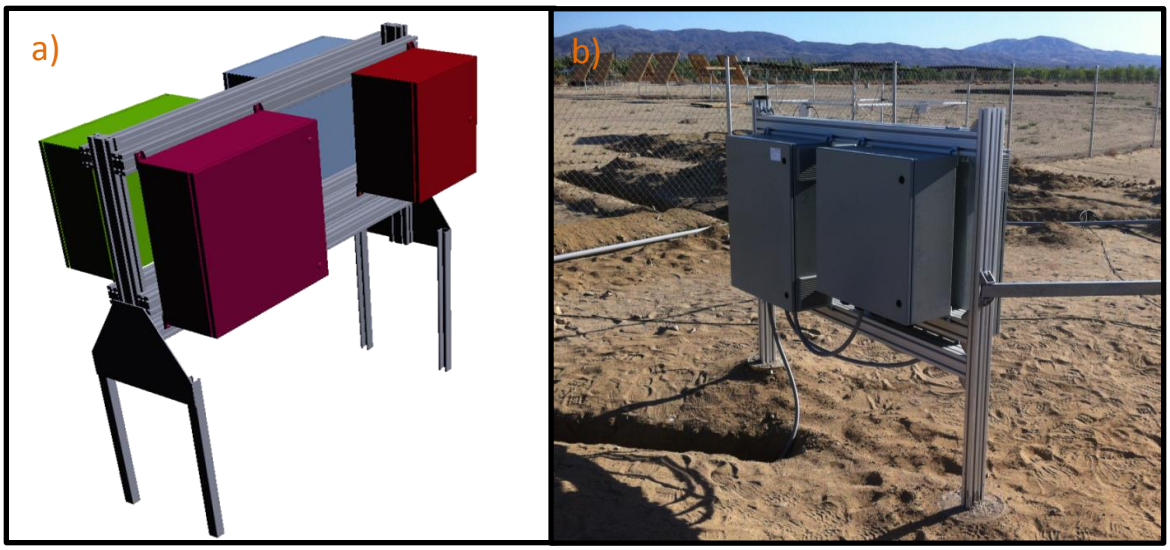

Figure 4-21: a) Design of enclosure frame showing the four enclosures. b) The enclosure frame post installation at the Little Rock test site.

4.2.4 Datalogger

To mitigate network congestion and daytime data loss, the measured data were stored on the datalogger and cameras during the day and transferred to the server at uOttawa during the night. This was necessary since remote troubleshooting and equipment monitoring was sometimes required during the daytime hours. Since the 3G connection provided limited bandwidth, there was a risk of data loss due to possibly congested network traffic. To accomplish this, the datalogger was equipped with a 2 GB compact flash card so that multiple days' measurements could be internally stored.

4.2.5 DC Load

At the time when the DC Load destined for Little Rock was designed, the MPPTs used at the uOttawa test site (model SMV24) were no longer in production. Rather, the AERL SRMVW was used, which was an improved version of the SMV24 model [42]. The newer SRMVW model featured improved conversion efficiencies and onboard measurement and storage capabilities. Specifically, the SRMVW model enabled very rapid measurements of both open circuit voltage, and maximum power point current and voltage. It could do this at one second intervals for several weeks of data storage capability. Communications with the SRMVW MPPTs were accomplished over a CAN (controller area network) bus protocol. The data from the MPPTs were collected by the datalogger, which required an Ethernet to CAN converter to bridge the datalogger and the MPPTs. Also, this meant that the datalogger program needed to be altered significantly from the program used at uOttawa to retrieve the CAN data packets that were contained within the Ethernet packets. Finally, edgewound power resistors were used to dissipate the electrical energy.

Unlike the uOttawa test site where the power resistors and MPPTs were mounted inside the same enclosure, the power resistors and the MPPTs at Little Rock were separated into their

own separate enclosure, as shown in Figure 4-22. This recourse was a prudent since the ambient temperatures at Little Rock consistently reached as high as 45 °C. With temperature limits of the MPPTs being below 50 °C [40], it was important to separate the MPPTs from the large heat load of the power resistors. The MPPT enclosure contained the AERL MPPTs, the Ethernet/CANbus converter module, circuit breakers for circuit protection, and a 100 cubic foot per minute (CFM) fan to provide forced air cooling to keep the components below 50 °C. Likewise, 2500 W load inside the resistor enclosure required forced air cooling to keep the air temperature inside the enclosure manageable. To accomplish this, a fan was installed to provide forced air cooling. Assuming a maximum allowable temperature inside the enclosure temperature of 70 °C (158 °F) and a worst case ambient temperature of 50 °C (122 °F), the required fan capacity in CFM (for temperature in degrees Fahrenheit) was [43]

$$CFM = \frac{P \times 3.17}{(T_{enclosure} - T_{ambient})} = \frac{2500\,W \times 3.17}{(158°F - 122°F)} = 220\frac{ft^3}{m}. \quad (4.2)$$

Applying a 25% safety factor, a 300 CFM fan was installed to keep the resistor enclosure sufficiently cool. Further, the enclosures were shaded so that solar irradiance would not significantly increase the heat load. High temperature wiring was installed inside the enclosure to avoid cable degradation and to ensure long term load reliability. Filters were also installed at both the intake and exhaust ports of the enclosure to prevent dust ingress as well as to aid in the pressurization of the enclosure. Finally, the intake fan was placed on the lower half on one of the sides of the enclosure while the exhaust was placed near the top on the opposing side of the enclosure. This allowed maximum air exchange by taking advantage of both the direction of air flow provided by the fan and the buoyant air flow effects caused by air temperature differences.

Figure 4-22: On left is the MPPT enclosure containing the AERL SRMVW MPPTs and the associated circuit breakers and terminal blocks. Shown on the left is the resistor containing the power resistors and cooling fan.

4.2.6 Instrumentation

An Eppley pyrheliometer was mounted on the tracker to measure the DNI at the Little Rock test site. A custom designed and machined aluminum mounting plate was used to facilitate the mounting of the instruments on the tracker, as shown in Figure 4-23. Also, two network cameras were installed at the Little Rock test site. One camera was mounted on the tracker to record a visual log of the sky and the other was mounted on an adjacent fence to log the tracker behavior. Each of the cameras was set up to record daytime images to an onboard SD card. Using a Python script, the images were then transferred at night to the server at uOttawa . Finally, three type-T thermocouples were installed on heat sinks of individual optic assemblies to measure their temperature. This would allow cell temperatures to be estimated.

Figure 4-23: Pyrheliometer and camera mounted on the Savanna tracker shown on the left. On the right is the camera facing the tracker as it is installed at the Little Rock test site.

4.3 Software

The server at uOttawa facilitated data collection through both custom and commercial scripts and software packages, and accommodated storage of all the collected data. Due to the large amounts of data being collected from both the uO ttawa and Little Rock test sites, a highly organized and efficient database architecture was required to ensure robust and reliable storage as well as quick and efficient data retrieval for analysis. A database using the Microsoft SQL server platform was created to accomplish this. Backups of the data were made regularly to protect the data in the event of a critical system failure.

For the test system at uOttawa, the server accepted all incoming telemetry from the datalogger, the spectroradiometer, and the three network cameras. As seen in Figure 4-24, Campbell Scientific's Loggernet software was used to communicate with, and retrieve, the data stored in the datalogger. The retrieved raw data was saved as a text file on the server. A Labview program developed in-house provided spectroradiometer control and data retrieval. The raw spectra data files were saved as .asd files, binary files whose formatting was specified by ASDi,

the spectroradiometer developer. A Java program was written to transfer the datalogger raw files and spectroradiometer raw files to the database. Furthermore, a Java application was written to log the telemetry from the tracker every second. The telemetry supplied from the tracker included wind speed, calculated and measured orientation of the tracker, and sun sensor data. This application directly inserted the data into the database tables. Finally, a Java script was written to capture the images from the three network cameras on site. The images were not placed in the database. Rather, they were stored as raw jpeg files and organized into a file tree for easy access.

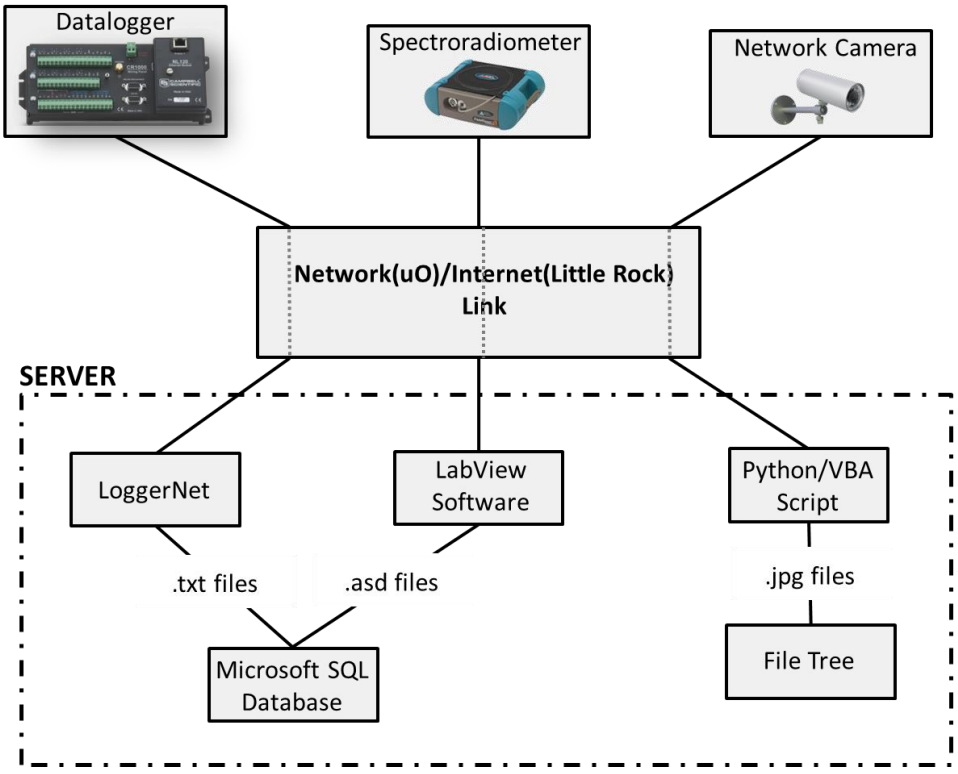

Figure 4-24: Data retrieval and storage network. Data is passed to the server from the datalogger, spectroradiometer, and cameras via an internet link.

For the most part, the telemetry and method of storage for the Little Rock test system was similar to the uOttawa test system, but with several notable differences. First, tracker data was not directly available. This meant that the tracker's recorded data files, which included the sun sensor data and tracking orientation data, had to be obtained directly from Morgan Solar. Furthermore, communication between the uOttawa server and the Little Rock equipment was bandwidth limited, as mentioned above. Consequently, the datalogger was equipped with a 2 GB compact flash memory card and the cameras were supplied with 2 GB SD flash cards. The datalogger and cameras stored the measured data to onboard memory and then dumped the data to uOttawa during the night.

4.3.1 Database Layout

The Microsoft SQL server platform was chosen since it offered a client/server database solution. Despite having a small number of database users, the client/server approach was favoured because it was more reliable than the file-server approach (e.g., MS Access) [44]. In particular, the client/server approach was much less susceptible to database corruption, which ensured that our data was better protected. Furthermore, the database was structured as four non-relational data tables. As summarized in Table 4-2, the first data table contained the panel level electrical measurements, the DNI, the GHI, and the ambient temperature at the uOttawa test site. The second table contained the individual optic *I-V* measurements, the DNI, and the ambient temperature measurements taken at the beginning of each of the individual optic IV measurements. The third table was used to store all calibrated spectral measurements. Finally, the fourth table stored the tracker data, which included wind speed measurements, sun sensor data, and the tracking orientation data. Though all these tables shared the Timestamp column, this database could not be considered relational under the widely used relational model since our database structure was not fully atomic [14]. However, the database was structured such that each table contained a specific class or type of data. This meant that creating queries and extracting data was simple and straightforward for subsequent data analysis.

Table	Columns
Table 1	• Timestamp • DNI • GHI • Ambient Temperature • Panel level Voltages • Panel level Currents
Table 2	• Timestamp • I/O IV Curve Measurements • DNI at the beginning of IV measurement • Ambient Temperature
Table 3	• Timestamp • Calibrated spectra measurement
Table 4	• Timestamp • Wind speed • Sun Sensor Data • Tracking Orientation Data

Table 4-2: Database table contents.

4.3.2 APECS Website and Remote Data Access

To provide project datasets to interested members of the general public, and to enable access of test site data to APECS project members, an APECS project website was developed. The website, located at *www.apecs.site.uottawa.ca,* provided a project description and live images of the test site updated every two minutes. As shown in Figure 4-25, the website also featured a

password protected data return form so that all test site data could be accessed remotely. This allowed the status of the test site to be monitored remotely and permitted data analysis to be done by members of the project who did not have direct access to the database on the SUNLab server. The website was developed in .php on an APACHE webserver by COOP students Graeme Jamieson and Bhavan Tehara.

Figure 4-25: Website data return form.

5 Data Analysis

5.1 Overview

With the test and measurement systems installed and the data acquisition infrastructure in place, it was then possible to evaluate the system performance as well as to identify system flaws and areas for improvement. From the extensive data collected, it was possible to analyze many system inputs – from meteorological characteristics to the idiosyncrasies of the semiconductor material. For this thesis, the focus was on the basic response of the system. Particularly, since the MSI technology was then in a development stage, it was instructive to analyze its performance and to determine the specific causes of performance issues. Likewise, the tracking system and its interaction with the panels and test equipment was important to understand so that future activities could avoid present problems.

System performance depends on many inputs and system properties, as noted in Chapter 2. The effect of these parameters must be quantified to further advance technological development. Specifically, the aspects of a CPV system that must be considered in a complete performance analysis include:

- DNI and the corresponding solar spectrum reaching the solar cell – these are affected by the local meteorological conditions and the concentration ratio and optical transfer function of the optical train;
- Optical alignment and tracking accuracy – these parameters are affected by the quality of the design and construction of the CPV panels and the trackers;
- Cell Temperature – this is primarily controlled by the overall thermal resistance of the heat sinking system, wind direction, and wind speed;
- Cell characteristics – the cell's EQE, series and shunt resistances, fill factor, temperature coefficients, and the resultant *I-V* curve, which is also affected by the above parameters.

This chapter explores the basic performance of the MSI individual optics and panels, and identifies performance trends and some notable peculiarities. The sources (or most plausible sources) of particular trends are identified based on the aspects identified above. Finally, the heat sinking capability of the MSI system is estimated by correlating numerical modelling results with measured data.

5.2 Long Term Degradation

There were nine individually-addressable optics installed on tracker 1, in addition to the six panels. These nine optics provided a representative sample of the optics that made up the panels, which could not be individually measured. Their *I-V* curves were measured every two minutes so that system reliability issues and failure mechanisms could be identified from the long-term performance data.

The maximum power P_{mp} of any solar module may vary appreciably over the course of a day, and from day to day. This is shown in Figure 5-1, where the maximum power of a MSI individual optic is plotted against the voltage at the maximum power point V_{mp} for a random selection of times during 15 days in June 2012. For convenience, the powers have been normalized to the maximum power in the dataset. The vertical variations in P_{mp} are primarily caused by changes in the DNI, and to a lesser degree by variations in solar spectra and cell temperature. The horizontal variations in V_{mp} are primarily the result of differences in cell temperature although changes in the DNI also contribute, but to a lesser extent. Cell electrical properties, such as series or shunt resistances, can also affect changes in the horizontal and vertical spread over time. The effect of each factor must be isolated from the others so that their system influence can be understood. With this, a reference measurement condition can then be established so that equitable comparisons can be made. That is, *I-V* curves measured under any conditions can be corrected to a reference condition. Ideally, all *I-V* curves corrected to the reference should be identical if the cell performance has not changed and all parameters affecting PV performance have been exactly determined.

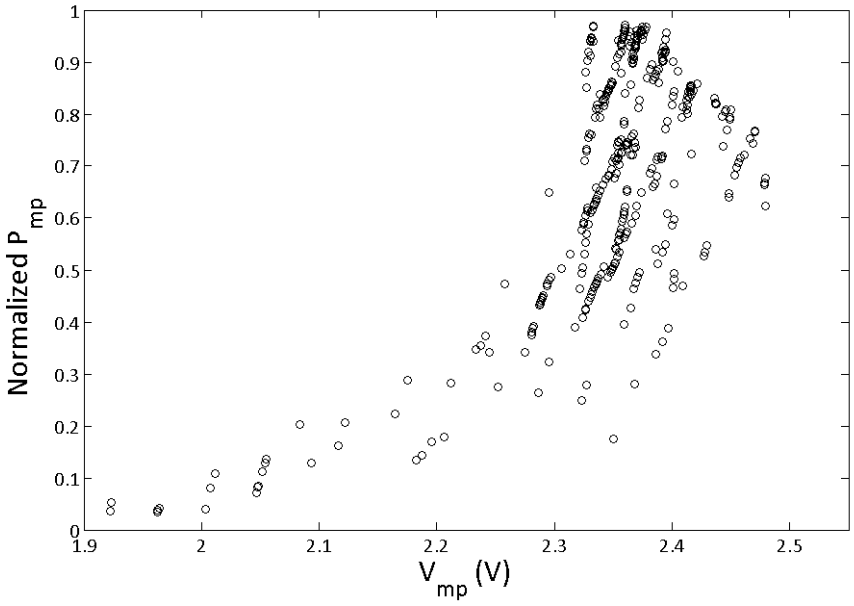

Figure 5-1: Measured P_{mp} scatter plot from over 500 *I-V* measurements of an individual optic taken over the course of June 1st to June 15th of 2012. IV Measurements with DNI < 50 W/m^2 were omitted.

There are several approaches to correct measured *I-V* curves to reference conditions. One is to develop a comprehensive PV system model as is done by Sandia National Laboratories [46]. The Sandia model is a robust and detailed PV system model that enables a system owner to develop complete knowledge of a PV system's behavior through *I-V* measurements, limited solar resource information, and empirical fitting. This allows a system owner to monitor actual versus predicted performance, diagnose system issues, and advance PV system design and sizing. This model does allow the correction of *I-V* measurements to reference conditions. This required

knowledge of cell temperature coefficients, optical alignment errors, wind speed and wind direction; significant regression analyses must be carried out to determine many of the system coefficients. This approach is overly detailed for a preliminary assessment of cell-optic assembly performance, since any significant performance degradation of the early-generation MSI optics meant that these system coefficients were likely to change rapidly over short periods of time. Instead, certain standard PV performance measurement procedures and requirements laid out by the International Electrotechnical Commission (IEC) were used.

5.2.1 IEC 60891 I-V Curve Correction

The IEC 60891 standard (Procedures for Temperature and Irradiance Corrections to Measured *I-V* Characteristics) outlines three methods to correct *I-V* measurements to a reference condition. Two of these three methods require that correction parameters be known for the device under test, such as its temperature coefficients, internal series resistances, and curve correction factors related to temperature dependencies of the internal series resistance. These methods were not used for the same reasons that the Sandia PV model was avoided. Instead, *Correction Procedure 3* of the IEC 60891 standard was used to correct the measured *I-V* curves. This correction procedure is an interpolation/extrapolation method that does not require any correction parameters as inputs. The method is an extension of the bilinear interpolation method with details described in [49,50]. It can address any desired irradiance and temperature condition. The only requirement is that a minimum of three *I-V* curves be measured at known irradiance and temperature, ideally spanning a range of temperatures and irradiances that include the desired reference condition [45]. The *I-V* curve at the desired reference can then be interpolated or extrapolated.

The IEC correction procedure is based upon the linear interpolation or extrapolation of two measured *I-V* curves. With two measured curves, the data can be adjusted to either the desired irradiance or temperature, but not both. Once done, a third *I-V* measurement can be included to correct the first adjustment for the previously neglected factor. The basic element, or building block, of this correction technique is the interpolation/extrapolation using two known *I-V* curves by applying the equations

$$V_3 = V_1 + a(V_2 - V_1) \tag{5.1}$$

$$I_3 = I_1 + a(I_2 - I_1), \tag{5.2}$$

where V_1 and I_1 are the points on the *I-V* curve at irradiance G_1 and temperature T_1; V_2 and I_2 are the points on the *I-V* curve at irradiance G_2 and temperature T_2; V_3 and I_3 are corresponding points on the corrected *I-V* curve at irradiance G_3 and temperature T_3; and a is an interpolation constant related to the irradiance and temperature such that

$$G_3 = G_1 + a(G_2 - G_1) \tag{5.3}$$

$$T_3 = T_1 + a(T_2 - T_1). \tag{5.4}$$

As illustrated in Figure 5-2a, the interpolation with only two *I-V* curves has one degree freedom controlled by a. That is, the range of values for G_3 and T_3 that can be used to

interpolate/extrapolate to the corrected *I-V* curve lies along a line that intersects points (G_1, T_1) and (G_2, T_2). Thus, G_3 and T_3 cannot be selected independently. That is, if G_3 is selected then T_3 is determined by the point along the line that has irradiance coordinate G_3 or vice versa.

Correcting the *I-V* curve to any irradiance values can then be done by combining the procedures for two known *I-V* measurements. With a third *I-V* measurement, the irradiance and temperature values now have two degrees of freedom so the curve can be adjusted to any set of irradiance and temperature values. This is shown in Figure 5-2b, where the values subscripted with *a, b, or c* refer to the reference *I-V* characteristics The procedure to correct to the desired reference condition (G_n, T_n) is as follows:

1) The *I-V* curve at conditions (G_m, T_m) is calculated from (G_a, T_a) and (G_b, T_b)
2) The *I-V* curve at conditions (G_n, T_n) is calculated from (G_m, T_m) and (G_c, T_c)

Each of these corrections uses equations (5.1)-(5.4) to perform the I-V correction. However, this requires that the interpolation coefficients and the values of Gm and Tm be determined before calculating any corrected curve. This can be done by solving the following equations:

$$G_m = G_a + a_1(G_b - G_a) \tag{5.5}$$

$$T_m = T_a + a_1(T_b - T_a) \tag{5.6}$$

$$G_n = G_m + a_2(G_c - G_m) \tag{5.7}$$

$$T_n = T_m + a_2(T_c - T_m). \tag{5.8}$$

Here there are four unknowns (Gm, Tm, a1, a2) and four equations, thus, a system solver can be used to determine their required values for the desired reference irradiance and temperature (Gn, Tn) of the corrected I-V curve. Figure 5-3 shows an example of the corrected I-V curve using the procedure of Figure 5-2a.

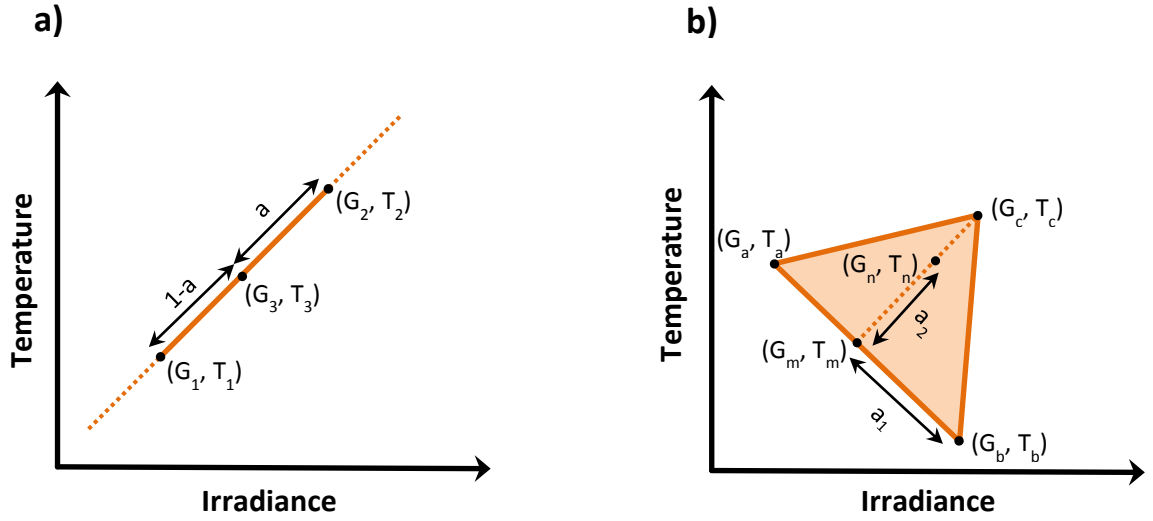

Figure 5-2: a) Correction with two measured IV curves can only be set by one of temperature or irradiance. B) Correction with three or more measured IV curves allows one to correct to any desired temperature and irradiance condition.

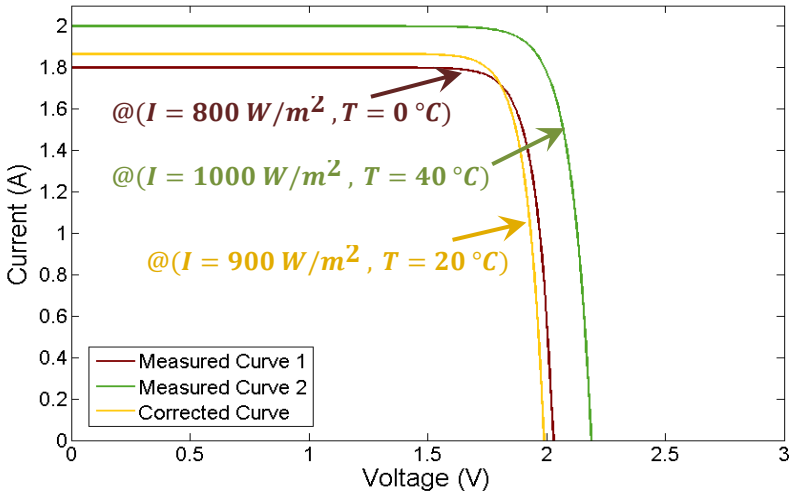

Figure 5-3: Producing a corrected *I-V* curve from measured curves using the procedure of Figure 5-2a.

The correction procedure was implemented in MATLAB to generate a single corrected *I-V* curve for each day. The performance of the individual optics could then be assessed over time for fixed irradiance and temperature. The reference condition was chosen to be concentrator standard operating conditions (CSOC), which are an irradiance of 900 W/m^2 and a cell temperature of 20 °C [47,56].

To evaluate the performance of the individual optics, several characteristics were calculated from the corrected *I-V* curve. These were the fill factor, the short circuit current, the open circuit voltage, the maximum power point voltage normalized to the open circuit voltage (V_{mp}/V_{oc}) , and the maximum power point current normalized to the short circuit current (I_{mp}/I_{sc}). The trends and changes in these parameters provided the evidence to help identify degradation mechanisms. For example, significant changes in V_{mp}/V_{oc} and I_{mp}/I_{sc} point to cell degradation, but changes in I_{sc} with the other parameters relatively stable suggest that there may be issues with the concentrating optics. Based on the calculated parameters, a brief qualitative analysis of the performance of each individual cell-optic assembly is given below. There were noticeable variations in I_{sc} over time for some of the individual cell-optic assemblies. Though it is possible that soiling of the optic contributed to this variability, it will be shown that it was primarily the result of optical misalignment as is substantiated by systematic and consistent observations. This optical misalignment will be discussed in detail subsequent to the individual optic analysis. When present, this observation will only be noted in the following individual optic analysis. Moreover, the purpose of the correction was to account for variations in environmental conditions such that the corrected IV curves were corrected to a single reference condition. This allowed for equitable comparisons and would otherwise give a meaningless or anecdotal results. To accurately apply the curve correction, stringent conditions were placed on the IV curve selection to limit extrapolation and ensure that the corrected IV curves would give accurate results. Specifically, corrected curves that were obtained large extrapolation values were omitted. This resulted in gaps in the data, particularly in the winter months, as a consequence of the

predominant low DNI and limited ranges of DNI observed in these months. Thus, unreliable corrected curves were filtered out of the analysis.

5.2.2 Individual Optic Analysis

Individual Optic 1

As seen in Figure 5-5, individual optic 1 performed relatively well over the measurement period, as evident by its stable fill factor (around 0.8), and V_{mp}/V_{oc} and I_{mp}/I_{sc} ratios. However, there are long term fluctuations in I_{sc} over time, which suggests that the irradiance on the cell is on this timescale. Otherwise, this optic had relatively stable performance and did not show any signs of degradation or failures through its life. Figure 5-5 shows neither observable water ingress nor any other noticeable issue with the optic.

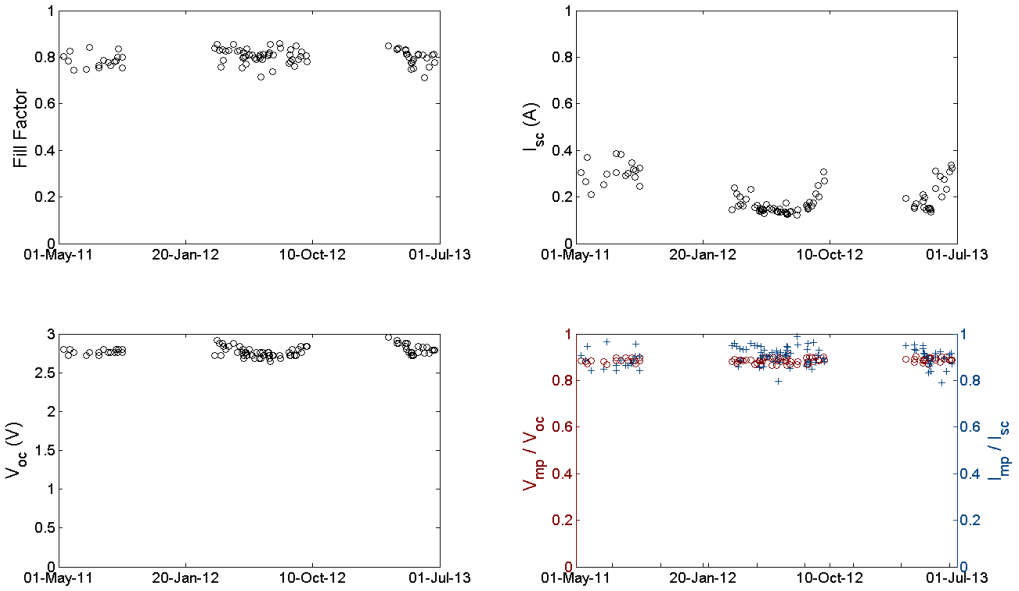

Figure 5-4: IEC correction results for individual optic 1.

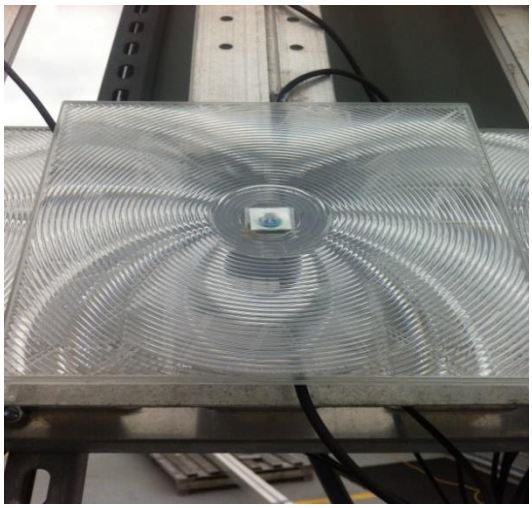

Figure 5-5: Individual optic 1 – no evidence of water ingress or other abnormalities.

Individual Optic 2

Individual optic 2 proved to have one of the most interesting behavior profiles of all analyzed optics. As seen in Figure 5-6, the behavior of the optic was relatively stable from May 2011 up until the beginning of 2012. However, on March 18, 2012 sudden cell degradation was observed. In Figure 5-7 (top panel), the degradation in the *I-V* curve is shown throughout March 18, with one final curve on the following day; the current has been normalized by the DNI to maintain a common reference, and the timestamps for the characteristics are shown in the bottom panel. The cell initially has the expected characteristic for a good cell as depicted by the dark red and orange curves. Near 1 PM, a noticeable deterioration in the cell's shunt resistance suddenly occurs (green curve). The shunt resistance continues to drop (blue curve, 2 PM) reaching a very low value by the morning of the next day (purple curve).

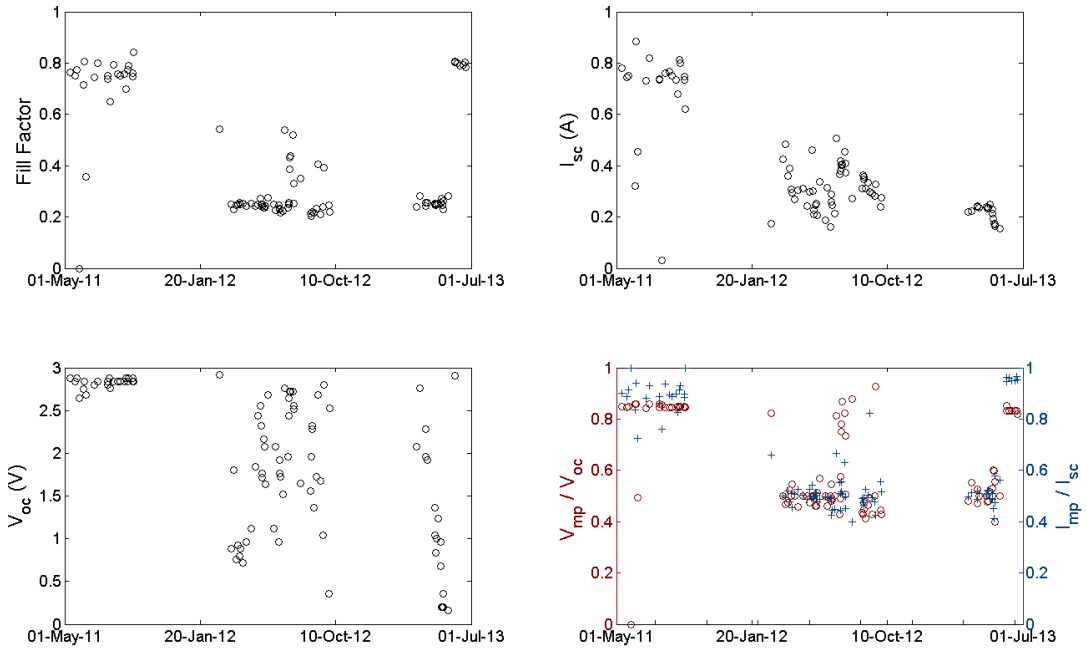

Figure 5-6: IEC correction results for individual optic 2

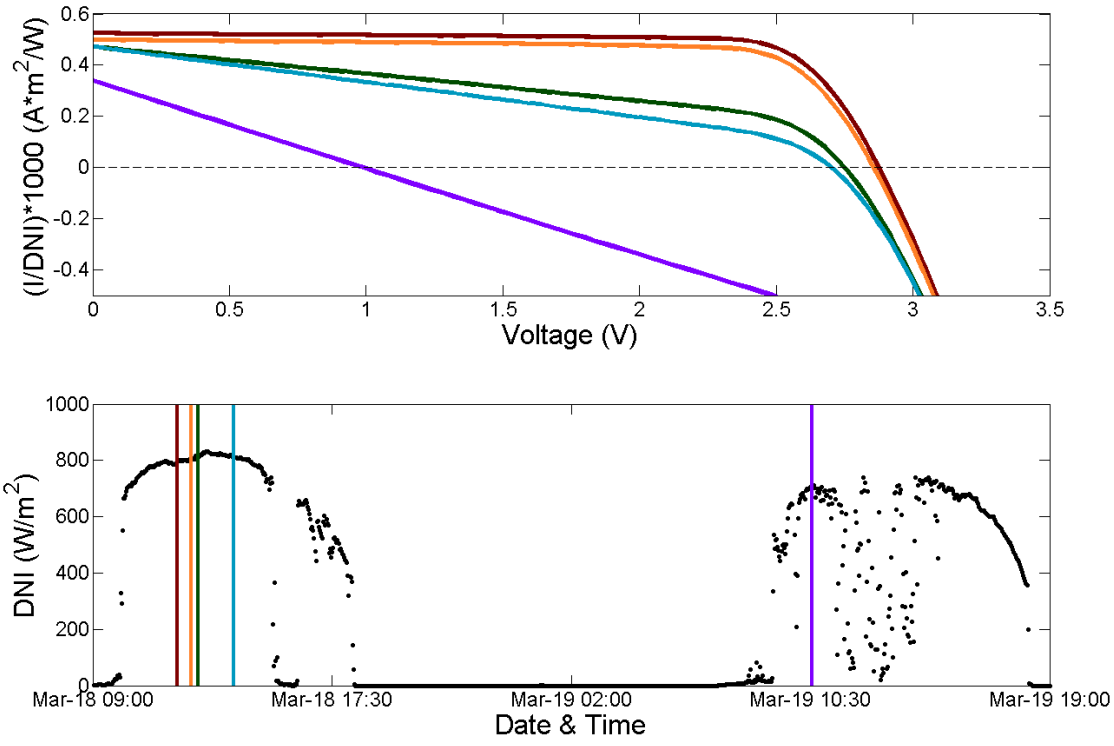

Figure 5-7: IV curve degradation of individual optic 2 over March 18th, 2012 and March 19th, 2012.

Though optic 2 was not disassembled, it was determined that shunt resistance degradation was most likely due to water ingress, as shown in Figure 5-8. It was determined through visual inspection that water entered the optic through breaks in the laser-welded seal of the optic. These breaks were likely caused by thermal stresses. Transient temperature changes caused by passing clouds may have resulted in rapid air pressure changes inside the hermetically sealed optic, stressing the optic seal. Variations in ambient temperature may have also caused the optic to flex with time, further contributing to stress on the seal until failure.

Water inside the optic may have reduced the shunt resistance in two ways. If sufficient water had entered the carrier, it may have provided an additional electrical path from anode to cathode, as it is likely that the water contained sufficient exogenous ions to make it reasonably conductive. However, such a mechanism is not generally consistent with the observed smooth onset to failure, since stress fractures are catastrophic events – the subsequent ingress of moisture over time would arguably lead to transient events (if the accumulation of moisture were slow) or sudden onset changes (if the accumulation of moisture were fast). Alternatively, *electromigration*, the movement of metallic material across a non-metal under the influence of an electric field, may been the cause of the shunt resistance degradation [51-52]. Since the CPV cells were bonded to their carriers with solder containing metals such as tin or silver, under the right conditions these metals may have migrated to form a conductive path between the carrier's cathode and anode. The conditions that promote electromigration were known to be present – moisture or high relative humidity, voltage difference between conductors, and narrow (width) spacing between conductors. Electromigration typically proceeds in the following manner [51,52]: first, dissolution or oxidation of the migratory metal at the anode (this requires the presence of water to dissolve the metal ions); then migration of the metal ions across the insulator towards the cathode due to the presence of the electric field; finally reduction or deposition of the metal at the cathode. Typically, the deposition of the migratory metal occurs as dendrites that grow in size until a conductive path is established between anode and cathode. The time to failure could range from minutes to weeks before a conductive path between anode and cathode was established. However, shunt resistance degradation would manifest suddenly when the conductive path was finally established, which agrees with observations. Also, as electromigration continued the dendrites would thicken and the conductivity of the path would increase. This would further degrade the shunt resistance across the cell, which was also observed. Though definitive physical proof of electromigration was not obtained (this would require the cell-optic assembly to be dismantled and the cell perimeter to be microscopically studied), it is plausible that this mechanism was responsible for the degradation of the shunt resistance.

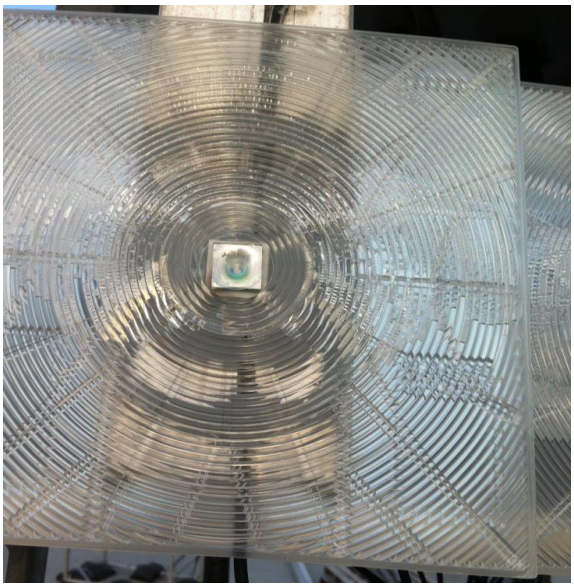

Figure 5-8: Individual optic 2 – significant water ingress.

Individual Optic 3

Individual optic 3 exhibited catastrophic failure at an early time in this study, as seen in Figure 5-9. The initially low I_{sc} implies that the concentrator optic was not properly directing light onto the cell, which may have resulted in the burning and consequent deformation noticed at the centre of the optic, as shown in Figure 5-10 (water ingress was subsequently noticed as well). The charring may have resulted in damage to the secondary optic, altering its light reflective properties, and/or the deformation caused by this charring may have altered the waveguiding properties of the light in such a way that light would no longer impinge upon the cell. With I_{sc} and V_{oc} both falling to zero at the same time, this is consistent with the cell no longer being illuminated. This failure mechanism occurred on many optics, both individual in panels. The cause of the burning failure mechanism was determined by MSI and corrected in later iterations of their manufacturing processes.

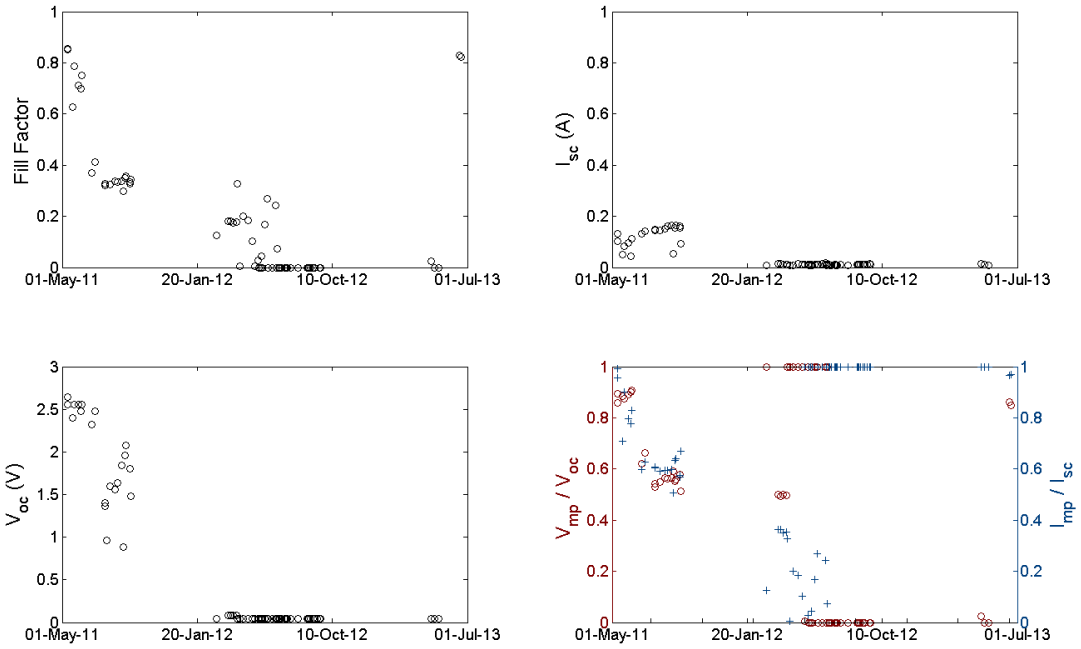

Figure 5-9: IEC correction results for individual optic 3

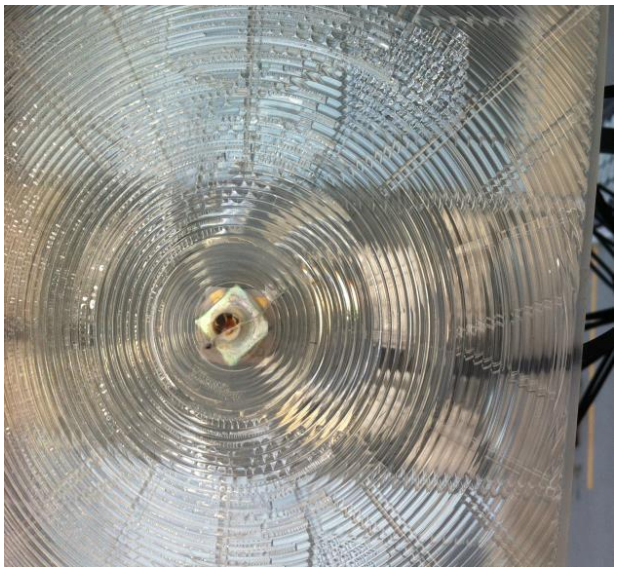

Figure 5-10: Individual optic 3 – significant water ingress and charring of the reflector.

Individual Optic 4

As shown in Figure 5-11, individual optic 4 exhibited a stable fill factor of around 0.8 and relatively constant V_{mp}/V_{oc} and I_{mp}/I_{sc} ratios over the measurement period. There was, however, some evidence of variability in I_{sc}. This suggests that the concentration of light on the cell was

somewhat variable over the course of days or weeks. Despite this, relatively stable performance was shown and there was no evident degradation in any of its corrected parameters. Also, there were no obvious signs of failure or degradation upon physical observation, as noted in Figure 5-12.

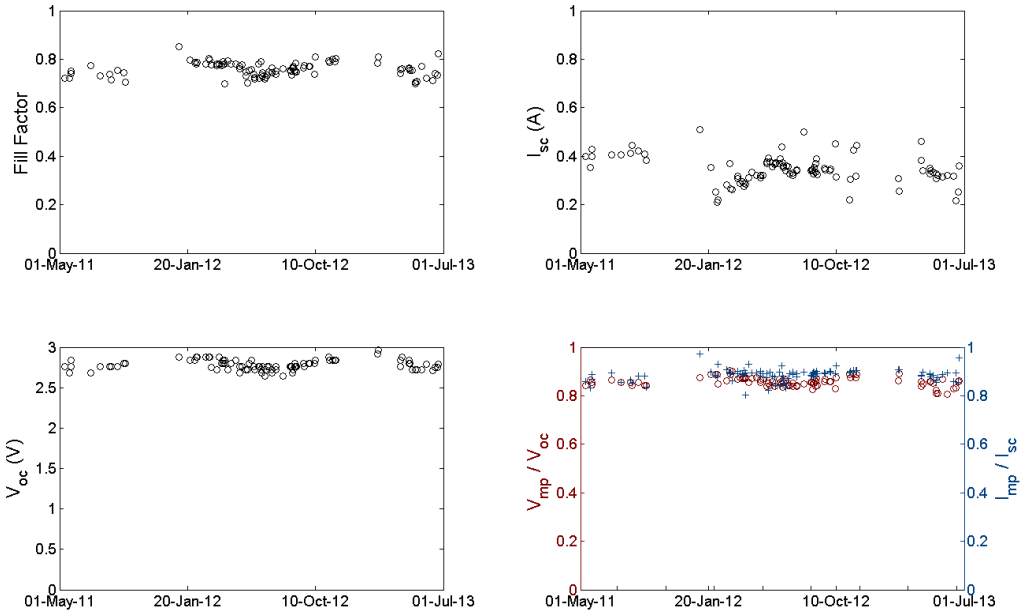

Figure 5-11: IEC correction results for individual optic 4

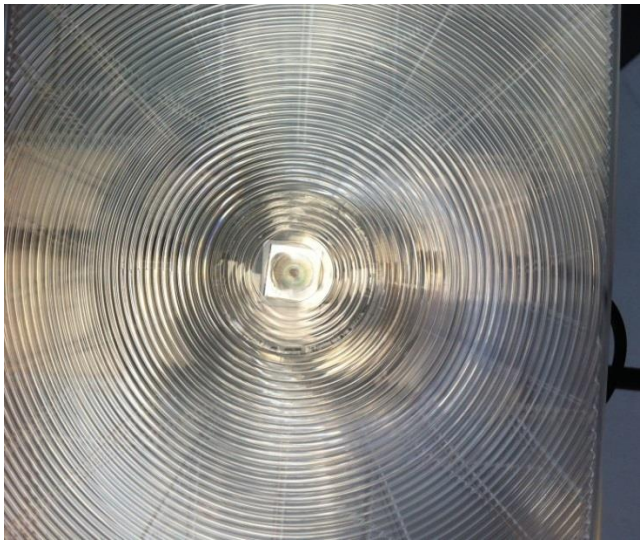

Figure 5-12: Individual optic 4 – no evidence of any abnormalities

Individual Optic 5

As seen in Figure 5-13, the fill factor and V_{oc} of individual optic 5 remained stable over the course of the measurements; no obvious degradation in the shunt or series resistance was observed since I_{mp}/I_{sc} and V_{mp}/V_{oc} also remained constant. Thus, there were no pronounced issues apparent with the cell. Also, there were no signs of burning or water ingress or any other gross abnormality, as supported by Figure 5-14. However, there was significant scatter in I_{sc}, superimposed on a general reduction in the current. This is consistent with an unstable and increasingly compromised ability to reliably couple light onto the cell. One of the factors that could cause this is an optic near its angular acceptance limit. Then I_{sc} would be sensitive to small changes in alignment that could have been brought on by some systematic shift in optic position superimposed on more random variations due to temperature fluctuations or small tracking errors.

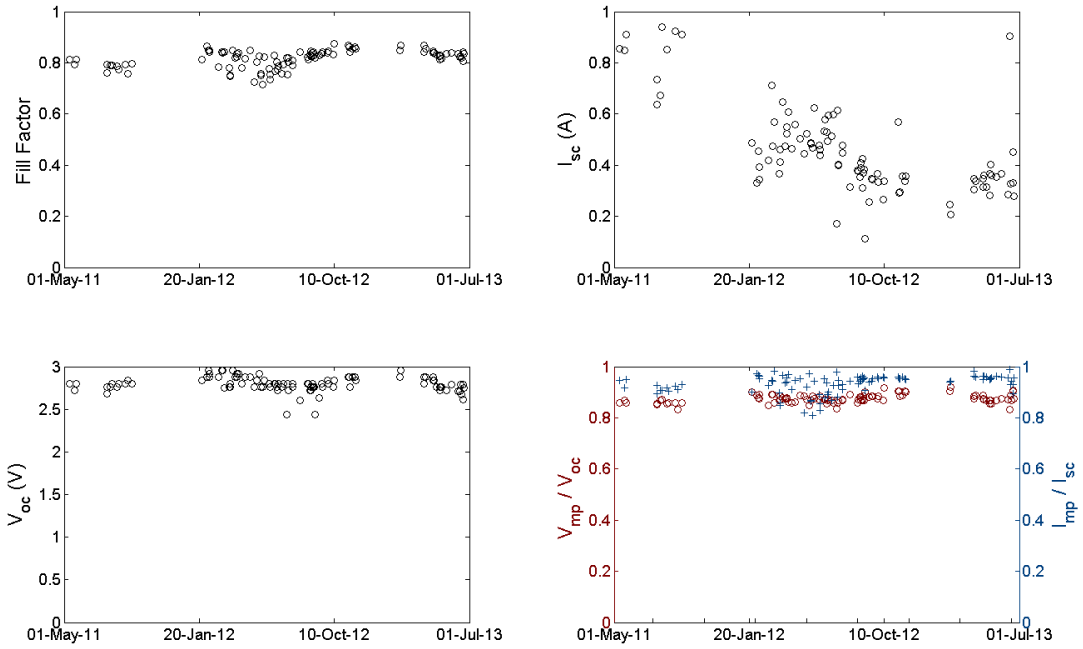

Figure 5-13: IEC correction results for individual optic 5

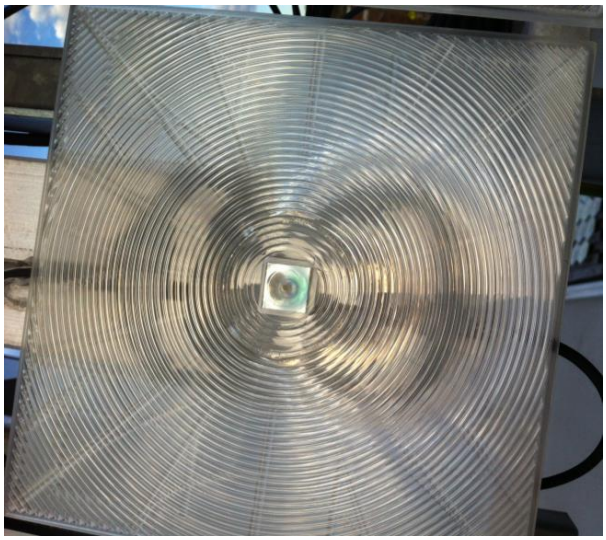

Figure 5-14: Individual optic 5 – slight charring on the reflector.

Individual Optic 6

The performance of all measured parameters of individual optic 6 remained relatively steady over the measurement period, as seen in Figure 5-15. However, the I_{sc} for this optic was very small. This was likely due to inefficient light-guiding and/or coupling arising from manufacturing issues since I_{sc} was small from the beginning. Furthermore, there was no observable water ingress but there was a slight amount of charring or burning apparent on the top of the secondary optic, as shown in Figure 5-16. This onset of this charring occurred well after the optic's installation and had no discernible effect on the optic performance. It is thus probable that the issue was in the coupling of the secondary optic to the cell, and not the light guiding/concentration itself.

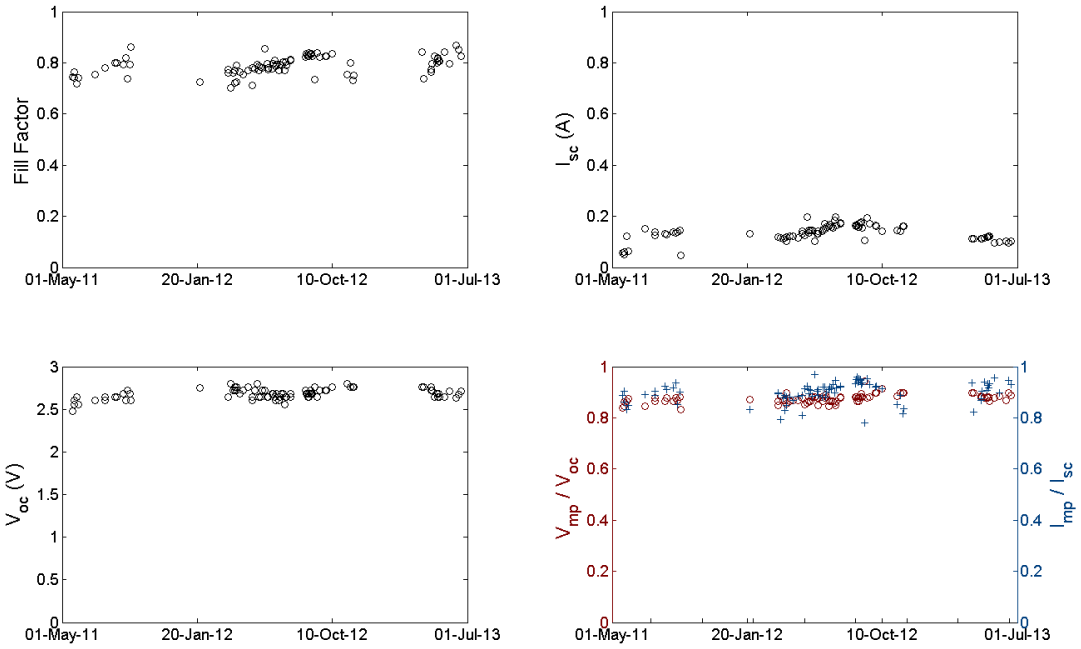

Figure 5-15: IEC correction results for individual optic 6

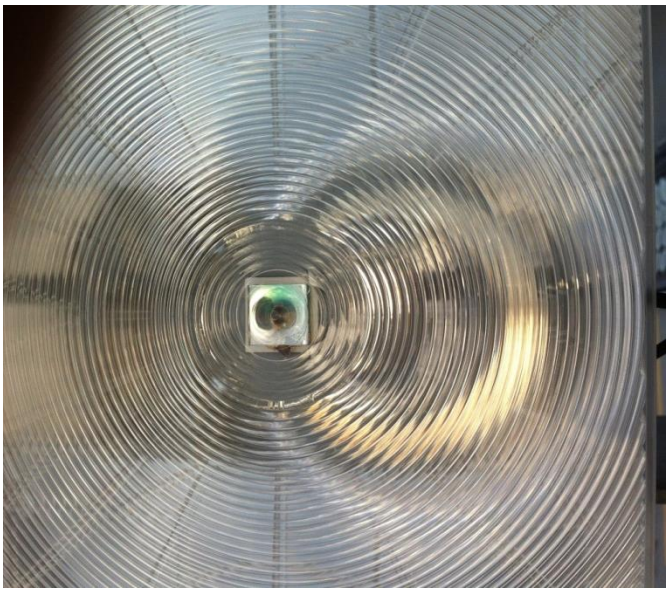

Figure 5-16: Individual optic 6 – some charring evident on the reflector.

Individual Optic 7

As noted in Figure 5-17, the performance of individual optic 7 was quite stable over the measurement period with almost no variation in its parameters, except for a slight decrease in I_{sc} over time. Figure 5-18 did not reveal any notable reliability issues for this optic, neither observable water ingress nor charring of the secondary optic.

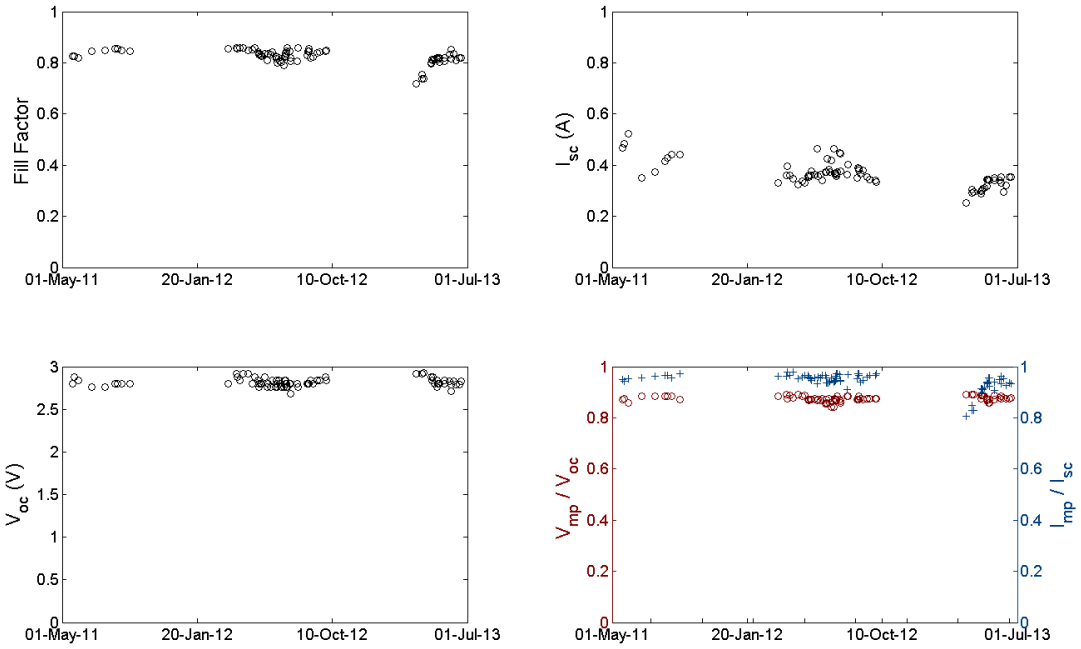

Figure 5-17: IEC correction results for individual optic 7

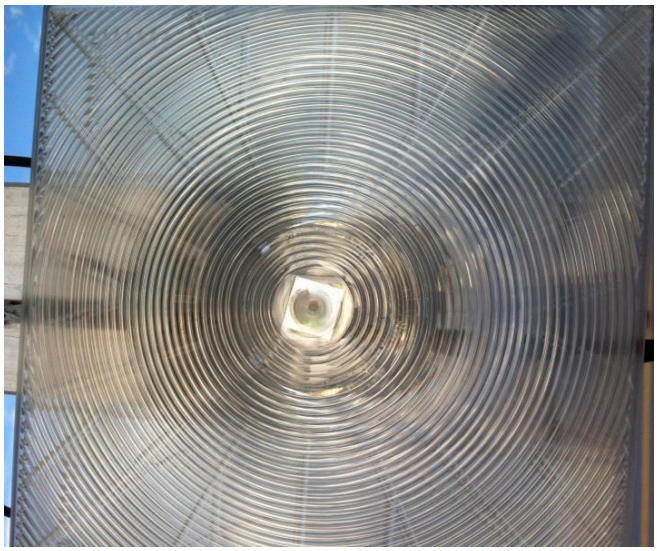

Figure 5-18: Individual optic 7 – no evidence of any abnormalities.

Individual Optic 8

As noted in Figure 5-19, the performance of individual optic 8 was quite stable over the measurement period with almost no variation in its parameters, except for a slight decrease in I_{sc}

over time. Figure 5-20 did not reveal any notable reliability issues for this optic, neither observable water ingress nor charring of the secondary optic.

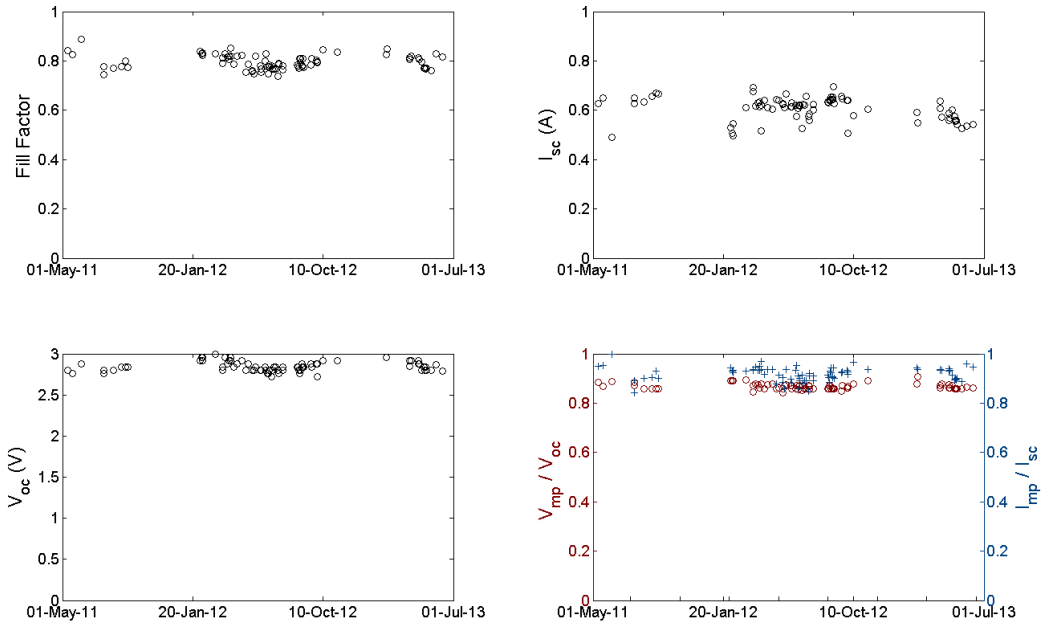

Figure 5-19: IEC correction results for individual optic 8

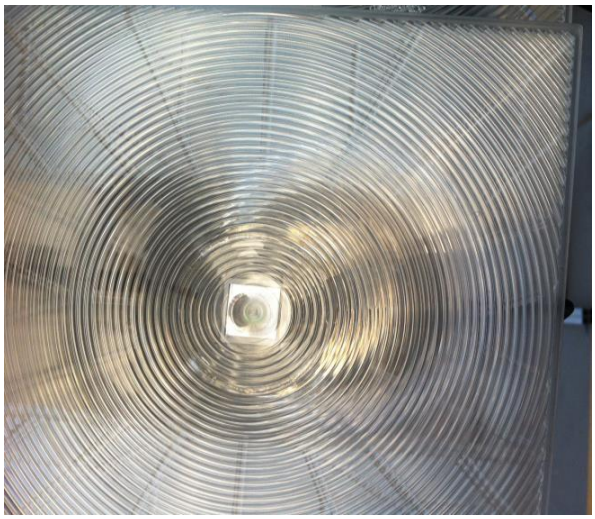

Figure 5-20: Individual optic 8 – no observable abnormalities.

Individual Optic 9

Individual optic 9 exhibited catastrophic failure at the onset of this study, with a general (though scattered) drop in fill factor, I_{sc}, and V_{oc}, as shown in Figure 5-21. The initially low I_{sc} implies that the concentrator optic was not properly directing light onto the cell, and consequent material expansion is thought to have caused the optic to crack at the centre, facilitating water ingress, as

seen in Figure 5-22. The strong scatter in fill factor, V_{mp}/V_{oc} and I_{mp}/I_{sc} data, superimposed on a concomitant strong decline in their trending, implies significant cell degradation likely caused by shorting of the cell, possibly through somewhat transient shunting by the water. Furthermore, as I_{sc} and V_{oc} both fall to zero at the same time, it is clear that the charring of the secondary optic eventually resulted in no illumination on the cell. Similar physical observations were noted for many of the panel optics.

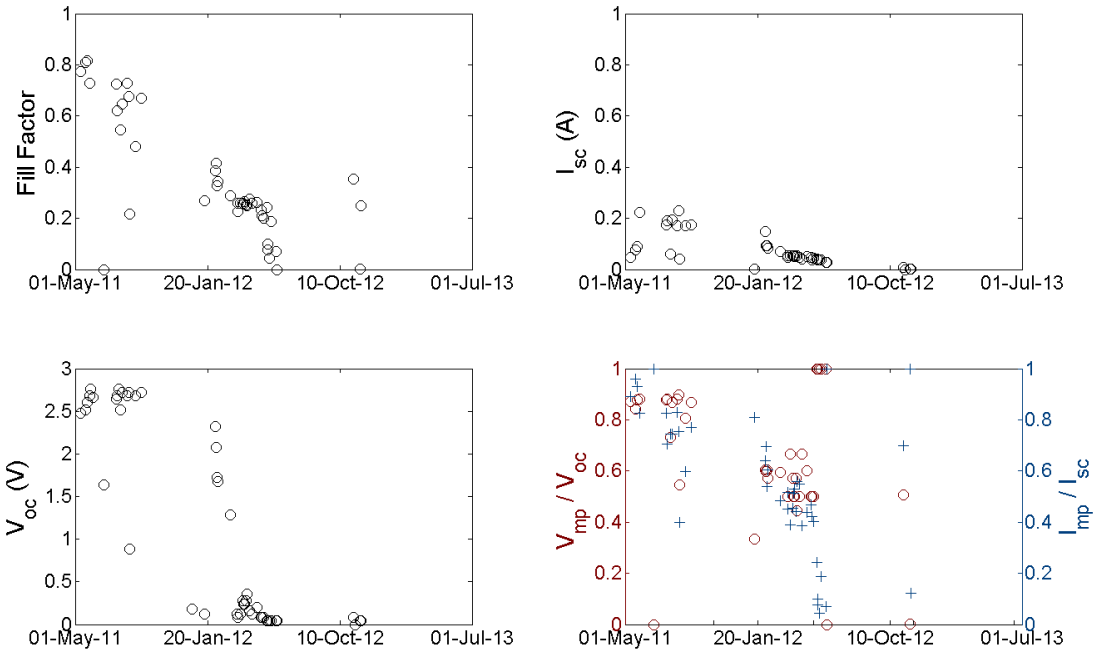

Figure 5-21: IEC correction results for individual optic 9

Figure 5-22: Individual optic 9 – significant water ingress and charring apparent.

5.3 Optic Misalignment

To further evaluate the performance of individual optics, I_{sc} measurements were plotted against their corresponding DNI measurements over the course of a day. Many different days were evaluated and all showed similar results. The plots of I_{sc} against DNI on May 11, 2012, which were representative of the data observed on all other days, are shown in Figure 5-23. The reliability issues associated with optics three, six, and nine (and their very low short circuit currents) precluded their consideration. A hysteresis effect is observed beginning at solar noon in the curves of optics one, two, and four; slight hysteresis in five; and very little to no hysteresis in optics six and seven. Hysteresis was unanticipated since I_{sc} is directly proportional to DNI. While optics six and seven behave as originally expected, the others do not. Possible causes of the hysteresis effect may be associated with changing temperature, spectral shifts over the course of a day, and/or optical alignment and tracking accuracy.

A single diode model was used to examine the effects of cell performance under changing conditions. The model was developed by SUNLab graduate student Mark Yandt [22] based on work in [48]. Herein, a triple junction cell was modelled using the equivalent circuit model portrayed in Figure 2-21b. Using the Varshi equation derived in [53], this model accounts for the bandgap shift – the change in the external quantum efficiency with temperature for each subcell. The concentrating optic's optical transfer function (OTF) was also included in the model, and the photogenerated current for each subcell calculated as

$$I_{ph} = q \int \frac{I(\lambda)}{E_{ph}(\lambda)} * OTF(\lambda) * EQE(\lambda, T)\, d\lambda\,, \tag{5.9}$$

where q is the electron charge, $I(\lambda)$ is the wavelength-dependent irradiance incident on the optic, $OTF(\lambda)$ is the optical transfer function, and $EQE(\lambda,T)$ is the temperature and wavelength dependent external quantum efficiency of the subcell. The *I-V* curve for a single subcell was determined from [15]

$$I = I_{ph} - I_o\left(e^{\frac{q(V+IR_S)}{nkT}} - 1\right) - \left(\frac{V + IR_s}{R_{sh}}\right). \tag{5.10}$$

Since the subcells are series connected, the *I-V* curve of the triple junction device was calculated by summing the voltages of the three resultant *I-V* curves; the current of the device was that of the least current producing subcell, referred to as the limiting subcell. The series and shunt resistance values for each subcell were determined from in-house temperature controlled measurements on isotypes supplied by the manufacturer. Finally, the model was then expanded and modified as required to determine the cause(s) of the observed hysteresis.

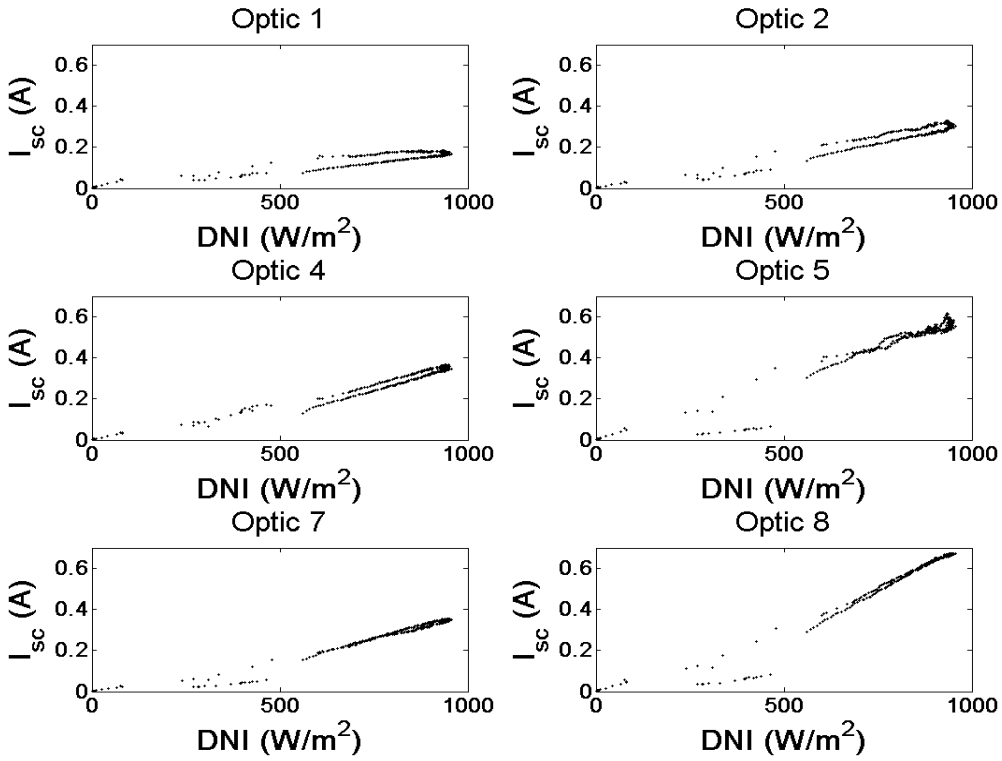

Figure 5-23: Isc vs DNI for six of the individual optics on May 11, 2012. A hysteresis type behavior is observed for most of the optics. Optics 3, 6, and 9 were omitted due to their poor performance.

While I_{sc} rises with an increase in cell temperature, the temperature coefficient of I_{sc} [25] is not large enough to explain the observed changes in I_{sc}. In Figure 5-23, the high part of the I_{sc} vs DNI curve occurred in the morning and the lower portion in the afternoon. Since ambient temperature is typically higher in the afternoon than in the morning, as was the case on May 11, 2012, this also militates against temperature as the cause of the hysteresis.

Spectral shifting – changes in the spectral irradiance incident on the cell – may be caused by systematic changes in local atmospheric conditions and air mass values. They may also arise from thermally-induced deformations in the optic. The deformations could lead to unwanted reflections, absorption, or refractive effects thus affecting the spectral irradiance on the cell. Shifting may induce a systematic change in which subcell limits the current, thus causing the current to evolve differently with DNI. To examine this hypothesis, spectra input into the model were biased over the course of a day to shift between top subcell limiting and middle subcell limiting. Since the bottom subcell overproduces in comparison to the middle and top subcell, bottom subcell limiting was never considered. I_{sc} vs DNI curves were then plotted to determine if it was possible to reproduce the hysteresis, and if so, to ascertain the conditions needed to reproduce the observed results.

In modelling the effect of varying spectra, the MSI optical transfer function (provided by MSI) was included into the model. Measured DNI and spectra were used as inputs to the model. Generated SMARTS2 spectra with integrated irradiance equal to the measured DNI were also included as an alternate input to the model. The mechanism used to control the limiting subcell and limiting currents were three Gaussian filters with sufficiently narrow bandwidths and centre wavelengths position such that each filter could be used to control the photogenerated current of its respective subcell. The approach most representative of atmospheric effects and AM changes was to make gradual changes in spectral content and so gradually transition. From this modelling, it was found that gradual variations in spectra produced a change in slope of the I_{sc} vs DNI if the limiting subcell changed from top to middle or vice versa. However, it did not produce hysteresis.

The deformation hypothesis considered a marked abrupt change in the spectral content incident on the cell, characteristic of abrupt changes in the optical transfer function of the optic due to physical changes caused by thermal stresses. For example, flexion of the light guiding layer might induce additional absorption or refraction within the optic by guiding light through parts of the optic that were never intended for the light to pass through. An abrupt change in spectra could produce in a sudden drop in total cell current, which produced the hysteresis illustrated in Figure 5-24. This abrupt change was modelled with the single diode model by abruptly changing the filtering of the incoming spectra at solar noon in such a way that the cell would suddenly shift from top sub-cell limiting to middle-cell limiting. Additionally, the magnitude of filtering required in the narrow band of a sub-cell's spectral regime to produce the hysteresis behavior was very large and very unlikely to occur in practice. Despite qualitative similarity to the measured optic behaviour, no physical justification for systematic and predictable deformation was found. This hypothesis likewise fails.

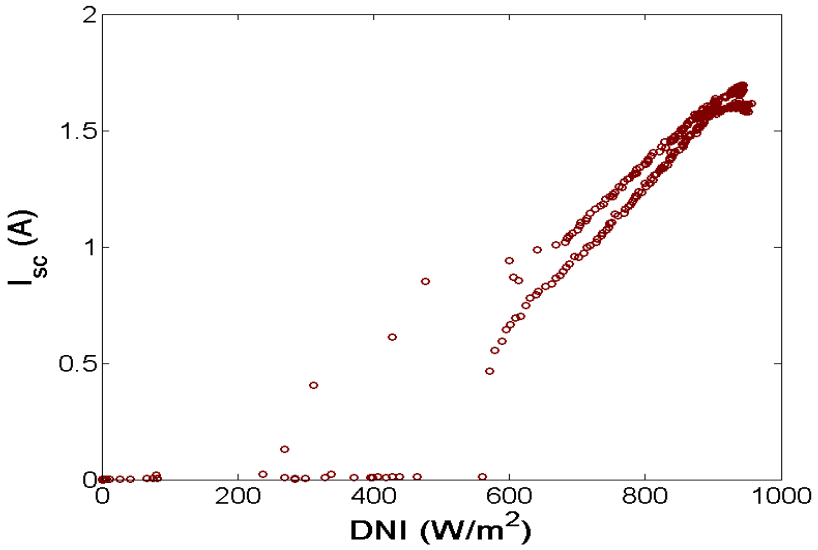

Figure 5-24: Modelled I_{sc} vs DNI with subcell filters included such that the cell went from top cell limiting in the morning to middle cell limiting in the afternoon.

Tracking accuracy and misalignment were next considered. As stated in chapter four, the pyrheliometer possessed an acceptance angle of approximately 2.9°. MSI optics had a smaller angular acceptance angle of 1° and are thus more sensitive to tracking inaccuracies than the pyrheliometer. Likewise, the specifications of the GoldenSun tracker stated that the trackers had a tracking accuracy within 0.1° to 0.2°. The data collected were used to look at many aspects of the tracking system. It was determined that the tracking elevation motor controls were programmed such that the tracker was always leading slightly in front of the sun. Consequently, the tracking alignment in elevation was changed at solar noon every day. This was the most likely explanation of the hysteresis effect. The following will describe the analysis that lead to this conclusion.

The Golden Sun tracker was equipped with a sun sensor to facilitate its fine (closed-loop) tracking. The sensor was made up four photodiodes separated by dividers, as illustrated in Figure 5-25. Reducing the difference between the north (N) and south (S) photodiodes to zero was used to make tracking corrections in elevation. Similarly, the difference between the west (W) and east (E) photodiodes was used to correct the tracker's position in azimuth. Examining the differences between the W and E photodiodes showed that the differences were minimized and providing expected behavior. However, as shown in Figure 5-27 the N photodiode was slightly more illuminated than the S photodiode before solar noon whereas the S photodiode is slightly more illuminated than the N photodiode after solar noon. These photodiode measurements were retrieved from the tracker control hardware. Unfortunately, no units were associated with the measured values. Thus, determining the approximate tracking error induced by the leading of the elevation controls needed to be estimated to determine if this leading behavior was worth consideration.

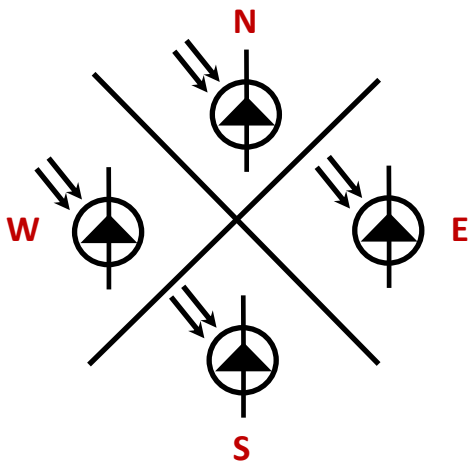

Figure 5-25: Layout of sun sensor on GoldenSun trackers. Four photodiodes were separated into quadrants by a divider.

The tracker-mounted network camera facing the sun was used to estimate the alignment error induced by the leading behavior. The sun was tracked within the camera's viewing window to determine if the sun's position shifted over the course of a day. Accomplishing this required the application of image processing techniques to the pictures taken at two minute intervals. As illustrated in Figure 5-26, these steps consisted first of cropping the image and converting it to grayscale. The grayscale image was then converted to a binary image using a threshold value of 0.65. An object-finding approach using the MATLAB *bwlabel* function was then applied, with a center of mass calculation used to find the coordinates of the sun center. A one-pixel shift in the position of the sun's center (and any point on the sun's disk) corresponded to 0.073°. Figure 5-27 compares the results of the analyzed images (bottom panel) with the sun sensor data (top panel). The tracker camera data reveal a 0.2° shift across solar noon, in agreement with, and quantifying, the sun sensor results. Note that this shift, though systematic, was still within the tracker specifications.

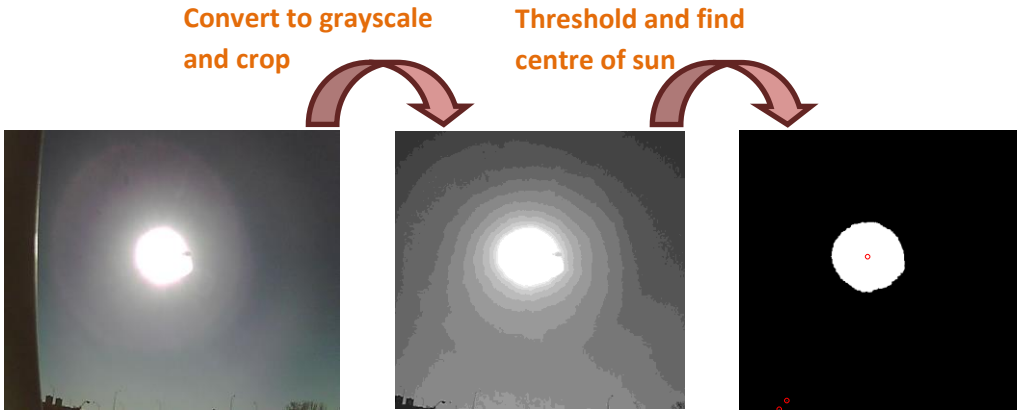

Figure 5-26: Image processing technique used to track the suns' relative position on tracker. The process consisted of converting the image to grayscale and cropping out the edges. The image was then given a threshold to convert to black and white. An object finding algorithm was then applied to find the center of the sun.

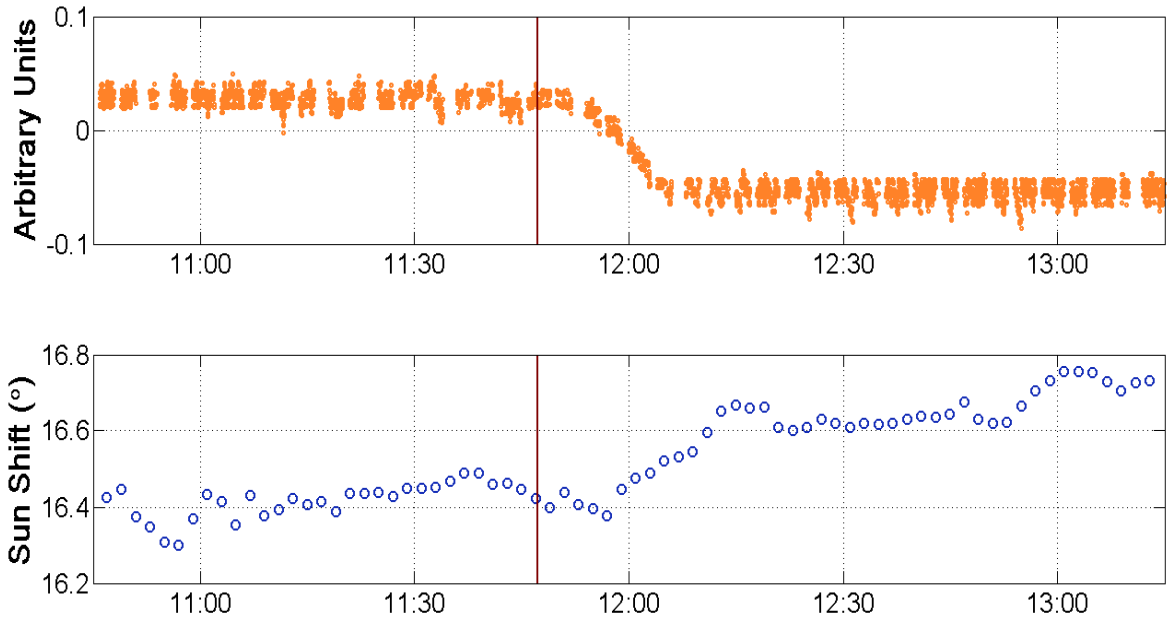

Figure 5-27: Comparing sun sensor readings to suns' position as measured by the image processing of the pictures taken by the on-tracker camera.

Given that the tracking alignment shifted by as much as 0.2° across solar noon, it was likely that the hysteresis resulted from misaligned optics becoming further misaligned. To test this, the angular acceptance of the optic was included in the single-diode model to study the impact of misalignment. An angular acceptance profile based on the MSI angular acceptance of the optic, and work done elsewhere [54], is shown within the inset of Figure 5-28. This angular acceptance profile assumed an angular acceptance of 1° and was constructed with an order six polynomial. The resulting plot of I_{sc} vs DNI shown in Figure 5-28 was based on a misalignment of 0.7° in the morning with a further 0.15° misalignment added immediately after solar noon. Comparison of these results with those found for optic four, reproduced in Figure 5-29, show good qualitative agreement, clearly demonstrating that the observed hysteresis behavior coincides with the change in tracking alignment across solar noon.

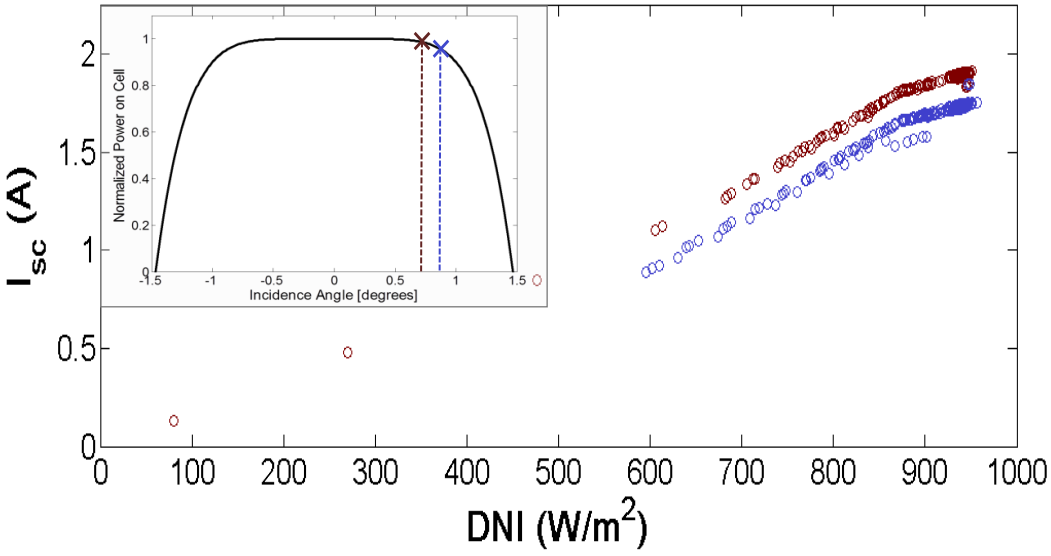

Figure 5-28: Resultant I_{sc} vs DNI characteristic with optic misalignment changed from 0.7º to 0.85º at solar noon. This demonstrates that the observed hysteresis is likely caused by both a tracker misalignment issue as well as an optical misalignment issue.

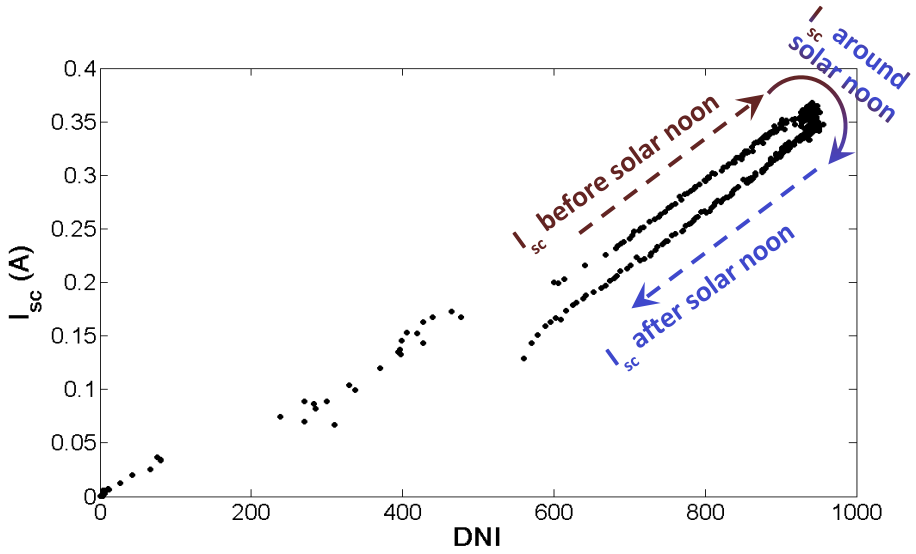

Figure 5-29: Measured I_{sc} vs DNI characteristic on May 11th, 2012. The hysteresis effect is clearly observed where the I_{sc} values where higher in the morning than they were in the afternoon. A transition to from these higher to lower values occurs at solar noon, which is consistent with the observed tracker behavior.

5.4 Estimating the system convective heat transfer coefficient

In Chapter 3, the cooling power (the thermal resistance of the CPV cell-optic-on-carrier assembly) was lumped into a single parameter, the convective heat transfer coefficient, *h*, through the bottom surface of the carrier. The value of this parameter is system specific, as it depends on the nature of the thermal bonding between cell, carrier, and heat sink; the nature of the heat sink used; and on the system environment. This is precisely why no filtering of the

measured data was done in this analysis as variations in DNI, temperature, and other environmental variables needed to be encapsulated in the analysis. Thus, accurately estimating the *h* parameter is instrumental in developing an accurate thermal model for an installed CPV system. Using the results of the thermal model with the measured *I-V* curve data of the individual optics facilitated the estimation of the *h* value for the MSI Gen II optics. Specifically, estimating the *h* parameter began by simulating the dependence of the average cell temperature on concentration for a range of *h* values. Next, the cell temperatures were calculated from the *I-V* curves measured throughout the course of a day, giving experimental data for the dependence of average cell temperature on concentration. Finally, the measured result was compared with the results in the simulated dataset to determine the *h* parameter.

A thermal model of the cell-on-carrier for the Gen II optics was developed, similar but not the same as that described in Chapter 3. The material stack and material properties were as previous described, but the geometry of the carrier and cell now matched the chip-on-carrier assembly of the Gen II optics, which was a departure from that described in Chapter 3. The channel layout and an example top surface simulated temperature profile are shown in Figure 5-30. Parametric sweeps of the concentration and the *h* parameter were conducted and the average cell temperature was calculated for each combination. As shown in Figure 5-31, this produced a family of curves of average cell temperature vs concentration, where the slope of these curves is the thermal resistance in units of $K \cdot m^2/W$. The ambient air temperature in the model was assumed to be 0 °C.

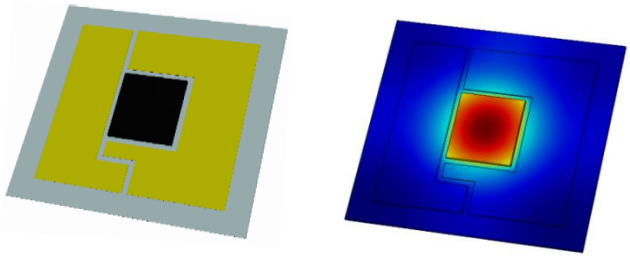

Figure 5-30: Modelled cell-on-carrier in MSI Gen II optics. On the left is the modelled geometry. On the right is a surface temperature plot of the carrier as determined from the numerical model.

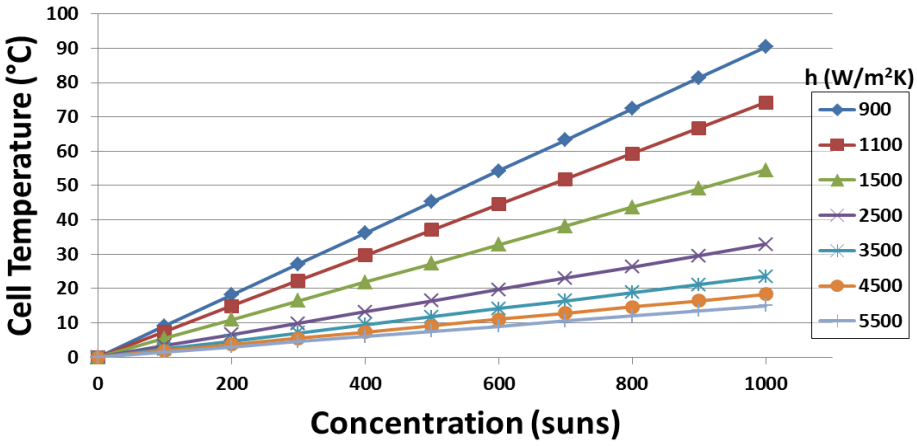

Figure 5-31: FEM modelling results. The slope of the temperature as a function concentration curves is dependent on the convective heat transfer coefficient, *h*.

To extract results like those produced by the numerical simulations from experimental data required the cell temperature to be calculated and the corresponding irradiance incident on the cell to be measured. The cell temperature was calculated using the shift in V_{oc} using a temperature coefficient of 4.5 mV/C°. Since many aspects of optic performance were not well known, including their concentration ratio, I_{sc} was used to estimate the irradiance incident on each cell. Spectrolab's first generation of triple-junction cells (C1MJ – concentrator first generation multijunction) were used in the Gen II optics. Their datasheet quotes a short-circuit current density of approximately 6.9 A/cm^2 at 500 suns [55]. Taking cell area into account this translates into an increase in I_{sc} of 5.47 mA for every one sun increase in concentration. Scatter plots of the cell temperature rise above ambient vs concentration were developed from the I_{sc} dependence on irradiance measurements for each month in 2012. An example is shown below in Figure 5-32. A clear linear trend is observed, as expected, but with a noticeable scatter. The scatter is due to daily fluctuations in the *h* parameter caused by changes in the efficacy of the heat sinking due to changes in wind speed and direction. Scatter could also arise from the nature of the *I-V* measurement itself, since a scan typically took about six seconds to complete with V_{oc} among the first points measured and I_{sc} the last point measured. Irradiance transients caused by passing clouds might have resulted in V_{oc} and I_{sc} measurements under different irradiance conditions. Data points in the analysis with concentration below 5 suns (27.35 mA) were filtered out since the V_{oc}'s below this threshold were ill defined resulting in inaccurate temperature estimations.

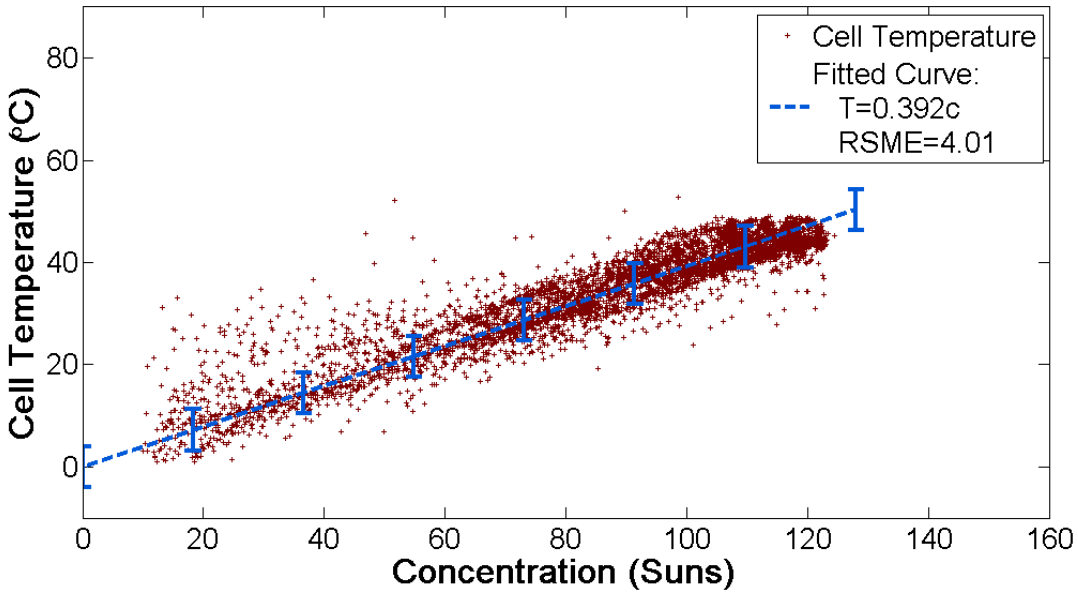

Figure 5-32: Cell temperature rise above ambient vs concentration. The cell temperature is determined from differences in V_{oc} and the concentration is estimated from the measured I_{sc}.

It is known from the modelling results shown in Figure 5-31 and equation (2.20) that the cell temperature is linearly dependent on the irradiance incident so linear regression analyses were performed to determine the slope of the measured cell temperature vs concentration from the scatter plots. Recall that the cell temperatures were calculated as the rise above ambient (the temperature difference between the average cell temperature and the heat sink temperature) so the regression line was constrained to a vertical intercept at 0 °C. Furthermore, examination of the residual plots showed that the scatter was unbiased and homoscedatic (i.e., the variance in the residuals do not depend on the concentration), barring a few anomalous outliers, likely due to passing clouds. Furthermore, the residuals were always observed to be approximately normally distributed for each of the analyzed months. Thus, the residuals were well behaved making the root mean square error (RMSE, or the residual sum of squares) a meaningful metric to quantify the degree of inaccuracy in the analysis. The RMSE is indicated by the error bars in Figure 5-32.

Once the slope of the linear fit from the regression analysis was determined, the slope then had to be compared with the modelling results to determine its equivalent *h* value. The thermal resistance (*R*) (e.g., the slope of the line in Figure 5-31 of the cell-on-carrier) was calculated for each simulated *h* value by finding the slope of the regression line. This was done in MATLAB with the *polyfit()* function. A plot of *h* vs thermal resistance was then created to build a model to convert the determined slopes, or thermal resistances such as that determined in Figure 5-32 into its equivalent *h* value. This allowed an estimation of *h* that would not have been possible by simply comparing the modelling results, where *h* was incremented by 20 W/m^2K. From equation (2.35) we know that the total thermal resistance is approximately inversely proportional to *h* where the spreading resistance term dependence is both complex and relatively

weak. Consequently, a power law was used to model the relationship between *h* and the thermal resistance. The *fit()* routine was used in MATLAB to estimate the relationship as illustrated in Figure 5-33. The equation modelling the dependence of the thermal resistance on *h* was found to be,

$$h = 78.55R^{-1.014} \tag{5.11}$$

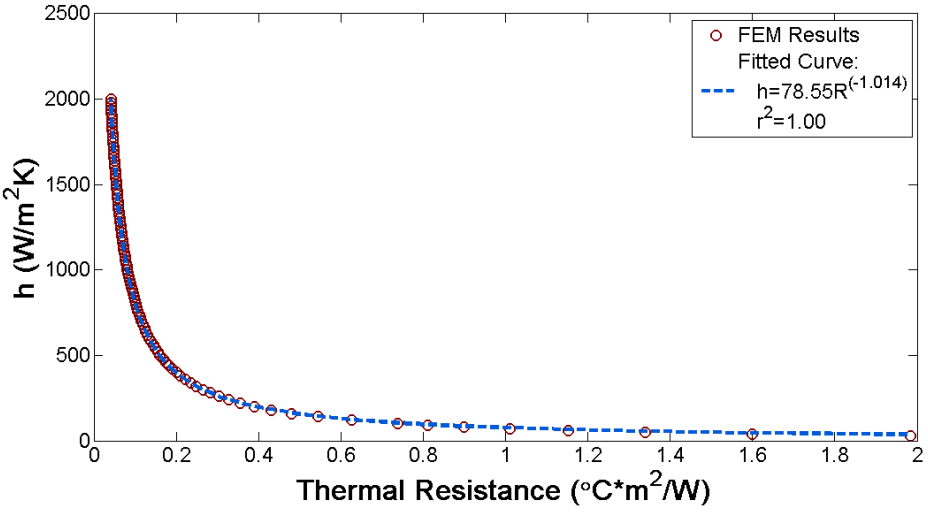

Figure 5-33: Modelled relationship between overall thermal resistance of cell-on-carrier and *h* as determined from the numerical modelling results.

The results of the analyses on optic 7 and optic 8 (the only optics that did not suffer from hysteresis) are shown in Figure 5-34 and Figure 5-35, respectively. No seasonal trends in the heat transfer coefficient are apparent. Assuming ergodicity, comparison of the two optics may be made by averaging the *h* values over the year, which also requires a determination of the uncertainties. Determining the error associated with each monthly calculation of *h* required estimating the error in the temperature measurements, the concentration measurements, and the modelling results. Sources of error contributing to the concentration measurement were through the I_{sc} measurement. Neither the temperature coefficient (A/°C) nor the concentration coefficient (A/suns) of I_{sc} are very sensitive within the range of temperature and concentration values considered in this analysis [57,58]. Only a small amount of error, approximately 1% would have been contributed by these factors. Likewise, the Keithley 2440 SourceMeter has measurement accuracies of better than 0.5 %, an even smaller contribution. Spectral variations that affect the current matching of the subcells [58], and transients caused by clouds, likely also contributed to sources of error. Factors contributing to errors associated with the temperature measurements included the small amount of uncertainty in the V_{oc} made by the Keithley 2440 sourcemeter (<0.5%). The piecewise linear interpolation between points on the *I-V* measurement required to obtain sufficiently precise V_{oc} values also contributed a small amount of error. Furthermore, the temperature coefficient of the C1MJ cell varied with concentration [25], particularly below 200

suns, making it another source of error in the analysis. These quantities may be neglected in comparison to the uncertainties in the primary measurement parameters, the concentration and the temperature shift.

In extracting the thermal resistance (Figure 5-32), the uncertainties in the data were all attributed to the dependent variable (the temperature shift). This assumption was valid so long as the uncertainty associated with the dependent variable was considerably greater than that associated with the independent variable (the concentration) [59], which was arguably true. Therefore, the equation to determine the thermal resistance and its associated uncertainty was

$$R = \frac{T}{Q} \quad \xrightarrow{associated\ error} \quad \frac{\Delta R}{R} = \sqrt{\left(\frac{\Delta T}{T}\right)^2 + \left(\frac{\Delta Q}{Q}\right)^2} = \sqrt{\left(\frac{\Delta T}{T}\right)^2}, \tag{5.12}$$

where the relative uncertainty in temperature was determined by dividing the residual sum of squares (RSS) by the total sum of squares (TSS). Equivalently, the relative uncertainty in the thermal resistance can be expressed in terms of the coefficient of determination (r^2) as

$$\frac{\Delta R}{R} = \sqrt{\left(\frac{RSS}{TSS}\right)^2} = (1 - r^2). \tag{5.13}$$

This was convenient since the r^2 value was readily determined within most statistical analysis algorithms. The error associated with the thermal resistance was then propagated through the power law equation (5.11) to determine the relative uncertainty in the heat transfer coefficient as

$$h = 78.55R^{-1.013} \quad \xrightarrow{associated\ error} \quad \frac{\Delta h}{h} = a\frac{\Delta R}{R} = (-1.013)\frac{\Delta R}{R}. \tag{5.14}$$

The results of the analysis provided an estimated *h* value for optics 7 and 8 with an associated uncertainty. The *h* values were determined by computing the mean of *h* and the associated uncertainty was determined by calculating the mean of the uncertainty. The mean *h* value of optic 7 was found to be 183 ± 52 W/m^{2}K. For optic 8, the mean value of *h* was found to be 224 ± 26 W/m^{2}K. These values agree well with one another within their given uncertainties, so these two optics may be treated as similar.

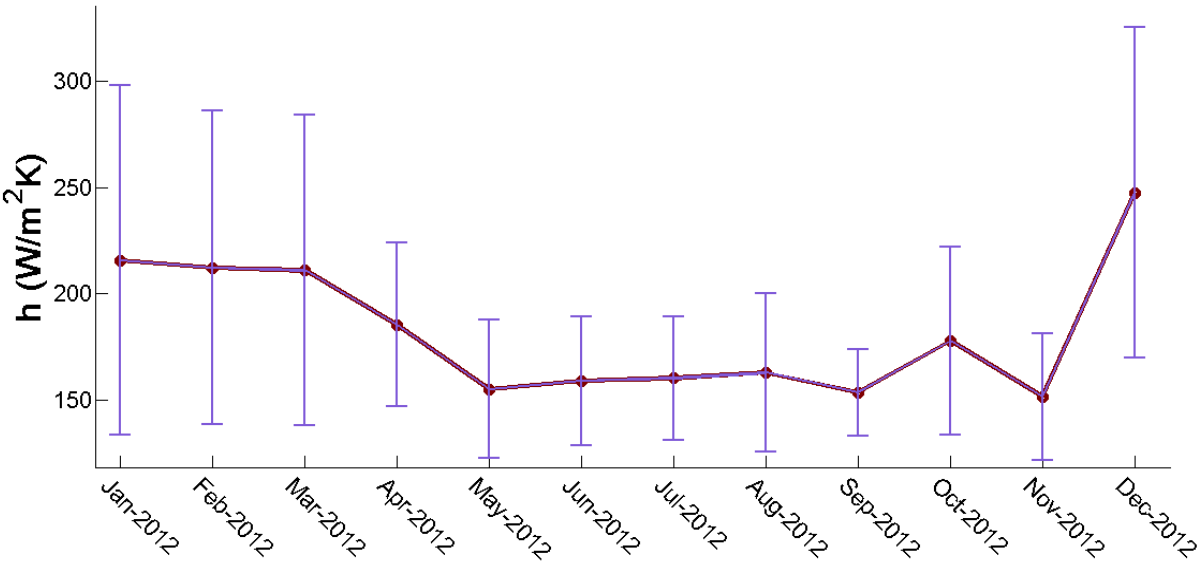

Figure 5-34: *h* of optic 7 calculated for each month of 2012

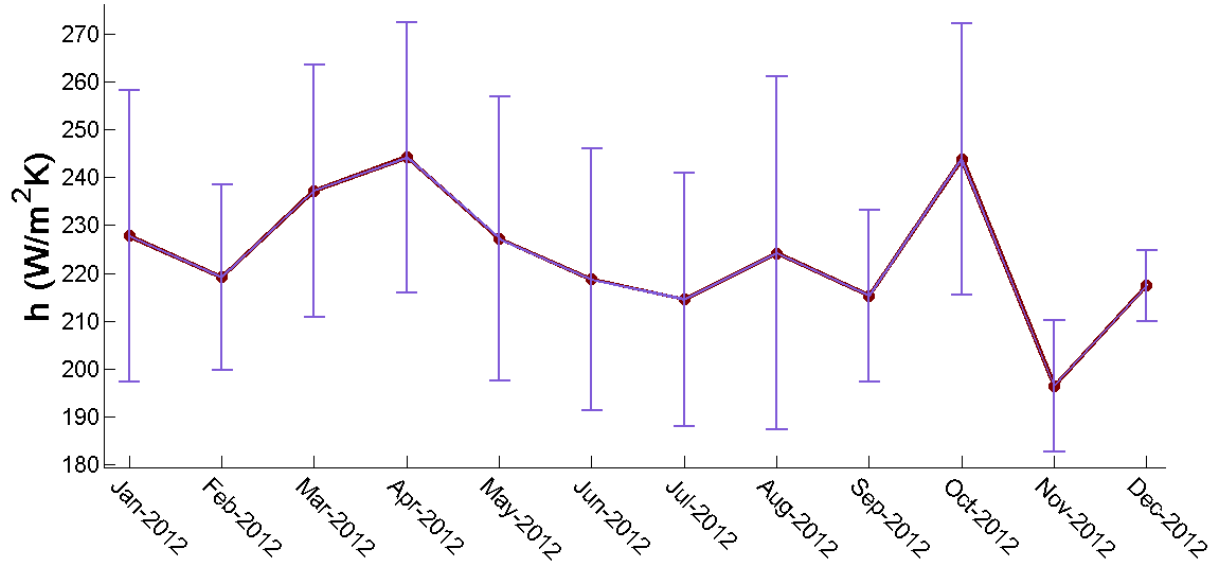

Figure 5-35: *h* of optic 8 calculated for each month of 2012

6 Conclusion

Central to this work was the design and construction of an outdoor PV test and measurement system at uOttawa and at Little Rock, CA. This work has laid the foundation and infrastructure for a comprehensive investigation of different CPV technologies. At this writing, the third generation of MSI's *Sun Simba* modules have been installed and data are now being collected. Third generation panels of the *Sun Simba* modules were also installed in Little Rock. The performance differences between the Sun Simba modules in Ottawa and Little Rock can now be characterized. This includes reliability aspects and electrical performance differences between two very different climates. The meteorological data between the Ottawa and Little Rock climates can also be used to perform energy yield analyses to better quantify the performance differences and to predict, from both a technical and economical standpoint, the penetration of CPV energy solutions into low insolation regions such as Canada.

The impending shortage in fossil fuels and the need to develop alternative sustainable energy sources were briefly discussed in chapter 1. In this context, the intrinsic advantages of PV were outlined, as were the advancements that must be made before CPV becomes a significant PV technology. This thesis has reported notably progress toward the sustainable energy goal by a detailed and comprehensive engineering analysis of MSI's prototype *Sun Simba* light-guiding technology in the context of a multiple site-specific solar resource implementation and analysis. In chapter 2, a thorough discussion of the theoretical fundamentals of PV and the characteristics and properties of the solar resource was given, which included the spectral composition of the sun's light and the apparent motion of the sun observed from the surface of the earth. Different CPV tracking and optical systems were presented, and notable installations were shown to illustrate some of their key advantages and disadvantages. The fundamental physics of a PV cell were presented and the key performance quantities were defined, emphasizing cell response to changes in temperature and irradiance. This permitted the key enabler of efficient CPV systems to be described – the MJSC. The challenges and performance losses associated with connecting cells to form modules and panels were discussed.

The basics of heat transfer were introduced to understand how the optical energy not extracted as electricity would affect system response, as found from steady state thermal modelling of cell-on-carrier assemblies whose thermal properties were comprehensively explored in chapter 3 using a numerical model constructed in COMSOL Multiphysics. The numerical model was then calibrated with experimental data by implementing a large parameter study using COMSOL script within MATLAB, and optimum design parameters were sought. Carrier properties such as carrier geometry and material choices were altered to examine their relationship with the average cell temperature. It was found that the copper layers of the carrier have an optimal thickness of approximately 2.5 mm, which can lead to an increase in efficiency of 0.8 % relative to production carriers. Several different materials for the insulating substrate of the carrier were contrasted and compared. Potential gains in cell efficiency were also outlined by considering different channel configurations. The electrical performance gains and mechanical

trade-offs that arose with different configurations were illustrated. The convective heat transfer coefficient was also varied and the results were discussed. Voids in the solder layer between the cell and carrier were introduced into the model. It was shown that the physics of heat transfer alone was insufficient to describe cell failure caused by solder voids.

The design, construction, technical specifications, and challenges related to the uOttawa and Little Rock test sites were discussed in chapter four. For the uOttawa site, unexpected behavior and performance inconsistencies of the Golden Sun trackers were discussed and the corrective actions taken were explained. The process of aligning the PV panels was outlined, and the instrumentation installed to gather DNI, spectra, and site pictures were revealed. The design and construction of a DC load to sink the power produced by the panels was discussed, and measurements on the individual optics were described. The CPV test and measurement system built in Little Rock was summarized, with a focus only on its differences with the uOttawa test system. Finally, the Microsoft SQL database, created to store the measured data from the test sites and to facilitate remote access of the data, was presented.

In chapter five, the long term performance of the individual optics was investigated. Performance metrics such as I_{sc}, V_{oc}, and fill factor were calculated over the span of 18 months. These metrics were extracted from *I-V* curves corrected to concentrator standard operating conditions using the IEC 60891 curve correction standard. This ensured that all performance comparisons were under equitable operating conditions. A third of the individual optic assemblies studied were shown to be completely degraded, outputing negligible amounts of power. The remaining assemblies showed consistent performance over the analysis period, except for one notable exception. This exception showed a rapid degradation in its shunt resistance, electromigration caused by water ingress into the optic being the plausible cause.

Investigating the performance of the individual optics revealed an unexpected hysteresis characteristic in the I_{sc} vs DNI curves for several of the individual optics. The effect of temperature variations, spectral shifting, and optical misalignment were considered as possible causes. Tracker data and image processing of on-sun images were used to determine the cause of the hysteresis, which was found to be the nonlinear behaviour of the tracker exacerbating optical misalignments.

Connecting the thermal modelling of the cell-on-carrier with the individual optic measurements allowed determination of the convective heat transfer coefficient. Individual optic 7 and individual optic 8 were investigated as they were well aligned, which helped to limit the degree of uncertainty in the estimation. Nevertheless, there was an appreciable degree of uncertainty associated with this estimation as a result of the spread in I_{sc} and V_{oc} measurements caused by factors such as the varying wind speeds and direction, as well as other measurement errors. The mean values of the convective heat transfer coefficients of optic 7 and optic 8 were found to be 183 ± 52 W/m^{2}K and 224 ± 26 W/m^{2}K, respectively, in good agreement with one another.

With the large data sets compiled from the *I-V* measurements at the uOttawa test site, parameters such as temperature coefficients, series resistance, and shunt resistance can now be extracted from a large set of individual optic *I-V* data over extended time periods. Knowledge of these parameters would enable detailed CPV system models to be constructed to provide more accurate performance estimates and energy yield analyses for greater investment certainty.

7 References

[1] W. Zittel *et al.* “Fossil and Nuclear Fuels – the Supply Outlook”. Internet: http://www.energywatchgroup.org/fileadmin/global/pdf/EWG-update2013_long_18_03_2013.pdf, Mar. 2013 [Jun 5, 2013].

[2] I. Dincer. "Renewable energy and sustainable development: a crucial review." *Renewable and Sustainable Energy Reviews*, 2000, pp. 157-175.

[3] W. Van Sark *et al*. "Analysis of the silicon market: Will thin films profit?" *Energy Policy*, 2007, pp. 3121-3125.

[4] M. Raugei and F. Paolo. "Life cycle impacts and costs of photovoltaic systems: Current state of the art and future outlooks." *Energy*, 2009, pp. 392-399.

[5] M.A. Green *et al*. "Solar cell efficiency tables (version 39)." *Progress in photovoltaics: research and applications*, 2011, pp. 12-20.

[6] P. Perez-Higueras *et al*. "High Concentrator Photovoltaics efficiencies: Present status and forecast." *Renewable and Sustainable Energy Reviews*, 2011, pp. 1810-1815.

[7] C. Seshan. "CPV: Not just for hot deserts!" *Photovoltaic Specialists Conference (PVSC), 2010 35th IEEE*. 2010.

[8] NREL, “Best Research - Cell Efficiencies,”. Internet: http://www.nrel.gov/ncpv/images/efficiency_chart.jpg. [Aug 10,-2013].

[9] C.A. Gueymard, "The sun’s total and spectral irradiance for solar energy applications and solar radiation models." *Solar energy*, 2004, pp. 423-453.

[10] ASTM, “G173-03 Standard Tables for Reference Solar Spectral Irradiances: Direct Normal and Hemispherical on 37° Tilted Surface.”

[11] K. Rajeshwar, R. McConnell, and S. Licht. “Solar hydrogen generation: toward a renewable energy future.” Springer, 2008.

[12] S.R. Wenham, M.A. Green, M.E.Watt, and R. Corkish, *Applied Photovoltaics. 2nd ed*. London, UK: Earthscan, 2009.

[13] G.M. Masters, *Renewable and Efficient Electric Power Systems.* Hoboken, New Jersey: Wiley, 2004.

[14] R.A. Messenger and J. Ventre, *Photovoltaic Systems Engineering. 3rd ed*. Boca Raton, Florida: Taylor and Francis Group, 2010.

[15] J. Nelson, *The Physics of Solar Cells.* London, UK: Imperial College Press, 2010.

[16] A.L. Luque and V.M. Andreev, *Concentrator Photovoltaics.* Berlin, Germany: Springer-Verlag, 2007.

[17] R. A. Rohde, "Radiation Transmitted by the Atmosphere," http://www.globalwarmingart.com/, 2007. [Online]. Available: http://www.globalwarmingart.com/wiki/File:Atmospheric_Absorption_Bands_png. [Jun 25, 2013].

[18] C. Honsberg and S. Bowden, "PVCDROM". Internet: http://pveducation.org/pvcdrom, [Jun 5, 2013].

[19] M. Iqbal, *An Introduction to Solar Radiation.* Berlin, Academic, Toronto, 1983.

[20] Cyrium Technologies, "Cyrium's QDEC High-Efficiency CPV Cells". Internet: http://www.cyriumtechnologies.com/sites/default/files/QDEC_Product_Family_Datasheet_SMS-0002-2.pdf, [May 15, 2013].

[21] SolarSystems, "CPV Dish System Overview". Internet: http://solarsystems.com.au/technology-2/cpv-systems-overview/ [Jun 30, 2013].

[22] M. Yandt, "Characterization and Performance Analysis of High Efficiency Solar Cells and Concentrating Photovoltaic Systems," MASc Thesis, University of Ottawa, 2012.

[23] D. Chemisana, "Building Integrated Concentrated Photovoltaics: A Review," *Renewable and Sustainable Energy Reviews*, pp. 603-611, 2011.

[24] Morgan Solar, "How It Works". Internet: http://morgansolar.com/how-it-works/ [Accessed: 14-May-2013].

[25] G.S. Kinsey *et al.*, "Operating Characteristics of Multijunction Solar Cells", *Solar Energy Mat. & Solar Cells*, pp. 950-951, 2009.

[26] C. Chamberlin, P. Lehman, J. Zoellick, and G. Pauletto, "Effects of Mismatch Losses in Photovoltaic Arrays," *Solar Energy,* Vol. 54, No. 3, pp. 165-171, 1995.

[27] S. Lee, "Thermal Challenges and Opportunities in Concentrated Photovoltaics", *12th Electronics Technology Packaging Conference*, pp. 608-613, 2010.

[28] M.M. Yovanovich, Y.S. Muzychka, and J.R. Culham. "Spreading Resistance of Isoflux Rectangles and Strips on Compound Flux Channels," *Journal of Thermophysics and Heat Transfer*, Vol. 13, No. 4, pp. 495-500, 1999.

[29] G. Maranzana, I. Perry, D. Maillet, and S. Rael, "Design Optimization of a Spreader Heat Sink for Power Electronics", *Internation Journal of Thermal Sciences*, No. 43 pp. 21-29, 2004.

[30] Suncore, “CTJ Receiver Assembly – 10 mm x 10 mm”, Internet: http://www.suncorepv.com/index.php?m=content&c=index&a=lists&catid=99, [Mar 30, 2013].

[31] Spectrolab, “CCA 100 C3MJ 1A Concentrator Cell Assembly” Internet: http://www.spectrolab.com/DataSheets/PV/CPV/C3MJ_CCA-100_data_sheet.pdf, Jan. 26, 2011 [Mar 30, 2013]

[32] N. Chasserio, et al. "Ceramic substrates for high-temperature electronic integration." *Journal of Electronic Materials*, pp. 164-174, 2009.

[33] B. Guenin, “Thermal Interactions Between High-Power Packages and Heat Sinks, Part 1”, *Electronics Cooling*, Vol. 16, No.4, March 2010.

[34] R. Simons, “Estimating Parallel Plate-Fin Heat Sink Thermal Resistance”, *Electronics Cooling*, Vol. 9, No. 1, February 2003.

[35] N. Bosco et al. “CPV cell infant mortality study,” in *AIP Conference Proceedings*. Vol. 1407, 2011.

[36] N. Zhu. “Thermal impact of solder voids in the electronic packaging of power devices”, in *Fifteenth Annual IEEE Semiconductor Thermal Measurement and Management Symposium*, 1999, pp.22-29.

[37] M. Cui, *et al*. "Thermal test and analysis of concentrator solar cells," in *Photonics Asia 2007*. International Society for Optics and Photonics, 2007.

[38] P. Cooksley, private communication, AERL technical support, Feb 2012.

[39] SuperLogics, “8017R-A5- Specifications,” Internet: http://www.superlogics.com/serial-data-acquisition/analog-input-modules-rs-485/8017R-A5/111-3171.htm [Apr 10, 2013].

[40] AERL, *AERL Coolmax Maximizer User’s Manual*, ver. 3, May 2010.

[41] R. King, *et al.* “Solar cell generations over 40% efficiency”, *Prog. Photovolt: Res. Appl.*, pp. 801–815, Apr 2012.

[42] AERL, “MPPT Solar Charge Controller,” Internet: http://www.aerl.com.au/solar-battery-charging-mppt/solar-battery-charging-mppt.html [Apr 15, 2013].

[43] Hammond Manufacturing, “General Selection Considerations,” Internet: http://www.hammfg.com/electrical/products/climate/blowers-selection [Apr 15, 2013].

[44] MSDN, “File-Server vs. Client/Server Internet: http://msdn.microsoft.com/en-us/library/office/aa165278(v=office.10).aspx [Apr 15, 2013].

[45] IEC 60891, "Photovoltaic Devices – Procedures for Temperature and Irradiance Corrections to Measured IV Characteristics."

[46] D.L. King, J.A. Kratochvil, and W.E. Boyson. *Photovoltaic array performance model*. United States. Department of Energy, 2004.

[47] Muller, Matthew, et al. "Determining Outdoor CPV Cell Temperature." *AIP Conference Proceedings*. Vol. 1407. 2011.

[48] Y. Sakurada, O. Yasuyuki Ota, and K. Nishioka. "Simulation of Temperature Characteristics of InGaP/InGaAs/Ge Triple-Junction Solar Cell under Concentrated Light." *Japanese Journal of Applied Physics*, 2011.

[49] Y. Tsuno, Y. Hishikawa, and K. Kurokawa. "Translation Equations for Temperature and Irradiance of the IV curves of Various PV Cells and Modules," in *Photovoltaic Energy Conversion, Conference Record of the 2006 IEEE 4th World Conference,* 2006.

[50] Y. Tsuno, Y. Hishikawa, and K. Kurokawa. "Temperature and irradiance dependence of the IV curves of various kinds of solar cells," in *Technical Digest of the PVSEC* 15, 2005, pp. 422-423.

[51] J.S. Krumbein. "Electrolytic models for metallic electromigration failure mechanisms." *IEEE Transactions on Reliability.* pp. 539-549, 1995.

[52] J.S. Krumbein. "Metallic electromigration phenomena." *IEEE Transactions on Components, Hybrids, and Manufacturing Technology*, pp. 5-15, 1988.

[53] P.Y. Varshni. "Temperature dependence of the energy gap in semiconductors."*Physica,* 149-154, 1967.

[54] P. Benítez, *et al*. "High performance Fresnel-based photovoltaic concentrator." *Opt. Express*, pp. 7650-7663, 2010.

[55] Spectrolab, "Application Note 0902: Analytical Model for C1MJ and C3MJ CDO-100 Solar Cells and CCAs" Internet: http://www.spectrolab.com/appnotes/0902AnalyticalModelforC1MJandC3MJCDO-100CellsandCCAs.pdf, Nov. 16, 2009 [Mar 30, 2013]

[56] IEC 62670, "Concentrator photovoltaic (CPV) module and assembly performance testing and energy rating – Performance measurement and power rating," Draft Standard.

[57] A. Braun, *et al*. "Temperature dynamics of multijunction concentrator solar cells up to ultra-high irradiance." *Progress in Photovoltaics: Research and Applications,* 2011.

[58] G. Siefer and A.W. Bett. "Analysis of temperature coefficients for III–V multi-junction concentrator cells." *Progress in Photovoltaics: Research and Applications*, 2012.

[59] P.R. Bevington and D.K. Robinson. *Data reduction and error analysis for the physical sciences*. New York: McGraw-Hill, 1969.

[60] IOFFE, "Semiconductors on NSM" Internet: http://www.ioffe.rssi.ru/SVA/NSM/Semicond/, [Apr 27, 2013].

[61] C.J.M. Lasance. "The thermal conductivity of pure metals." *Electronics Cooling*, pp. 16-21, 1999.

[62] C.J.M. Lasance. "The thermal conductivity of aluminum oxide." *Electronics Cooling*, 1999.